KU Leuven
Biomedical Sciences Group
Faculty of Medicine
Doctoral School of Biomedical Sciences





MITOCHONDRIAL METABOLISM SETS THE SPECIES-SPECIFIC TEMPO OF NEURONAL DEVELOPMENT

Pierre CASIMIR

Jury:

Supervisor KU Leuven: *Dr. Pierre Vanderhaeghen*
Supervisor ULB: *Dr. David Gall*
Co-supervisor: *Dr Ryohei Iwata ULB-KU Leuven*
Chair examining committee: *Dr Patrick Callaerts*
Chair public defence: *Dr Patrick Dupont*
Jury members: *Dr Esteban Gurzov*, *Dr Bassem Hassan, Dr Sebastian Jessberger, Dr Godelieve Moons, Dr Serge Schiffmann, Dr Patrik Verstreken,*

Dissertation presented in partial fulfilment of the requirements for the joint degree of Doctor of Biomedical sciences (KU Leuven) and *Doctor of Medical sciences (ULB)*

2023-2024

Table of contents

List of Abbreviations **4**

Introduction **6**

The Human Brain Size and Complexity *6*

Prolonged Maturation of Human Cortical Neurons *7*

Divergence and Convergence of Gene Regulatory Networks (GRN) between Species *8*

The role of Metabolism and Mitochondria during Development *10*

Objective of the Research **16**

Results **17**

Mitochondria Growth and Dynamics during Cortical Neuron Maturation follow a Species-Specific Timeline *17*

Mitochondrial Metabolic Activity is Lower in Human than Mouse Developing Cortical Neurons *23*

Increasing Mitochondria Activity in Human Neurons leads to Accelerated Neuronal Maturation, Growth and Complexification *29*

Effects of Increasing Mitochondria Activity in Human Cortical Neurons on Protein Turnover *40*

Discussion **44**

Materials and Methods **52**

Mice *52*

DNA Constructs *52*

Lentiviral preparation *54*

Cell culture media *54*

Human PSC culture and cortical cell differentiation *56*

Mouse PSC culture and cortical cell differentiation *57*

Immunostaining *57*

NNN-labeling *58*

Mouse mitochondria labeling *59*

PSC-derived Mouse mitochondria labeling *59*

Human mitochondria labeling *60*

Mitochondrial morphology analysis *60*

CLEM (correlative light and electron microscopy) *61*

Xenotransplantation *63*

Oxygraphy *64*

Metabolic labeling *66*

Measurement of whole-cellular NAD/NADH *68*

Proteomics for measurement of protein turnover *69*

Electrophysiological recordings *72*

Detection of KCl-induced NPAS4 expression *73*
Impact of metabolic modulators on KCl-induced NPAS4 expression *74*
Neuronal morphology analysis of NNN-labeled cell *76*
Statistical analysis *78*
Abstract **79**
Uittreksel **79**
References **81**
Acknowledgements **92**
Personal Contribution **93**
Conflict of Interest **94**
Curriculum Vitae **95**

List of Abbreviations

Acetyl-CoA: Acetyl-coenzyme A

ACN: Acetonitrile

ADP: Adenosine diphosphate

AlbuMAX: medium additive enriched in FFA

ATP: Adenosine triphosphate

CLEM: correlative light and electron microscopy

COXII: Cytochrome c oxidase subunit 2

COX8A: Cytochrome c oxidase subunit 8A

CreER^{T2}: Cre recombinase fused to a mutant Estrogen receptor ligand-binding domain

DAPT: *N*-[*N*-(3,5-Difluorophenacetyl)-L-alanyl]-*S*-phenylglycine *t*-butyl ester

EdU: 5-ethynyl-2'-deoxyuridine

eGFP: enhanced green fluorescent protein

ETC: electron transport chain

FFA: free fatty acids

GRN: Gene Regulatory Network

GSH: reduced Glutathione

GSK: GSK-2837808A, chemical inhibitor of LDHA

GSSG: oxidized Glutathione

hPSC: Human Pluripotent Stem Cells

IUE: in utero electroporation

KCl: Potassium Chloride

LDH: lactate dehydrogenase

LDHA: lactate dehydrogenase subunit A

LDHB: lactate dehydrogenase subunit B

MACS: magnetic-activated cell sorting

Mito-EmGFP: Emerald-green fluorescent protein fused to mitochondrial targeting sequence of COX8A

MNs: secondary motor neuron

mRNA: messenger Ribonucleic acid

mtDNA: mitochondrial Deoxyribonucleic acid

NAD: Nicotinamide Adenine Dinucleotide

NADH: Nicotinamide Adenine Dinucleotide - reduced

NeuroD1: Neuronal Differentiation 1

NGN2: neurogenin 2

NNN: NeuroD1-dependent Newborn Neuron

NPAS4: Neuronal PAS Domain Protein 4

NPC : Neural progenitor cell

NRF1 : nuclear respiratory factor 1

NRF2 : nuclear respiratory factor 2

OCR: oxygen consumption rate

OXPHOS: oxidative phosphorylation

O_2: Dioxygen

PDH: Pyruvate Dehydrogenase

PGC-1α: peroxisome proliferator-activated receptor γ co-activator-1α

PSC: Pluripotent Stem Cells

PS10: PDH kinase (PDK1-4) inhibitor

PTM: post-translational protein modification

RNA: Ribonucleic acid

RNA-seq: RNA sequencing

scRNA-seq: single cell RNA sequencing

SRGAP2: SLIT-ROBO Rho GTPase-activating Protein 2

TCA: tricarboxylic acid

tCD8: truncated CD8

TEM: transmission electron microscopy

TFAM: mitochondrial transcription factor A

TMRM: tetramethylrhodamine methyl ester

UK-5099: (E)-2-cyano-3-(1-phenylindol-3-yl)prop-2-enoic acid: mitochondrial pyruvate carrier inhibitor

UPS: ubiquitin proteasome system

^{13}C: Carbon 13

4-OHT: 4-Hydroxy-Tamoxifen

Introduction

The Human Brain Size and Complexity

The remarkable size and complexity of the human brain, as well as its prolonged development resulting in extended critical periods of learning and plasticity, have been proposed to play a role in the acquisition of human-specific cognitive features(*1*, *2*).

Across a wide range of species, brain size is correlated with body size and neocortex volume is itself expanding exponentially with brain size. The human brain slightly deviates from this correlation with a larger brain than predicted by the allometric rules(*3*–*5*). Furthermore, brain size cannot be used to directly infer the number of neurons in the brain, as brain size and neuron numbers are differentially correlated in different taxa, brain size increasing hypermetrically in rodents(*6*) and isometrically in primates(*7*) with the number of neurons, resulting in a much larger number of neurons in a primate brain compared to a rodent brain of similar size(*4*, *7*). As a result, in addition to a slight increase in relative size, the human brain is also characterized by a larger absolute number of neurons compared to all non-human primates and most other mammals(*4*, *5*).

Besides brain size and neuron number, common principles of brain network organization (connectomics) are shared across species with the formation of small circuits with high clustering combined with fewer long distance connections between them(*8*). If global myelination maps display similarities between primates and even with the mouse, the human brain contains proportionally larger regions of lightly myelinated cortex, mostly in pre-frontal, lateral temporal, parietal and insular areas, compared to chimpanzee and macaque, which are intermediate, and marmosets in which heavily myelinated regions occupy the highest proportion of the cortex(*5*, *9*, *10*).

Furthermore, looking closer at the cellular level, the human brain is also characterized by a higher level of complexity as exemplified by dendritic morphology of pyramidal neurons in the neocortex. Indeed, despite regional variation in pyramidal neuron structure, being more

complex in pre-frontal area compared to primary visual, sensory or motor cortices, human pyramidal neurons display a larger dendritic field area, higher spine density and more branched dendritic arborization in all cortical regions compared with chimpanzee and macaque(*11*–*14*).

Prolonged Maturation of Human Cortical Neurons

The human brain is characterized by a prolonged development. In particular, human cortical neurons are characterized by a prolonged timing of maturation compared to other species(*15*). Morphologically, during maturation the cortical neuron undergoes soma enlargement, growth and ramification of the apical dendrite and of the axon, followed by basal dendrites, development of dendritic spines and synaptic connections with first an overproduction of spines followed by synaptic pruning and selective stabilization of synapses(*16*–*19*). Cortical neurons complete their morphological maturation in 3-4 months in the mouse and in the rat(*16*, *20*), in 3-4 years in the macaque(*17*), while in human, it takes 2-3 years for the soma and dendritic arborization to reach and adult-like morphology(*21*, *22*) and 35-40 years for the spine density to stabilize at the adult level in the prefrontal cortex(*19*, *23*). This morphological maturation is paralleled by a metabolic maturation as measured by glucose utilization rate that increases concomitantly to synaptic overproduction and decreases concurrently to synaptic pruning(*24*–*27*). This timing difference between species is conserved in *in vitro* cultures of cortical neurons(*28*–*31*). A role of cell-extrinsic regulatory mechanisms has been shown with studies comparing cortical neuron maturation in pure neuronal cultures or in co-culture with astrocytes or mixed glial cultures (mixed populations of astrocytes, oligodendrocytes and microglia) that have established that the presence of glia accelerates cortical neuron maturation, both electrophysiologically and morphologically, identifying cues involved in cross-talks between glia and neurons regulating dendritic growth and synaptic development and stabilization(*32*–*37*). However, besides extrinsic regulatory

cues, human and primate cortical neurons derived from pluripotent stem cells (PSC) and xenotransplanted into the mouse cortex develop along their species-specific timelines, which is pointing to mainly cell-intrinsic regulatory mechanisms(*18*, *38*, *39*) A protracted maturation timeline is also observed in human compared to chimpanzee and Bonobo neurons when neural induction is accelerated by forced expression of proneural factor NGN2, using the same protocol and culture conditions for the different species, further pointing to cell-intrinsic regulatory mechanisms(*40*, *41*).

Divergence and Convergence of Gene Regulatory Networks (GRN) between Species

One main driver of evolution relates to changes in the regulation of gene expression(*42*). During development, there is a successive expression of different transcriptional programs at different positions in the embryonic space that is the result of localized and transient expression of genes coding for sequence-specific transcription factors interacting with their target DNA sequence elements producing specific patterns of target gene expression, these target genes being other regulatory genes or genes expressing spatially important signaling components. The logic map summarizing the functional links between regulatory genes and their target regulatory modules resulting in the developmental pattern of gene expression is called a Gene Regulatory Network (GRN)(*42*, *43*). The protracted/neotenic maturation of human cortical neurons could be related to differences in GRNs compared to other species, with changes resulting in new human-specific subcircuits composed of original rearrangements of common genes (shared with other species) or by the apparition/alteration of few new genes in the hominid branch of the evolution (Fig.1A). Indeed, genomic studies have identified large segmental gene duplications that occurred in the human lineage generating paralog gene copies that became a substrate for subsequent evolution(*44*, *45*). Several of these human-specific gene families are expressed in the human cortex during its

development(*46*) and have been hypothesized to play a role in the acquisition of human-specific features. One of the strongest candidate gene family identified so far is the SLIT-ROBO Rho GTPase-activating Protein 2 (SRGAP2) gene family. SRGAP2 is a post-synaptic protein, localized in both excitatory and inhibitory synapses, acting as a positive regulator of synaptogenesis. Its paralog (human-specific) gene SRGAP2C acts as a negative regulator of the ancestral gene and gain-of-function experiments in the mouse developing cortex resulted in delayed dendritic spine maturation and synaptogenesis, with, at mature stages, an increase in dendritic spine density(*15*, *47*, *48*). These data make of SRGAP2C a strong candidate human-specific gene that could control some aspects of the human-specific neoteny of dendritic spine and synapse maturation, although it has not been tested yet in human neurons(*49*). The functions of many other of these gene families still remain unknown and need to be investigated but their implications have been so far found to be involved mainly in either early neurogenesis or late synaptogenesis and too restricted to account for global neoteny of human cortical neuron maturation(*46*, *47*, *50*).

Other genetic mechanisms that have been related to human evolution comprise differential expression of GRN modules/subcircuits induced by species-specific changes in one or a few of its components(*51–53*), in non-coding RNAs(*54*), in the activity of enhancer elements(*55*, *56*) or in the patterns of alternative splicing(*57*). Such mechanisms could be at the origin of significant species-specific changes due to modulation of the expression of GRN subcircuits without change in the global architecture of the GRN.

Many comparative genomic, epigenomic and transcriptomic analyses have investigated expression patterns in the human developing cortex compared to non-human species(*58–65*), mostly chimpanzee and macaque, using either primary pre- and post-natal cortical samples or PSC-derived organoid samples, and have shown that gene co-expression patterns and transcriptional programs determining cell types are largely conserved among primates. These analyses have also revealed divergent chromatin accessibility and gene

expression patterns, identifying genes displaying species-specific (and human-specific) spatial or temporal expression patterns. In particular, they documented a prolonged developmental timeline in human, the transcriptome-wide developmental delay between human and non-human primates following closely time-shift trajectories based on life history landmarks and/or brain growth curves, confirming at the gene level what is known at the cellular level(*63*). They also identified genes for which the transcriptional delay exceeds what would be predicted from developmental rate differences among species and which represent interesting candidate genes as modifiers of key GRNs. However, these analyses failed so far to unravel the species-specific gene regulatory mechanisms underlying the prolonged timescale of neuronal maturation itself. This could result from our limited understanding of the complex developmental GRN of cortical neuron maturation, or because changes in the GRN itself are not the main drivers of species-specific timescale differences.

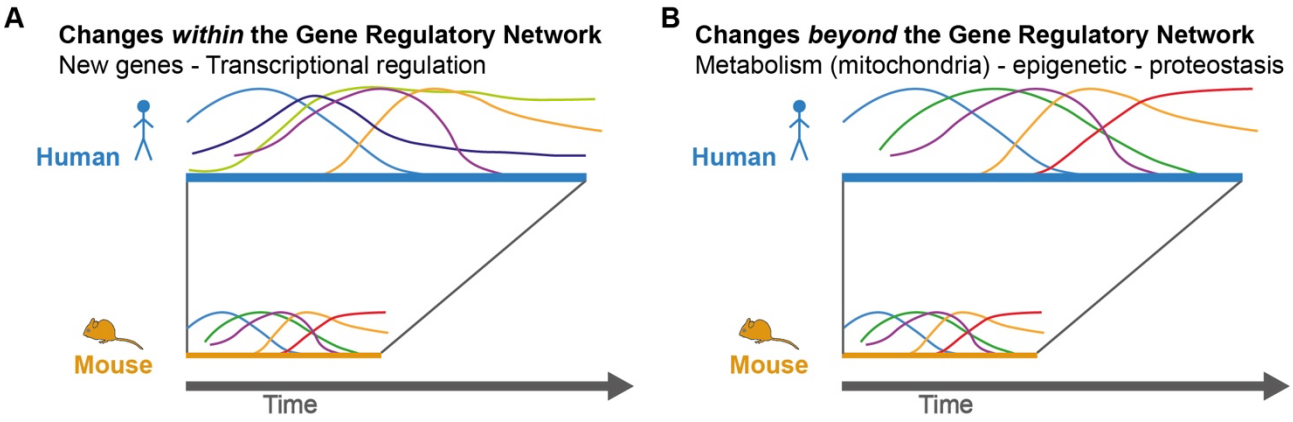


Figure 1. Schematic representation of two non-mutually exclusive mechanisms underlying divergence of developmental timing between species, implying divergence of GRN components, e.g. by the apparition of few new genes in the hominid branch of the evolution (A), or conserved GRN driven at different pace by divergent global metabolic processes (B).

The role of Metabolism and Mitochondria during Development

The neotenic maturation of cortical neurons could be linked to divergence in processes that do not participate directly to the GRN but influence the way it proceeds over time (Fig.1B). These could include global cellular mechanisms such as RNA and protein turnover,

intermediary metabolism and chromatin landscape remodeling. Indeed, the protracted timing of cortical neuron maturation can be considered in the broader perspective of the rate of embryonic development across taxa which is also a highly variable and species-specific life trait. In birds and mammals, the rate of embryonic development is correlated to lifespan(*66*, *67*). Lifespan itself is correlated to the body mass and to the resting metabolic rate of an animal in such a way that larger animal species live longer compared to small-bodied animals, and larger animals also expend more energy because of their bigger mass. But the resting metabolic rate scales up with body mass in such a way that the mass-specific resting metabolic rate, that is the energy expenditure per gram of tissue per unit of time, is higher in small-bodied animals than in larger ones(*68*–*71*). The latter relationship between resting metabolism and body mass has been formalized as the Kleiber's law(*68*–*70*, *72*).

These life trait relationships have been established mainly at the organism level and using heat production or, more often, oxygen consumption rate as a proxy for metabolic rate. A few studies have assessed the metabolic rate at the cellular level, mainly in fibroblasts and hepatocytes but also kidney cortex, and the correlation between the cellular oxygen consumption rate and body size of the animal seems to be conserved at the cellular level(*73*–*75*) even if there is still some controversy(*76*).

A causal role of the metabolic rate in the control of growth rate has been speculated and been the object of theoretical developments(*72*). In particular, whether these correlations between metabolism, growth and body size reflect scaling of intrinsic cellular metabolism or constraints in energy delivery by the vascular system in the adult(*70*, *71*) remains controversial, but importantly, current literature reports only correlations between these life history traits and failed so far to properly test and show a causal relationship. Furthermore, the pertinence and veracity of these correlations was not assessed during embryonic development, even less so during brain development and cortical maturation.

The recurrent use of the oxygen consumption rate as a proxy for metabolic rate implies that

the previously mentioned correlations involve, not necessarily exclusively but predominantly, the mitochondrial oxidative metabolism. This raises the question whether the differences in oxygen consumption rate observed at the cellular level are reflecting differences in the quantity per cell and/or efficiency of mitochondria between animals of different sizes(*75*, *77*).

Mitochondria are double membrane organelles that are thought to have evolved from a symbiotic relationship between aerobic bacteria and primordial eukaryotic cells. They are the site of oxidative phosphorylation in eukaryotic cells and they also participate in intermediary metabolism, calcium signaling and apoptosis. Mitochondria maintain a genome that encodes proteins essential for their respiratory function, but most mitochondrial proteins are encoded in the nuclear genome and imported into mitochondria. Mitochondria are highly dynamic organelles constantly undergoing fusion and fission, and being transported along the cytoskeleton to different cellular sub-compartments and regions, in particular in neurons, in the soma and in the axon and dendritic arborizations(*78–81*).

Some early papers addressed this question whether different oxygen consumption rate at the cellular level would be linked to differences in mitochondrial quantity per cell and/or efficiency between animals of different sizes. They reported that mitochondrial quantity per gram of liver tissue decreases with increasing body mass. Interestingly however, the cellular oxygen consumption diminishes more than the mitochondrial content, suggesting an additional decrease in mitochondrial activity per se with increasing body mass. Indeed, a higher proton leak was also reported in smaller animals, as well as an increased surface of inner mitochondrial membrane(*74*, *77*, *82–85*). Again however, these early papers did not investigate more specifically the role of mitochondria during development, nor tested/showed a causal relationship between mitochondrial content, growth rate and body size.

More recently, several reports identified mitochondrial activity as one of the mechanisms

driving cell maturation in different systems in cell cultures, including cardiomyocytes and pancreatic β cells(*86–89*) derived from hPSC.

Mitochondria function and its modulation through mitochondria biogenesis, mitochondrial dynamics regulation and transport have also been linked to neural development and plasticity. Mitochondria biogenesis requires the coordinated synthesis of proteins encoded by the nuclear and mitochondrial genomes(*90*). Peroxysome proliferator-activated receptor γ co-activator-1α (PGC-1α) is a transcription co-activator that has been identified as a master regulator of mitochondrial biogenesis(*91*). A transcription co-activator is a protein that increases the probability of a gene being transcribed but does not itself bind to DNA(*92*). PGC-1α interacts with numerous transcription factors including nuclear respiratory factor 1 and 2 (NRF1 and NRF2) that control the expression of mitochondrial proteins and of mitochondrial transcription factor A (TFAM) which itself is critical for the initiation of mitochondrial DNA (mtDNA) transcription and replication(*90*, *92*, *93*). Mitochondria biogenesis through modulation of PGC-1α expression has been associated to the formation and maintenance of neuronal dendritic spines in cultured hippocampal neurons(*93*). In another report, decreased mitochondria biogenesis through TFAM deletion *in vivo* in a mouse model of adult neurogenesis resulted in compromised growth and maturation of hippocampal adult-born neurons, as exemplified by a reduced dendritic length and complexity(*94*). Furthermore, disruption of mitochondrial dynamics and/or transport during cortical neuron maturation have been associated with morphological changes/alterations of dendritic arbor, both *in vitro* and *in vivo*(*95–97*). In the maturing dendrites, mitochondria were also associated with morphogenesis and plasticity of spines and synapses(*95*, *98*). In particular, mitochondria representing spatially stable compartments in the vicinity of dendritic spines and synapses have been shown to support activity-dependent dendritic translation and thereby synaptic plasticity(*99*). Altered mitochondrial morphology and metabolism in Fragile X syndrome with increased leakage of the inner mitochondrial membrane have also

been linked to changes in protein synthesis rate and perturbation of dendritic spine maturation and plasticity(*100*).

However, how mitochondrial function evolves during cortical neuron maturation and comparison between species in the context of evolution has not been explored yet.

Interestingly, lifespan and the resting metabolic rate at the cellular level have also been correlated to protein turnover kinetics. Indeed, measurement of protein turnover kinetics on proteome-wide scale in fibroblasts of different species showed that short-lived species displayed a higher turnover rate than larger longer-lived ones(*101*, *102*).

Within the cell, proteins are constantly degraded and re-synthesized. The turnover rates are highly variable within the proteome with protein high-lives ranging from minutes to years(*101*, *103*). Many factors influence the turnover rate including sequence determinants and physico-chemical parameters of the protein, as well as the relative activity and selectivity of proteolytic pathways within the cell. Hence, proteins of identical sequence can have different half-lives within different cell types, tissues, and environmental conditions(*101*, *103*). Secondary motor neurons (MNs) are a prominent neuronal subtype of the spinal cord that mature in 3-4 days in the mouse and in 2 weeks in humans. The GRN of secondary motor neuron maturation is highly conserved across vertebrates(*104*). Using MNs maturation as a model, the difference in the rate of neuron maturation between mouse and human has been shown to be unrelated to changes in genomic sequences nor in the sensitivity to specific signaling pathways(*105*). Instead, difference in kinetic features of gene expression were proposed to be at play. In particular, a global increase in protein lifetime was identified in human cells. This included key transcription factors of MNs maturation GRN. This difference in protein turnover between species correlated to interspecies difference in the dynamics of differentiation(*105*).

Another model used to study developmental timing is the somite segmentation, that is, the sequential formation of paired body segments out of presomitic mesoderm. Its timing is

determined by oscillatory gene expression(*106*) and is different between species. Despite the different cellular context, the analysis of the causes underlying timing differences between species also pointed to differences in biochemical reaction speeds as a candidate mechanism. In particular, protein half-lives(*106*), as well as mRNA half-lives(*106*), mRNA splicing and export kinetics(*106*, *107*) were all longer/slower in human versus mouse. The observed differences were sufficient to quantitatively account for the longer oscillatory period in gene expression in the human segmentation clock(*106*). However, no causal relationship between the protein turnover rate and developmental timing was demonstrated yet.

Objective of the Research

The objective of my PhD thesis project was to test the hypothesis that species-specific features of mitochondria and metabolism regulate the intrinsic developmental timing of cortical neuron maturation. To achieve this purpose, we first started to document changes in mitochondrial quantity, morphology and dynamics across time during cortical neuron maturation, from the early newborn neuron stage to the mature stage, and across species, comparing mouse to human. We acquired data both *in vitro*, using mouse primary cultures of neurons and mouse and human PSC-derived cortical neurons, and *in vivo*, on in-utero electroporated mouse cortical neurons, or ESC-derived human cortical neurons xenotransplanted onto mouse neonatal cortex, using confocal microscopy and electron microscopy techniques. Then, we documented changes in mitochondrial function during cortical neuron maturation in both species by measuring the cellular oxygen consumption rate and by performing targeted metabolomics experiments, using cortical neurons at different maturation stages. These functional data were analyzed in the perspective of the morphological data previously gathered. Based on species-specific differences identified in mitochondrial morphology and metabolism during cortical maturation, we then applied a long term modulation of mitochondrial function during human and mouse cortical neuron maturation, *in vivo* and *in vitro*, using chemical compound treatments or genetic manipulation, and used morphological, electrophysiological and functional readouts of neuron maturation, to test for a causal relationship between mitochondrial function and cortical neuron maturation rate. Finally, we performed proteomics experiments to document differences in protein turnover kinetics, between species, and after modulation of mitochondrial activity, to start to investigate a potential role of protein turnover kinetics in the regulation of cortical neuron maturation rate.

Results

NB: the data presented here, except for data in Fig.8E-H and Fig.16, were published in :

R. Iwata*, P. Casimir*, E. Erkol, L. Boubakar, M. Planque, I. M. Gallego López, M. Ditkowska, V. Gaspariunaite, S. Beckers, D. Remans, K. Vints, A. Vandekeere, S. Poovathingal, M. Bird, N. Corthout, P. Vermeersch, S. Carpentier, K. Davie, M. Mazzone, N. V. Gounko, S. Aerts, B. Ghesquière, S.-M. Fendt, P. Vanderhaeghen, Mitochondria metabolism sets the species-specific tempo of neuronal development. *Science*. **0**, eabn4705 (2023).*Equal contribution

As this is a collaborative work resulting in a publication with a shared first-authorship, the present manuscript was centered on data I had a major contribution in the acquisition of, with the exception of Fig. 10 D-I which was acquired by Dr Iwata in collaboration with the imaging facility and electrophysiology unit of VIB-KULeuven CBD. Data I had no major contribution in the acquisition of is discussed but not presented. The lector is referred to the sus-mentioned publication for more details.

Mitochondria Growth and Dynamics during Cortical Neuron Maturation follow a Species-Specific Timeline

A major challenge to study neuronal maturation is that neurogenesis is not synchronous. After amplification by symmetric divisions, neuronal progenitors undergo several rounds of asymmetric divisions allowing them to self-renew while producing early newborn neurons(*15*, *108*, *109*). This results in populations of neurons born at different time points co-existing at the same stage of brain development. Similarly, during *in vitro* generation of cortical neurons, it results in heterogeneous cultures of neurons of different ages in the same dish. To study cortical neuron development with optimal temporal and cellular resolution, we developed a genetic neuronal birthdating system: the NeuroD1-dependent Newborn Neuron

(NNN) labeling. It combines the expression of Tamoxifen-inducible CreER^{T2} under the control of the promoter of NeuroD1, together with Cre-dependent (floxed) reporters eGFP and/or truncated CD8 (tCD8), enabling identification or MACS purification of the labeled cells (Fig.2A). As the NeuroD1 promoter is turned on transiently at the time of neuron generation(*58*), a pulse of Tamoxifen (4-OHT) allows the selective labeling of a cohort of neurons born at precise time-points, which display a timely progression in dendritic growth and complexity (Fig.2B,C). To maximize the number of neuronal cells born at similar time points, the cultures are treated simultaneously with the Gamma-secretase inhibitor DAPT, which inhibits Notch signaling and thereby increases cortical neurogenesis(*110*), followed by CD8 MACS-sorting so that the purified NNN-labeled neurons thus display homogeneous maturation patterns.

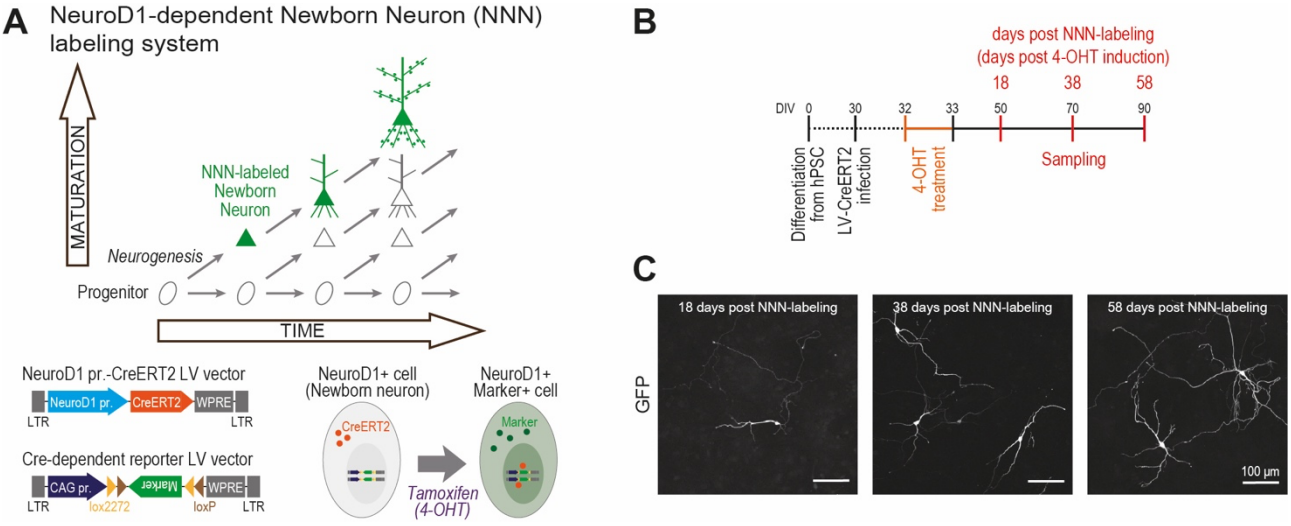


Figure 2. **Cortical neuron maturation at high temporal and cellular resolution.** (A) Schematic of NeuroD1-dependent Newborn Neuron (NNN)-labeling system. (B) Experimental timeline. (C) Representative images after NNN-labeling in human PSC-derived cortical neurons.

By applying the NNN-labeling system to mouse cortical neurons in combination with mitochondria labeling with Mito-EmGFP (Emerald-GFP protein fused to mitochondrial targeting sequence of COX8A), we observed that mitochondria are initially small in size and relatively sparse in newly born mouse neurons, as expected(*111*), and gradually grow in 2-

3 weeks during neuronal maturation (Fig.3A,C). A comparable timeline was observed using mouse PSC-derived cortical neurons(*112*). However, a similar examination of PSC-derived human cortical neurons revealed a more prolonged timeline of mitochondria development, spanning several months (Fig.3B,C).

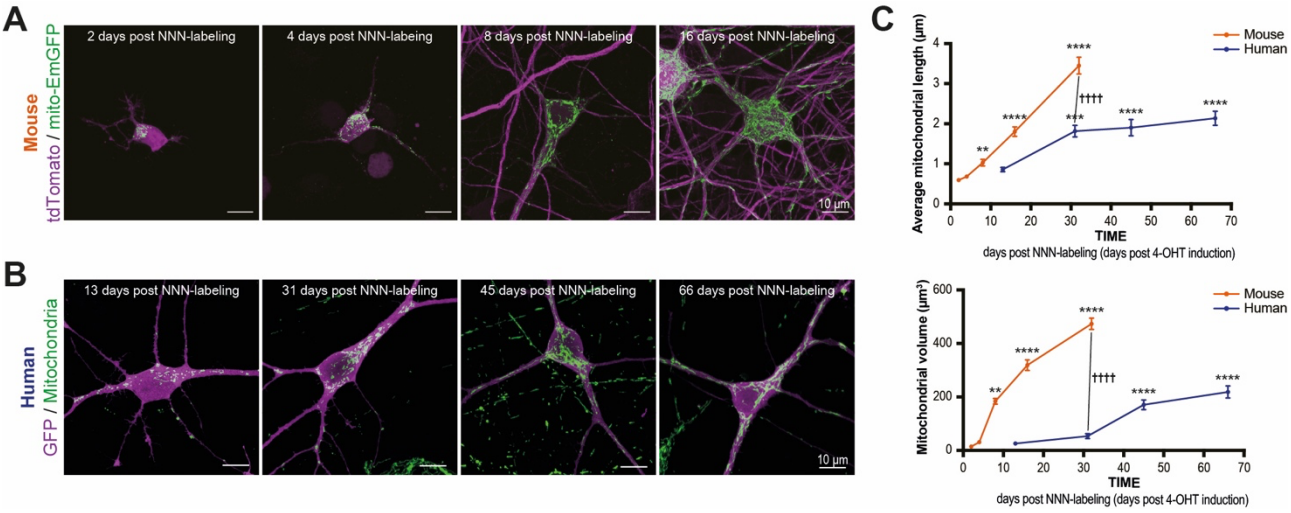


Figure 3. Mitochondria growth and dynamics follow a species-specific timeline during cortical neuronal maturation. (A,B) Representative images of mitochondrial morphology in NNN-labeled neurons in (A) mouse and (B) human. (C) Quantification of average mitochondrial length (top) and mitochondria volume (bottom) per cell from two or three biological replicate experiments. Data are shown as mean ± SEM. Mouse (2, 4, 8, 16, 32 days post (dp) NNN-labeling. Length: N=10, 11, 10, 10, 5 cells. Volume: N=6, 8, 10, 9, 5 cells). PSC-derived Mouse (4, 18 dp NNN-labeling. Length: N=9, 9 cells. Volume: N=9, 9 cells). Human (13, 31, 45, 66 dp NNN-labeling. Length: N=20, 15, 17, 18 cells. Volume: N=9, 11, 22, 20 cells). Compared with the first time point: Dunnett's multiple comparisons test. **P < 0.01, ***P < 0.001, ****P < 0.0001. Compared mouse and human: Unpaired t test. ††††P < 0.0001.

To confirm these *in vitro* observations, we looked at mitochondrial dynamics in mouse and human maturing cortical neurons *in vivo*. In mouse, we first labeled cortical neurons with eGFP using in utero electroporation (IUE) at E14.5, followed by correlative light and electron microscopy (CLEM) at several time points until cortex maturation at postnatal day 30 (P30) (Fig.4A). Next, we performed xenotransplantation of DAPT-treated PSC-derived human cortical neurons transduced with eGFP (Fig.4B). In this system, xenotransplanted neurons integrate into mouse cortex within a few days after transplantation and display a protracted

pattern of maturation, taking months to reach maturation(*18*, *38*). CLEM performed on these neurons revealed that the human cortical neurons displayed much slower patterns of mitochondria growth than their mouse counterparts, taking months to reach similar levels of mitochondria development as the mouse does in four weeks (Fig.4A,B).

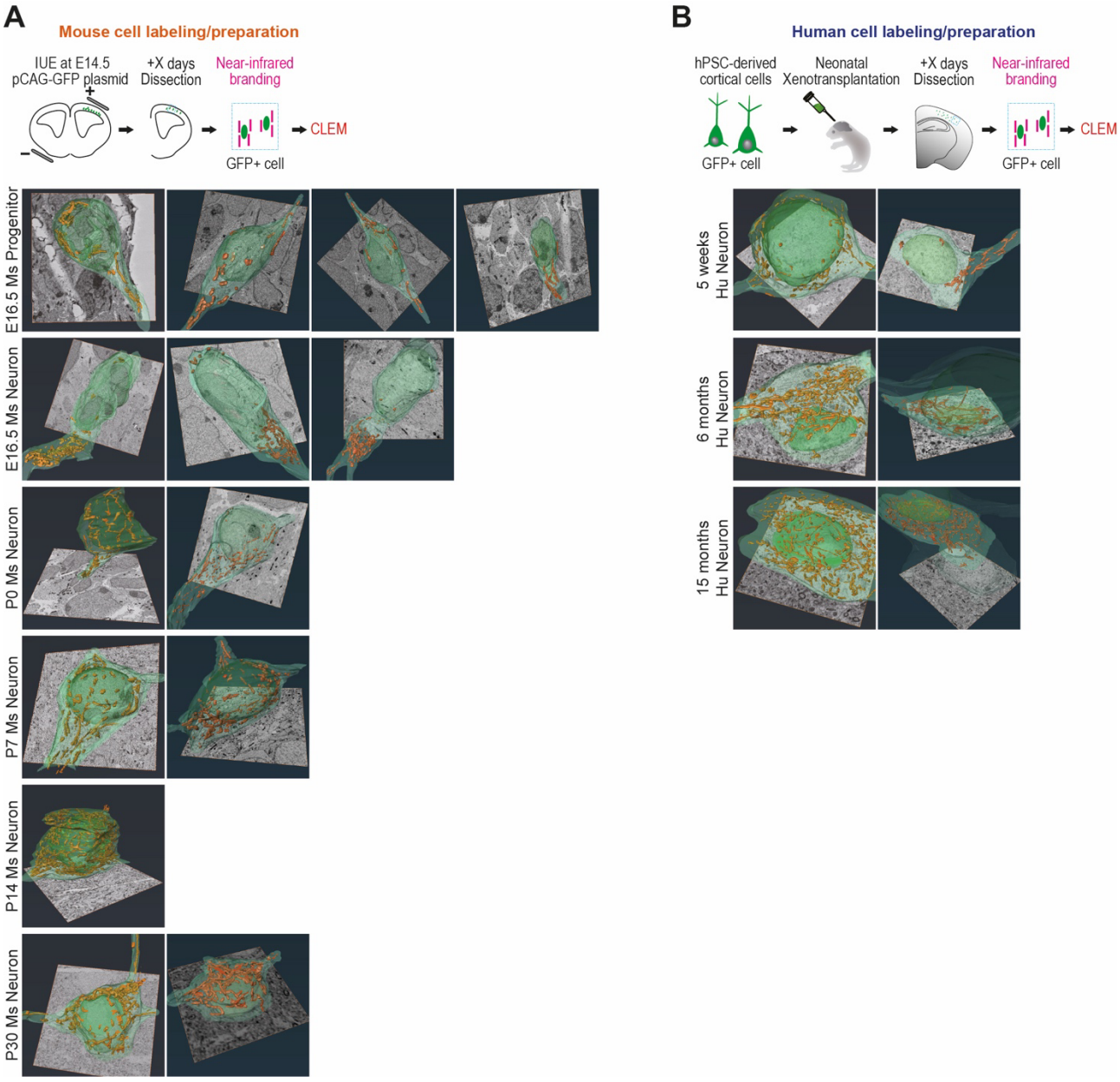


Figure 4. Electron microscopy study of mitochondrial growth and dynamics during cortical neuron maturation (A) Schematic of mouse (Ms) cortical neuron birth-dating by in utero electroporation (IUE) followed by correlative light and electron microscopy (CLEM), and representative images at indicated time-point following IUE. E: embryonic day. P: postnatal day. Yellow structure: Mitochondria. Bottom image: 20μm square. (B) Schematic of human (Hu) cortical neuron birth-dating followed by neonatal mouse cortex xenotransplantation used for CLEM, and representative image at indicated time-

point after neonatal xenotransplantation. Only a small part of the human neuron is modeled as a representative piece. Bottom image: 20μm square.

By using TEM (transmission electron microscopy) to visualize mitochondria ultrastructure in greater detail, we found that in newborn neuron mitochondria display a morphology with few cristae and an electron dense matrix. In contrast, they display more and better defined cristae, suggestive of functional maturation(*113–115*) as well as a decrease in electron density of the mitochondrial matrix during neuronal development, following a species-specific timeline, more protracted in human neurons (Fig.5).

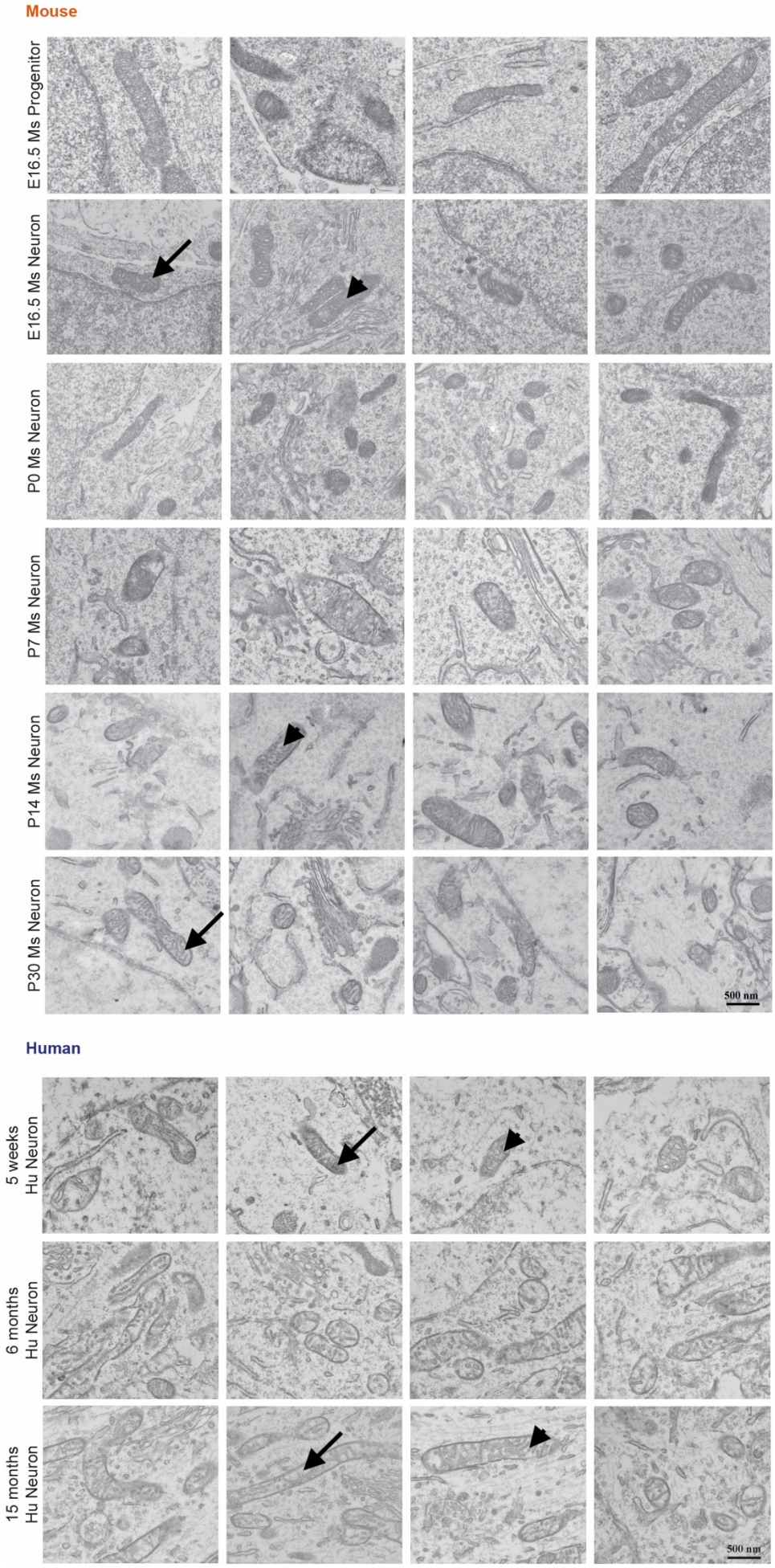

Mouse
E16.5 Ms Progenitor
E16.5 Ms Neuron
P0 Ms Neuron
P7 Ms Neuron
P14 Ms Neuron
P30 Ms Neuron
500 nm
Human
5 weeks Hu Neuron
6 months Hu Neuron
15 months Hu Neuron
500 nm

Figure 5. Ultrastructure of mitochondria of mouse and human cortical neurons during maturation. Representative images of mitochondria by transmission electron microscopy at indicated time-point of mouse and human cortical neurons, illustrating changes in mitochondrial matrix (arrows) and cristae (arrow heads).

Mitochondrial Metabolic Activity is Lower in Human than Mouse Developing Cortical Neurons

Next, we examined the functional properties of mitochondria during neuronal development, first focusing on mitochondrial oxidative phosphorylation (OXPHOS) and electron transport chain (ETC) capacity. We measured mitochondrial oxygen consumption rate (OCR) using Oxygraphy(*116*) on highly enriched preparations (>95% neurons) of birth-timed mouse and human cortical neurons (Fig.6A,B).

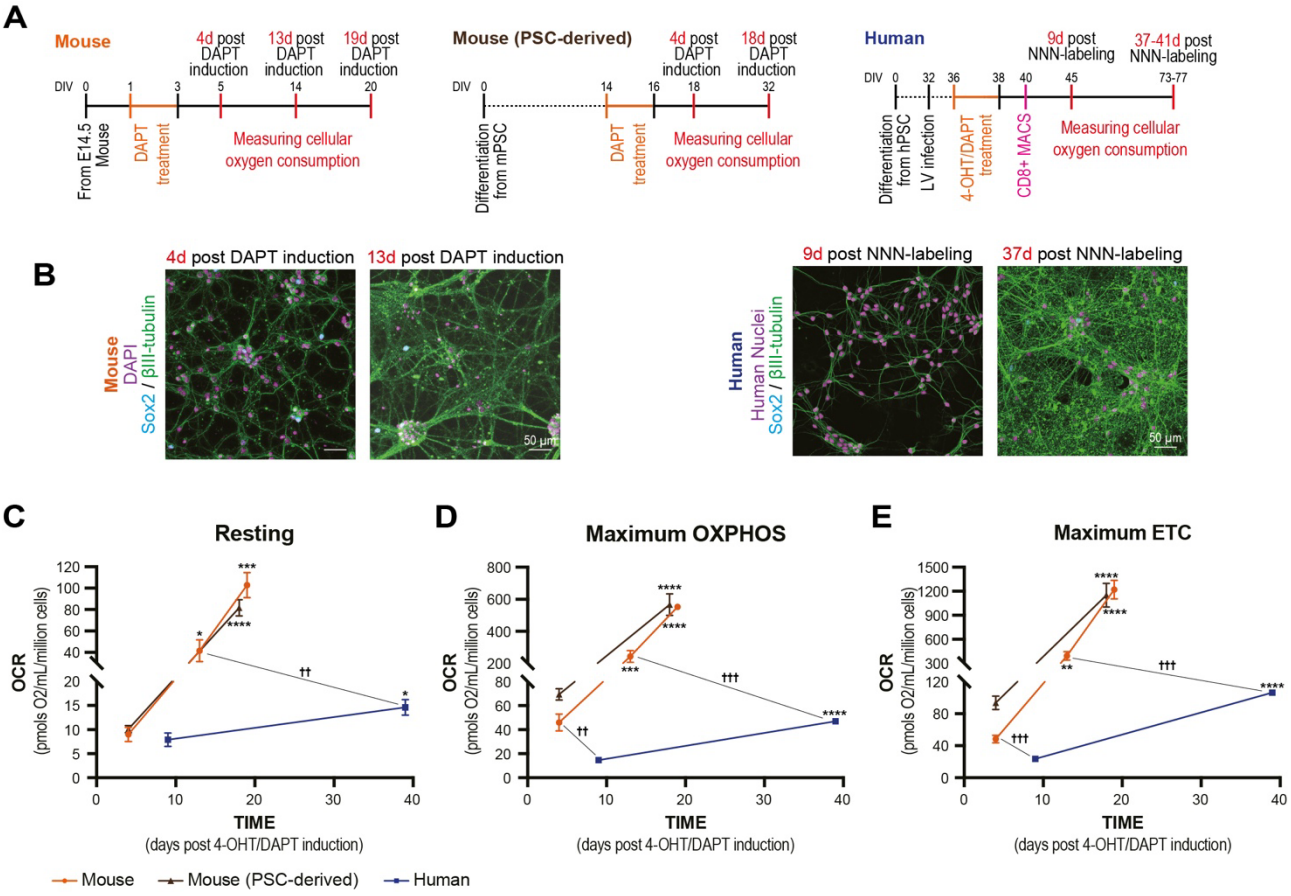


Figure 6. Changes in the oxygen consumption rate (OCR) during cortical neuron maturation and interspecies differences. (A) Experimental timeline of the experiments for OCR measurement during Mouse (primary), Mouse (PSC-derived) and Human cortical neuron maturation. (B) Representative

images of mouse and human neurons used for oxygraphy experiment. (C-E) Quantification of the OCR during neuronal development. Data are shown as mean ± SEM from at least two biological replicates. (C) Resting OCR. (D) Maximum oxidative phosphorylation (OXPHOS) capacity under coupled condition. (E) Maximum electron transport chain (ETC) capacity under uncoupled condition (uncoupler CCCP treated). Mouse (4, 13, 19 dp DAPT induction. N=6, 8, 4). PSC-derived Mouse (4, 18 days post DAPT induction. N=10, 7). Human (9, 37-41 dp NNN-labeling. N=6, 7). Dunn's or Dunnett's multiple comparisons test. Compared with first time point: *P < 0.05, **P < 0.01, ***P < 0.001, ****P < 0.0001. Compared mouse and human: Unpaired t test or Mann Whitney test. ††P < 0.01, †††P < 0.001.

From early stages, mitochondrial OCR was found to be higher in mouse than human neurons, and to increase much more rapidly in mouse than in human neurons, in line with their morphological development. As a result, stimulated OCR was found to be >10 times higher in mouse than in human counterparts after 2 weeks of differentiation (Fig.6C,D,E). The increasing mitochondria ETC activity during mouse neuronal development was confirmed by mitochondria membrane potential measurement using tetramethylrhodamine methyl ester (TMRM)(see Iwata, Casimir et al, Science 2023, ref. (*112*), Fig S5).

We next performed mass spectrometry-based ^{13}C tracer analysis(*117*) of enriched preparations of human and mouse cortical neurons (>95% neurons, data not shown) at similar ages (19 days following neuronal birth), focusing on glucose metabolism (Fig.7A). While this led to similar labeling of glycolytic metabolites in the two species, it revealed a higher enrichment of lactate from $^{13}C_6$-glucose and a higher secretion of lactate in human compared with mouse neurons (Fig.7B-F, Fig.9). On the other hand, the labeling of tricarboxylic acid (TCA) cycle metabolites was comparatively lower in human than in mouse neurons, indicating less mitochondria-driven metabolic activity (Fig.7B,C, Fig.9). In addition, we performed whole cell NAD^+ and NADH measurements, which revealed that while the levels of NAD^+ and NADH are both higher in human neurons, the NAD^+/NADH ratio tended to be lower than in mouse neurons, which may suggest a difference in NAD recovery and synthesis between two species (Fig.7H). We also found a much higher GSH/GSSG ratio in

human neurons, indicating a lower oxidative stress pressure in human cells (Fig.7G), consistent with a lower activity of the mitochondrial ETC, which can be source of reactive oxygen species.

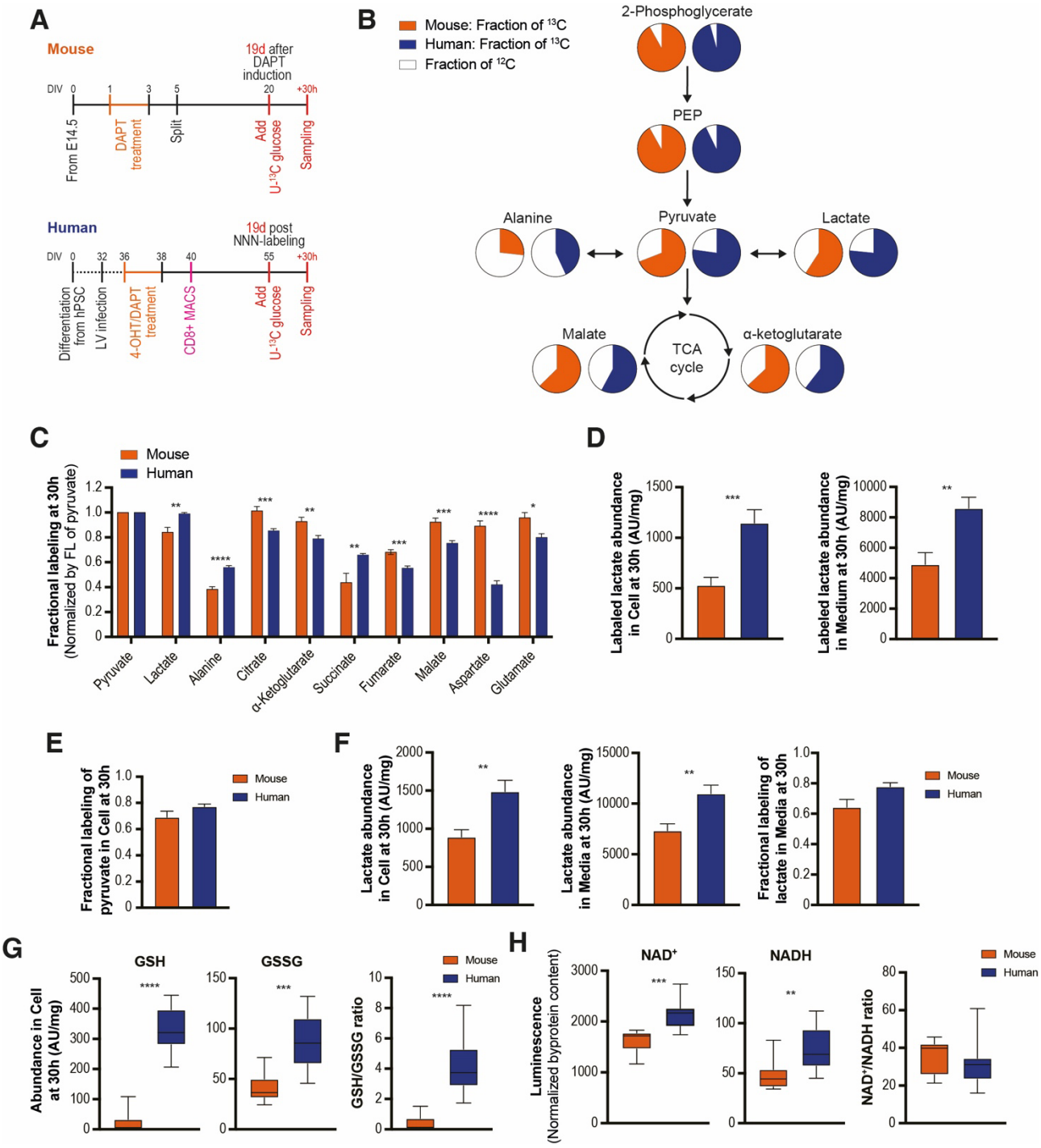


Figure 7. Interspecies differences in mitochondria metabolism during neuronal development. (A) Experimental timelines for metabolomics experiments during Mouse and Human cortical neuron maturation. (B) ^{13}C enrichment patterns of the metabolites in Mouse (Orange) and Human (Blue). Mouse: N=9, Human: N=9. PEP: Phosphoenolpyruvate. (C) Fractional labeling of metabolites normalized by the labelled fraction of pyruvate at 30h post tracer addition in 19 days post DAPT induction/NNN labeling

neurons. Mouse: N=9, Human: N=9. (D) ^{13}C-labeled lactate abundance in cell (Left) and in medium (Right) at 30h post tracer addition. Mouse: N=9, Human: N=9. (E) Fractional labeling of pyruvate in Cell at 30h post tracer addition. (F) Lactate abundance in Cell (Left) and Medium (Middle) and Fractional labeling of Lactate in the Medium (Right) at 30h post tracer addition. (G) Abundance of reduced Glutathione (GSH) (Left) and oxidized Glutathione (GSSG) (Middle) and GSH/GSSG ratio (Right) at 30h post tracer addition. (H) Whole cell abundance of NAD^+ (Left) and NADH (Middle) and NAD^+/NADH ratio (Right) in 12 days post DAPT induction/NNN labeling neurons. Mouse: N=9, Human: N=9. Data are shown as mean ± SEM. AU: arbitrary units. Unpaired t test or Mann Whitney test. *P < 0.05, **P < 0.01, ***P < 0.001, ****P < 0.0001.

Finally, ATP and ADP levels and ATP/ADP ratios were found to be higher in human than mouse neurons (Fig.8D), while their fractional labeling from glucose was lower (Fig.8B), suggesting more de novo biosynthesis of ATP/ADP in mouse neurons (Fig.8A). Consistent with this result, the fractional labelling of Acetyl-CoA from glucose showed a higher m+5 labeling (5 carbons in CoenzymeA from ATP) and a higher m+7 labeling (5 carbons in CoA from ATP + 2 carbons in the acetyl group from pyruvate) in mouse than in human (Fig.8A,C). Finally, we performed the same ^{13}C glucose tracer metabolomics experiment on another earlier time point, that is 12 days after neuronal birth, to see if the changes observed in mitochondrial growth and OXPHOS activity during neuron maturation were matched by changes in metabolite enrichment in glycolysis and TCA cycle. In each species, few differences were observed between the two time points. In mouse, a trend towards an increase in the labeling of metabolites from the TCA cycle was observed that was significant only for citrate. In human, a trend towards a decrease in aerobic glycolysis was observed in the form of a significant decrease in the labeling of lactate (Fig.8E-H). Measurements of metabolic labeling from ^{13}C glucose at earlier time points in mouse cells and later time points in human cells would be required to further document changes in metabolism during maturation and the difference in their kinetics between species. Collectively, these data indicate that human developing cortical neurons display lower levels of mitochondria-driven TCA cycle and oxidative activity than their mouse counterparts at similar birth-time.

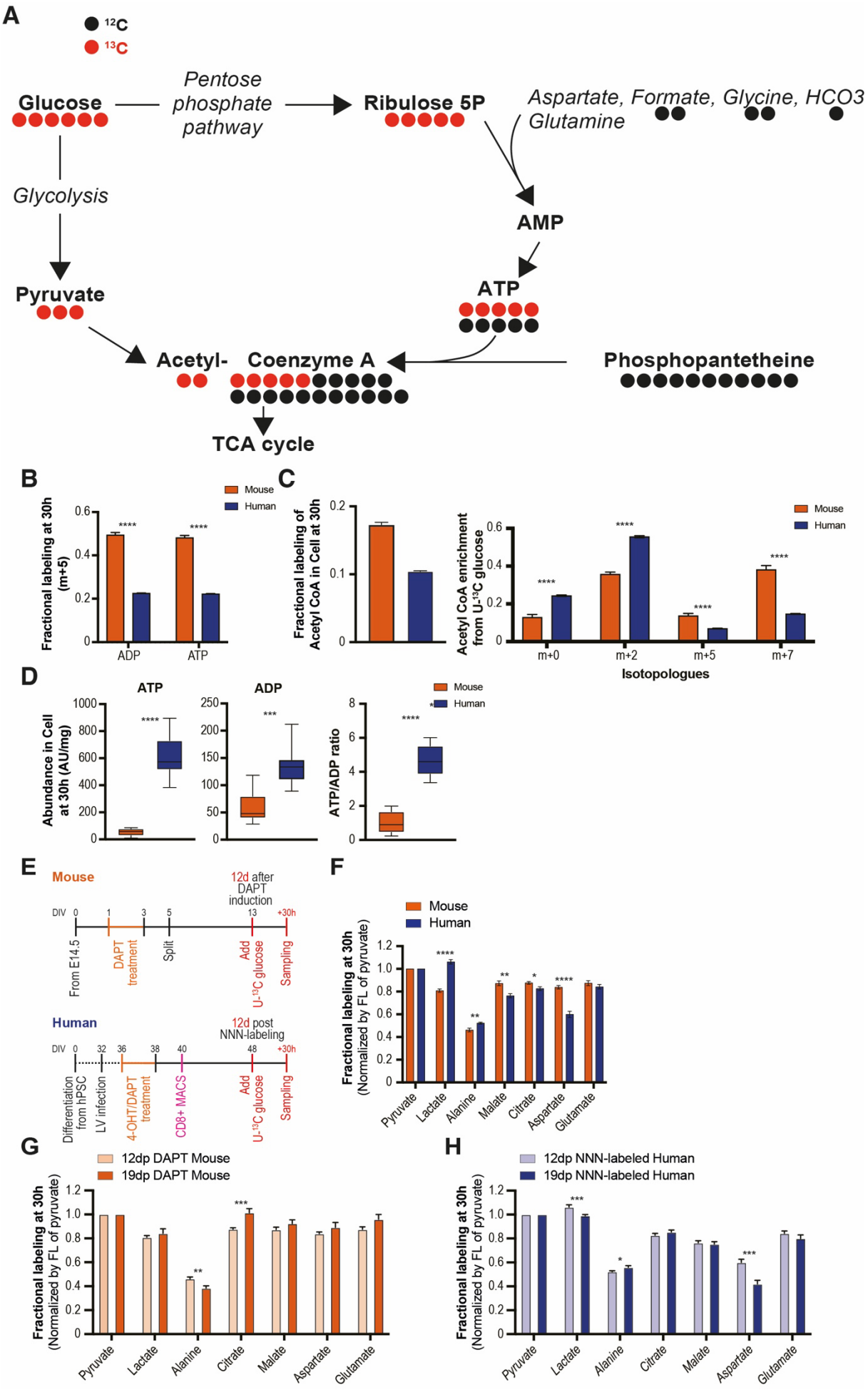

A
12C
13C
Glucose
Pentose phosphate pathway
Ribulose 5P
Aspartate, Formate, Glycine, HCO3
Glutamine
Glycolysis
AMP
Pyruvate
ATP
Acetyl-
Coenzyme A
Phosphopantetheine
TCA cycle
B
Mouse
Human
Fractional labeling at 30h (m+5)
ADP
ATP
C
Fractional labeling of Acetyl CoA in Cell at 30h
Acetyl CoA enrichment from U-13C glucose
m+0
m+2
m+5
m+7
Isotopologues
D
ATP
ADP
Abundance in Cell at 30h (AU/mg)
ATP/ADP ratio
E
Mouse
12d after DAPT induction
DIV
From E14.5
DAPT treatment
Split
Add U-13C glucose
Sampling
Human
12d post NNN-labeling
Differentiation from hPSC
LV infection
4-OHT/DAPT treatment
CD8+ MACS
F
Fractional labeling at 30h (Normalized by FL of pyruvate)
Pyruvate
Lactate
Alanine
Malate
Citrate
Aspartate
Glutamate
G
12dp DAPT Mouse
19dp DAPT Mouse
H
12dp NNN-labeled Human
19dp NNN-labeled Human

Figure 8. U-^{13}C glucose tracing and targeted metabolites in mouse and human cortical cells. (A) Schematic of the labeling of ATP and Acetyl-Coenzyme A from U-^{13}C glucose. (B) m+5 fractional enrichment of ADP and ATP. Data are shown as mean ± SEM. Mouse & Human (N=9). Unpaired t test. (C) Fractional labeling of Acetyl CoA (Left). Isotopologue distribution following ^{13}C for Acetyl CoA (Right). Data are shown as mean ± SEM. Mouse & Human (N=9). Unpaired t test. (D) Abundance of ATP and ADP in cell (Left & Middle). ATP/ADP ratio (Right). Data are shown as mean ± SEM. Mouse & Human (N=9). Unpaired t test or Mann-Whitney test. (E) Experimental timelines for metabolomics experiments during Mouse and Human cortical neuron maturation. (F) Fractional labeling of metabolites normalized by the labelled fraction of pyruvate at 30h post tracer addition in 12 days post DAPT induction/NNN labeling neurons. Mouse: N=12, Human: N=9. (G) Fractional labeling of metabolites normalized by the labelled fraction of pyruvate at 30h post tracer addition in 12 versus 19 days post DAPT induction Mouse neurons. 12 days post DAPT induction: N=12, 19 days post DAPT induction: N=9. (H) Fractional labeling of metabolites normalized by the labelled fraction of pyruvate at 30h post tracer addition in 12 versus 19 days post NNN labeling Human neurons. 12 days post DAPT induction: N=9, 19 days post DAPT induction: N=9. Data are shown as mean ± SEM. AU: arbitrary units. Unpaired t test or Mann Whitney test. *P < 0.05, **P < 0.01, ***P < 0.001, ****P < 0.0001.

Our oxygraphy data point to a strong temporal patterning of mitochondria metabolism during neuronal maturation. To gain insights on the upstream mechanisms and *in vivo* relevance of these observations, we examined our scRNA-seq of *in vitro* birth-dated human neurons, together with *in vivo* human and mouse fetal cortex scRNA-seq datasets(*118*, *119*), focusing on mitochondria and metabolism genes. This revealed a temporal increase of mitochondria metabolism-related genes including the TCA cycle and OXPHOS pathways during neuronal maturation (see Iwata, Casimir et al, Science 2023, ref(*112*), Fig. 3F,J, Table S2), thus highly consistent with the oxygraphy data. The *in vitro* and *in vivo* patterns of expression of mitochondria/metabolic genes were highly similar and correlated (see Iwata, Casimir et al, Science 2023, ref(*112*), Fig.3E,F), thus providing direct *in vivo* validation for our *in vitro* observations. Human and mouse comparison revealed similar temporal patterning of mitochondria/metabolic genes, with an overall increase in genes related to oxidative phosphorylation and decrease of genes related to glycolysis, but at a higher speed in mouse than human neurons (see Iwata, Casimir et al, Science 2023, ref(*112*), Fig.3J).

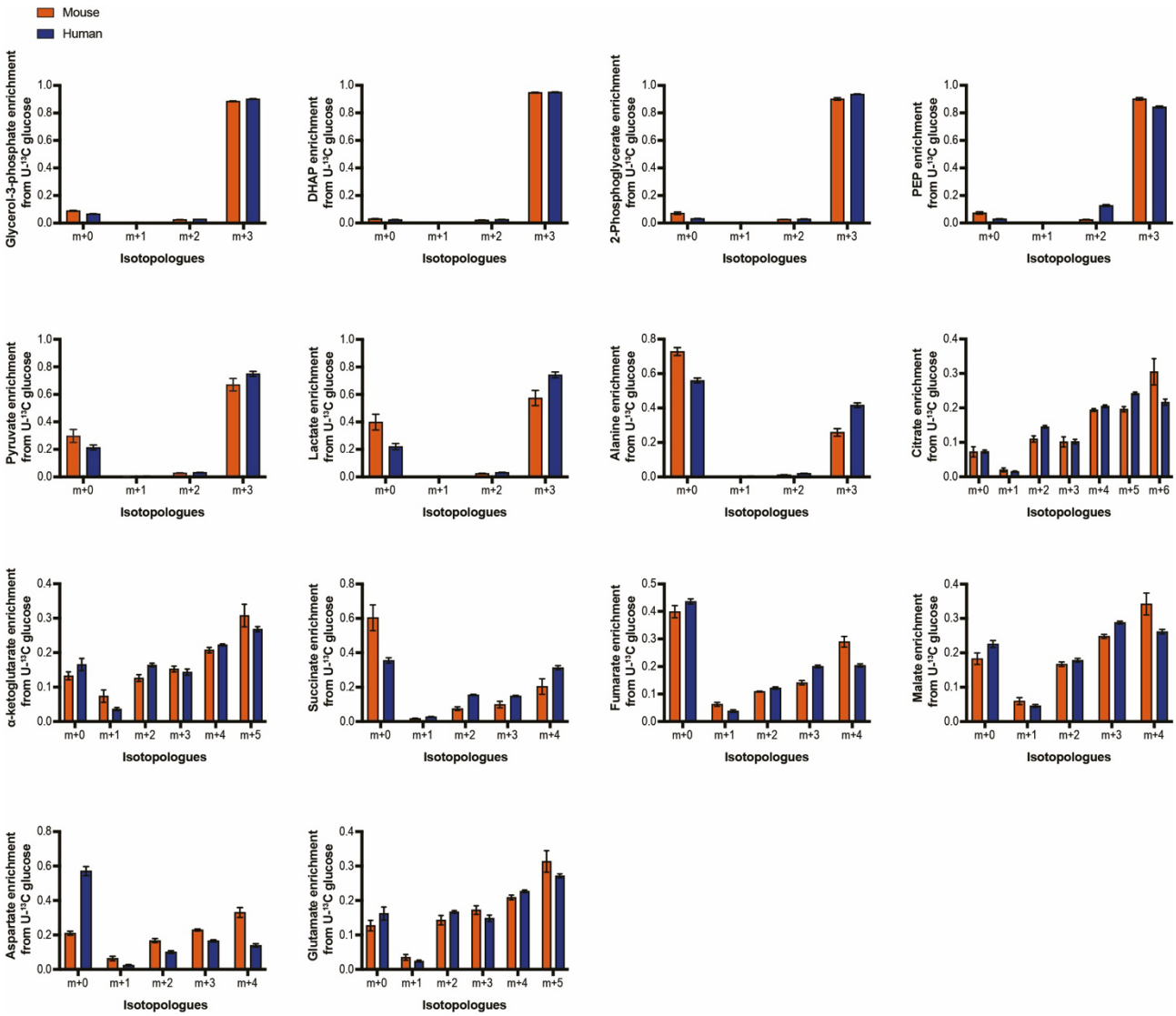


Figure 9. Isotopologue distribution following U-^{13}C glucose tracing. Data are shown as mean ± SEM. Mouse & Human (N=9).

Increasing Mitochondria Activity in Human Neurons leads to Accelerated Neuronal Maturation, Growth and Complexification

We next tested whether the species differences observed in mitochondria metabolic functions could be causally linked to the speed of neuronal maturation. Glucose tracer experiments revealed an interspecies difference in the pyruvate to lactate conversion (Fig.7,8,9), which is catalyzed by lactate dehydrogenase (LDH). LDH is a tetrameric enzyme with isoenzymes composed of different proportions of two common subunits, A and B. Both enzymes were expressed in mouse and human cortical neurons, with higher levels in human

than mouse (see Iwata, Casimir et al, Science 2023, ref(*112*), Fig.S12). LDHA favors the conversion of pyruvate to lactate, and LDHB favors the conversion of lactate to pyruvate(*120*) (Fig.10A). To increase mitochondria activity in developing neurons, we therefore targeted the activity of LDHA. As expected, treatment with a chemical inhibitor of LDHA, GSK-2837808A (referred to as GSK) (*121*), resulted in increased mitochondria oxidative activity in human neurons, as measured by mitochondria OCR (Fig.10B). This result is consistent with previous reports in cancer cells, in which genetic depletion of LDHA increases mitochondrial OXPHOS activity (*122*).

We tested additional treatments predicted to increase mitochondria oxidative phosphorylation. These include preparations of free fatty acids (FFAs) (AlbuMAX), an additional fuel besides glucose for mitochondrial TCA cycle activity. AlbuMAX treatment also led to increased OCR, including additive effects of LDH inhibition and FFA (referred to as AlbuMAX/GSK) treatments (Fig.10A,B). Importantly, these treatments, alone or in combination, all led to a significant increase of OCR, but not to the level found in mouse neurons (Fig.6C-E, Fig.10B), even with higher concentrations of LHDA inhibitor (Fig.13).

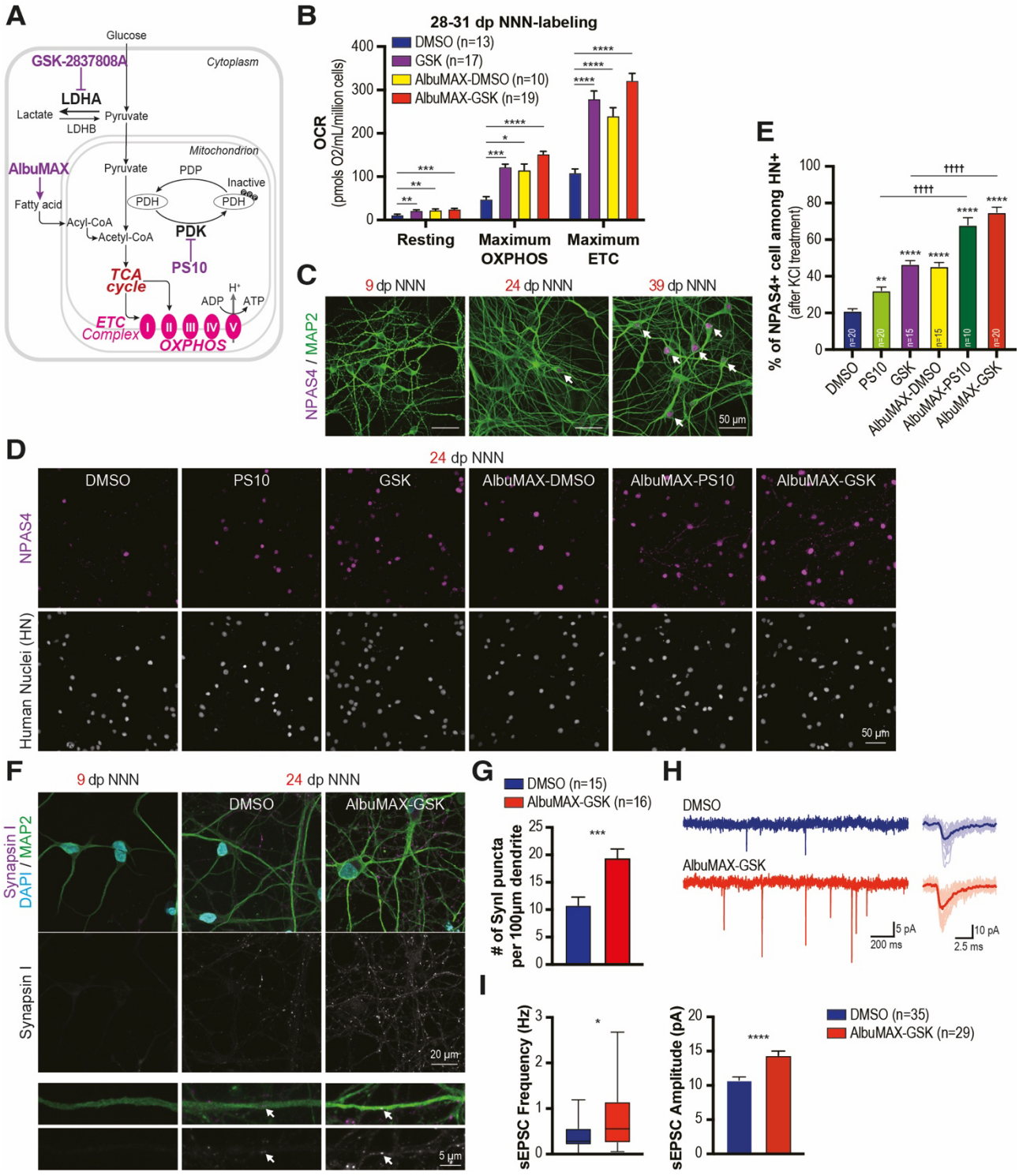


Figure 10. Increasing mitochondria metabolism accelerates human neuronal maturation. (A) Schematic of metabolic pathways targeted by indicated chemical compounds. GSK: GSK-2837808A. LDHA/B: lactate dehydrogenase A/B. PDH: pyruvate dehydrogenase. PDK/P: pyruvate dehydrogenase kinase/phosphatase (B) Quantified OCR from more than three biological replicate experiments. Data are shown as mean ± SEM. DMSO: N=13, GSK: N=17, AlbuMAX-DMSO: N=10, AlbuMAX-GSK: N=19. Dunnett's or Dunn's multiple comparisons test. (C) Representative images of KCl-induced NPAS4 expression in NNN-labeled human neurons over time. Arrow: NPAS4+ neurons. (D) Representative images of the number of NPAS4 positive neurons induced by KCl following treatment with indicated

chemical compounds. (E) Quantification of the proportion of NPAS4-positive neurons among all neurons (human-specific nuclear antigen) induced by KCl following treatment with indicated chemical compounds from three independent biological replicates. Data are shown as mean ± SEM DMSO: N=20, PS10: N=20, GSK: N=15, AlbuMAX-DMSO: N=15, AlbuMAX-PS10: N=20, AlbuMAX-GSK: N=20 ROIs. Tukey's multiple comparisons test. (F) Representative images of synapsin I staining in NNN-labeled human neurons. (G) Quantification of the number of synapsin I puncta on dendrites from three independent biological replicates. Data are shown as mean ± SEM. DMSO: N=15, AlbuMAX+GSK: N=16. Unpaired t test. Arrow: synapsin I puncta on dendrite. (H) Trace of spontaneous excitatory postsynaptic current (sEPSC). (I) Quantification of sEPSC frequency (Left) and amplitude (Right) from four independent biological replicates. Data are shown as mean ± SEM. DMSO: N=35, AlbuMAX-GSK: N=29 neurons. Unpaired t test or Mann-Whitney test. *P < 0.05, **P < 0.01, ***P < 0.001, ****P < 0.0001, ††††P < 0.0001.

We also examined the impact of AlbuMAX/GSK treatment, which showed the highest OCR, on mitochondria morphology and protein composition. Morphology analyses did not reveal significant effects of treatment on mitochondria length and volume (Fig.11A-C).

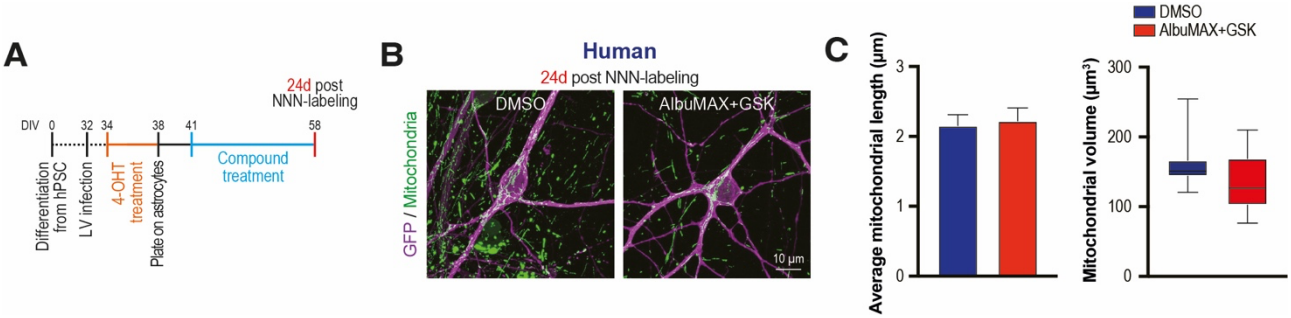


Figure 11. Mitochondria enhancing treatments effect on mitochondrial morphology. (A) Timeline of experiments to assess the effect of mitochondria enhancing treatments on mitochondrial morphology and quantity. (B) Representative images of mitochondrial morphology in NNN-labeled human neurons in DMSO (Left) and AlbuMAX/GSK treated (Right) conditions. (C) Quantification of Average mitochondria length (Left) and volume (Right). Data are shown as mean ± SEM. DMSO: N=10, AlbuMAX-GSK: N=13 neurons. Unpaired t test or Mann-Whitney test.

Similarly, Western blot analyses revealed that the levels of most tested mitochondria proteins remain unchanged. However, some important components were increased following the treatment, specifically COXII, a component of complex IV (see Iwata, Casimir et al, Science 2023, ref(*112*) Fig, S17). Importantly, the effects of AlbuMAX/GSK treatments

on OCR could still be detected 1-5 days after arrest of the treatment (Fig.12A-E). Overall these data suggest that there is no global effect of LDH inhibition on mitochondria biogenesis or dynamics, but rather a selective molecular and metabolic remodeling leading to increased oxidative phosphorylation. Finally, none of the treatments enhancing mitochondria led to neuronal toxicity or changes in neuronal identity as levels of apoptosis remained equally low and identity marker stable following AlbuMAX/GSK treatments (see Iwata, Casimir et al, Science 2023, ref(*112*), Fig. S13E, S16A-E).

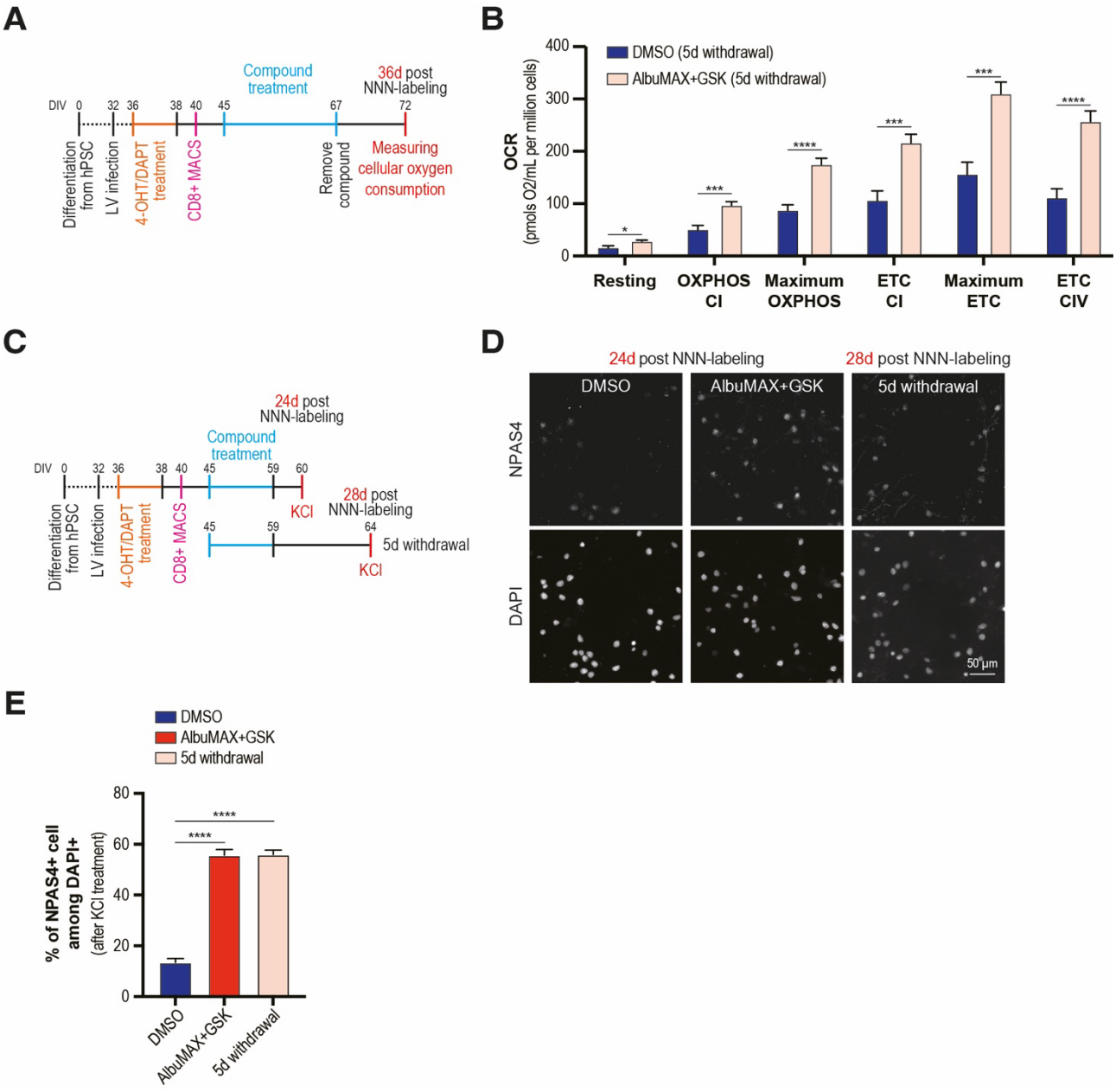


Figure 12. Irreversibility of treatment effect on human cortical neuron mitochondria activity and excitability. (A) Experimental scheme. At day 67, media were changed to fresh media without chemical

compound for 5d withdrawal group. (B) Quantified OCR from three biological replicate experiments. Data are shown as mean ± SEM. DMSO (5d withdrawal): N=10, AlbuMAX-GSK (5d withdrawal): N=8. (C) Experimental scheme. At day 40, MACS-sorted cells were plated on coverslip without mouse astrocytes. At day 59, the media were changed to fresh media without chemical compounds. (D) Representative images of KCl-induced NPAS4 expression following treatment with indicated chemical compounds. (E) Quantification of the proportion of NPAS4+ cells among DAPI+ cells from three biological replicate experiments. Data are shown as mean ± SEM. N=15 ROIs for each condition. Tukey's or Dunn's multiple comparisons test. *P < 0.05, **P < 0.01, ***P < 0.001, ****P < 0.0001.

Next, we tested the impact of these treatments on neuronal maturation rates. To probe the speed of maturation we assessed the classical parameter of neuronal excitability, by measuring their ability to respond to membrane depolarization following KCl addition, using as a read-out the expression of the activity-dependent immediate early gene NPAS4(*123*, *124*). We thus found that very few NNN-labeled human cortical neurons respond to KCl shortly after their birth (9-24 days), while most of them become responsive only weeks later (39 days) (Fig.10C).

We then examined the impact of LDHA inhibitors on human cortical neuron maturation, by treating the cells from day 9 to 23, when the neurons are still poorly responsive to KCl depolarization (Fig.10D,E). The LDH inhibitor treatment was stopped for 1-5 days before assessing maturation, to distinguish genuine effects of the treatments on mitochondria and neuronal development from an acute impact on mitochondria function (Fig.10C-E, Fig.12). While in control conditions, few neurons at day 24 responded to KCl treatment, as expected (Fig.10C-E), prior inhibition of LDHA led to a major increase in the proportion of neurons displaying NPAS4 responses, indicating an acceleration of neuronal maturation in response to increased mitochondria respiration (Fig.10C-E). Increased neuronal maturation was also observed with other mitochondria enhancing treatments including AlbuMAX , as well as PS10, a PDH kinase (PDK1-4) inhibitor(*125*), that also stimulates mitochondrial metabolism by increasing the conversion of Pyruvate into Acetyl-CoA. Interestingly, the effects of AlbuMax and LDHA inhibition were additive (Fig.10E), further pointing to mitochondrial

metabolic activity as an important driver of the speed of neuronal maturation. Finally, as these experiments were performed on human cortical neurons cultured on mouse astrocytes (Fig.10), we tested the impact of the same compounds on pure neuronal populations, which resulted in the same degree of acceleration of neuronal maturation (see Iwata, Casimir et al, Science 2023, ref(*112*), Fig. S13F-H, S14C-E, S15C-E), indicating that the effects observed are intrinsic to cortical neurons and do not require astrocytes.

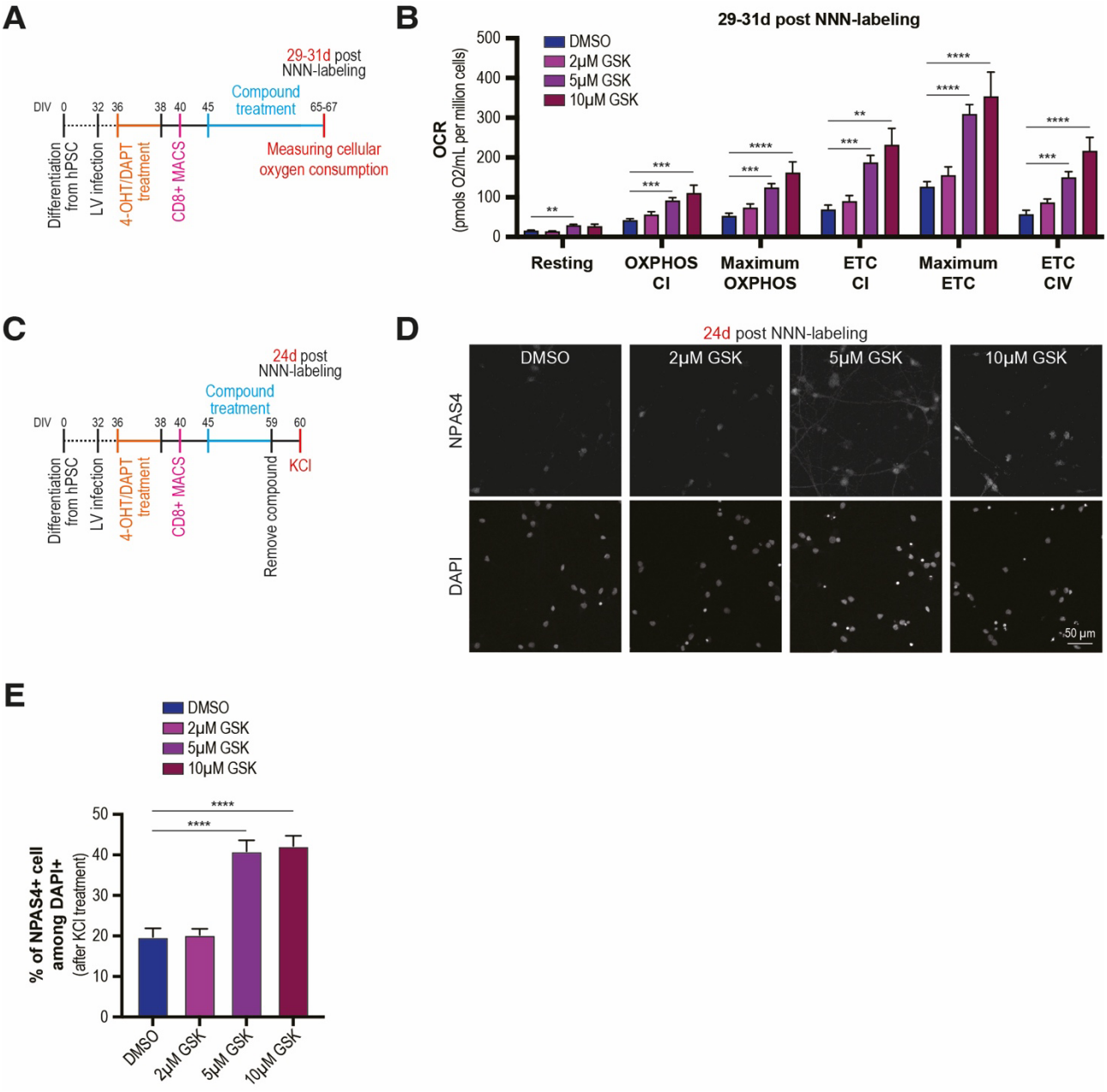


Figure 13. Dosage-dependent impact of LDHA inhibitor on human cortical neuron mitochondria activity and excitability. (A) Experimental scheme and (B) quantified OCR from four biological replicate experiments. Data are shown as mean ± SEM. DMSO: N=9, 2µM GSK: N=8, 5µM GSK: N=13, 10µM

GSK: N=7. Dunnett's or Dunn's multiple comparison test. (C) Experimental scheme. At day 40, MACS-sorted cells were plated on coverslip without mouse astrocytes. (D) Representative images of KCl-induced NPAS4 expression following treatment with indicated chemical compounds. (E) Quantification of the proportion of NPAS4+ cells among DAPI+ cells from three biological replicate experiments. Data are shown as mean ± SEM. N=15 ROIs for each condition. Tukey's multiple comparisons test. **P < 0.01, ***P < 0.001, ****P < 0.0001.

These data suggest that increased mitochondria activation leads to accelerated neuronal differentiation. We tested this further by performing patch-clamp recordings of human cortical neurons following 22-30 days of AlbuMAX/GSK treatment. Strikingly this resulted in increased frequency and amplitude of synaptic currents (Fig.10H,I), together with an increase of membrane potential (see Iwata, Casimir et al, Science 2023, ref(*112*), Fig. S18), consistent with the global increase in the differentiation of the treated neurons. Consistent with synaptic currents changes, we found an increased number of pre-synaptic marker synapsin I puncta on dendrites in treated neurons (Fig.10F,G). Notably however, the density of synapsin I puncta in 24 days-old AlbuMAX/GSK-treated human neurons was still lower than 13 days-old mouse neurons (Fig.10F, Fig.14).

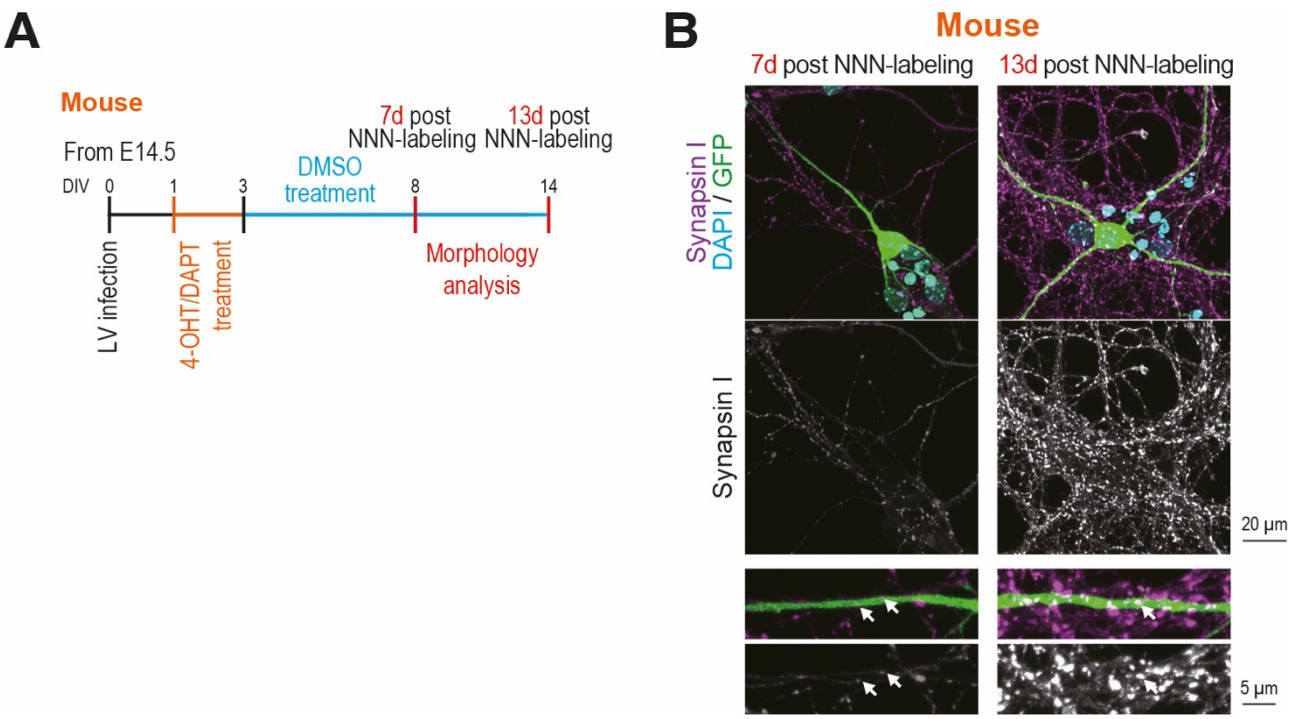


Figure 14. Characterization of maturing Mouse cortical neurons. (A) Experimental timeline and (B) Representative images of synapsin I positive puncta on mouse dendrites at different stages of mouse cortical neurons.

We then examined the global consequences of mitochondria-enhancing treatments on neuronal size and dendritic length, as well as branching of dendritic arbors, which constitute crucial aspects of neuronal maturation. AlbuMAX/GSK-treated human cortical neurons displayed strikingly larger neuronal size and increased dendritic length and complexity (Fig.15A,B). Remarkably, the growth and complexity pattern of 24 days-old neurons treated with AlbuMAX/GSK reached at least the same maturation level as for control neurons 58 days after their birth (Fig.2B, Fig.15A), indicating that mitochondria enhancement accelerates neuronal development towards growth and complexity several weeks ahead of time.

To explore the relevance of these observations across species, we next tested whether mitochondria activity could influence rates of maturation in mouse neurons (Fig.15C-J). Mitochondria enhancing with AlbuMAX/GSK in mouse neurons resulted in increased dendritic length and complexity (Fig.15C-E). Conversely, reduction of mitochondria activity, using either UK-5099 as a mitochondrial pyruvate carrier inhibitor, or Rotenone as an ETC complex I inhibitor, resulted in decreased growth of dendrites, consistent with slower rates of development (Fig.15E-J).

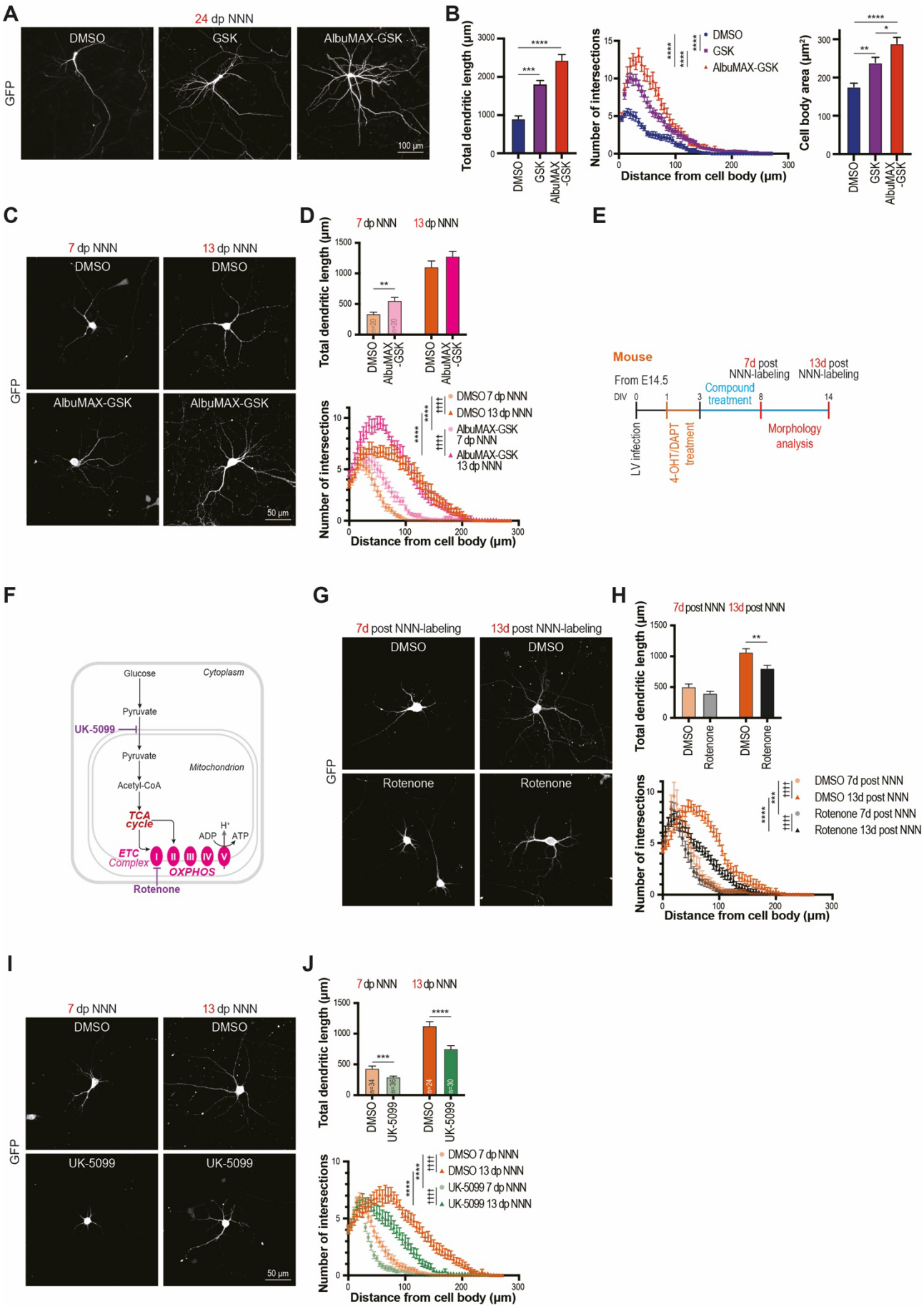

A
24 dp NNN
DMSO
GSK
AlbuMAX-GSK
GFP
100 µm
B
Total dendritic length (µm)
Number of intersections
Distance from cell body (µm)
Cell body area (µm²)
DMSO
GSK
AlbuMAX-GSK
C
7 dp NNN
13 dp NNN
DMSO
AlbuMAX-GSK
GFP
50 µm
D
7 dp NNN
13 dp NNN
Total dendritic length (µm)
Number of intersections
Distance from cell body (µm)
DMSO 7 dp NNN
DMSO 13 dp NNN
AlbuMAX-GSK 7 dp NNN
AlbuMAX-GSK 13 dp NNN
E
Mouse
From E14.5
DIV
LV infection
4-OHT/DAPT treatment
Compound treatment
7d post NNN-labeling
13d post NNN-labeling
Morphology analysis
F
Glucose
Cytoplasm
Pyruvate
UK-5099
Mitochondrion
Acetyl-CoA
TCA cycle
ADP
ATP
ETC Complex
OXPHOS
Rotenone
G
7d post NNN-labeling
13d post NNN-labeling
DMSO
Rotenone
GFP
H
7d post NNN
13d post NNN
Total dendritic length (µm)
Number of intersections
Distance from cell body (µm)
DMSO 7d post NNN
DMSO 13d post NNN
Rotenone 7d post NNN
Rotenone 13d post NNN
I
7 dp NNN
13 dp NNN
DMSO
UK-5099
GFP
50 µm
J
7 dp NNN
13 dp NNN
Total dendritic length (µm)
Number of intersections
Distance from cell body (µm)
DMSO 7 dp NNN
DMSO 13 dp NNN
UK-5099 7 dp NNN
UK-5099 13 dp NNN

Figure 15. Functional coupling between mitochondria metabolism and neuronal development across species. (A) Representative images of NNN-labeled human neurons following treatment with indicated chemical compounds. (B) Quantification of neuronal morphology analysis from two biological replicates. N=20 neurons for each condition. Data are shown as mean ± SEM. (Left) Total dendritic length. Dunn's multiple comparisons test. (Middle) Sholl analysis of dendritic branching. Two-way ANOVA test. (Right) Cell body area. Tukey's multiple comparisons test. (C) Representative images of indicated chemical compounds NNN-labeled mouse neurons. (D) Quantification of total dendritic length (Top) and sholl analysis of dendritic branching (Bottom) from three biological replicates. Data are shown as mean ± SEM. DMSO (Concentration: 1/4000. 7, 13 dp NNN-labeling. N=20, 17), AlbuMAX-GSK (7, 13 dp NNN-labeling. N=20, 20). (E) Experimental timeline for chemical compound treatment in Mouse NNN-labeled cortical neurons. (F) Schematic of metabolic pathways targeted by indicated chemical compounds (G) Representative images of indicated chemical compounds NNN-labeled mouse neurons. (H) Quantification of total dendritic length (Left) and sholl analysis of dendritic branching (Right) from three biological replicates. Data are shown as mean ± SEM. DMSO (Concentration: 1/5000000. 7, 13 days post NNN-labeling. N=16, 32), Rotenone (Concentration: 21nM, 7, 13 days post NNN-labeling. N=21, 33). (I) Representative images of indicated chemical compounds NNN-labeled mouse neurons. (J) Quantification of total dendritic length (Top) and sholl analysis of dendritic branching (Bottom) from three biological replicates. Data are shown as mean ± SEM. DMSO (Concentration: 1/40000. 7, 13 dp NNN-labeling. N=34, 24), UK-5099 (Concentration: 2.5μM. 7, 13 dp NNN-labeling. N=36, 30). Unpaired t test or Mann-Whitney test for dendritic length. Two-way ANOVA test for sholl analysis. *P < 0.05, **P < 0.01, ***P < 0.001, ****P < 0.0001. ††††P < 0.0001.

Finally, we tested whether the effects could be observed *in vivo*, taking advantage of a xenotransplantation model of human cortical neurons in the mouse neonatal cortex, in which human neurons develop along their species-specific timeline(*18*, *38*). We first performed genetic manipulation of human neuron metabolism, by lentiviral overexpression of LDHB or eGFP alone as a control, which resulted in increased mitochondria OCR, as expected (see Iwata, Casimir et al, Science 2023, ref(*112*) Fig.6A). We next xenotransplanted the transduced neurons, which revealed an increase in dendritic length and complexity 4 weeks post-transplantation (see Iwata, Casimir et al, Science 2023, ref(*112*), Fig.6A-D), corresponding to a pattern found typically at 2-3 months in control conditions(*38*). While further analyses of the LDHB-treated neurons will be required at later stages to address their

functionality, these data indicate that increasing mitochondria metabolic activity results in acceleration of human neuronal differentiation also during *in vivo* differentiation.

Effects of Increasing Mitochondria Activity in Human Cortical Neurons on Protein Turnover

Given the correlation between protein turnover and lifespan and body size(*101*, *102*), as well as recent studies suggesting an association between protein turnover and species-specific development timing of motor neurons(*105*) and of the segmentation clock(*106*), we next examined the protein turnover in mouse and human maturing cortical neurons. We performed a Stable Isotope Labeling of Amino acids in Cell culture (SILAC)(*126*) experiment in combination with liquid chromatography-mass spectrometry (LC-MS/MS) analysis using enriched preparations of mouse and human cortical neurons. These cultures are composed of more than 95% of neurons which are non-dividing cells, ensuring that the cell proliferation rate does not interfere with the measured kinetics of isotopic labeling. The SILAC labeling with isotope labeled Lysin and Arginine was started in immature neurons for both species (5 days post DAPT induction in mouse neurons, 14 days after DAPT induction/10 days post MACS sorting in human neurons) and performed during 1, 3 and 6 days (Fig.16A). The measured fractional labeling of identified proteins at the different time points allowed to calculate protein half-lives following the kinetic model outlined in the materials and methods section. The fractional labelling was quantified for 2091 peptides that were mapped to 833 proteins in mouse, and for 974 peptides that were mapped to 511 proteins in human (Fig.16B). The distribution of protein half-lives for all identified proteins, as well as for 256 ortholog proteins shared between mouse and human, revealed a shift towards shorter protein half-lives in mouse compared to human (83% of ortholog proteins for which the half-life in mouse cells is on average half of the half-life in human cells) that was significant for 109 proteins (42% of ortholog proteins) (Fig.16C,D), consistent with previous observations

in other cell types and contexts(*102*, *105*, *106*, *127*). We next examined the impact of GSK/AlbuMAX treatment on protein turnover rate during human cortical neuron maturation by treating the cells from day 9 to 20 and performing the SILAC labeling from day 14 to 20. The fractional labelling was quantified for 1025 peptides that were mapped to 468 proteins. The distribution of protein half-lives of GSK/AlbuMAX treated and untreated cells showed a trend for a slight shift towards shorter half-lives in treated cells (77% of proteins for which the half-life in GSK/AlbuMAX treated cells is on average 87% of the half-life in untreated cells), that was significant for only 53 proteins (14,6%) (Fig.16F,G). Overall this suggests that protein turnover is faster in mouse than in human maturing cortical neurons and that mitochondria enhancing treatment could accelerate protein turnover in human neurons although this question requires further investigation.

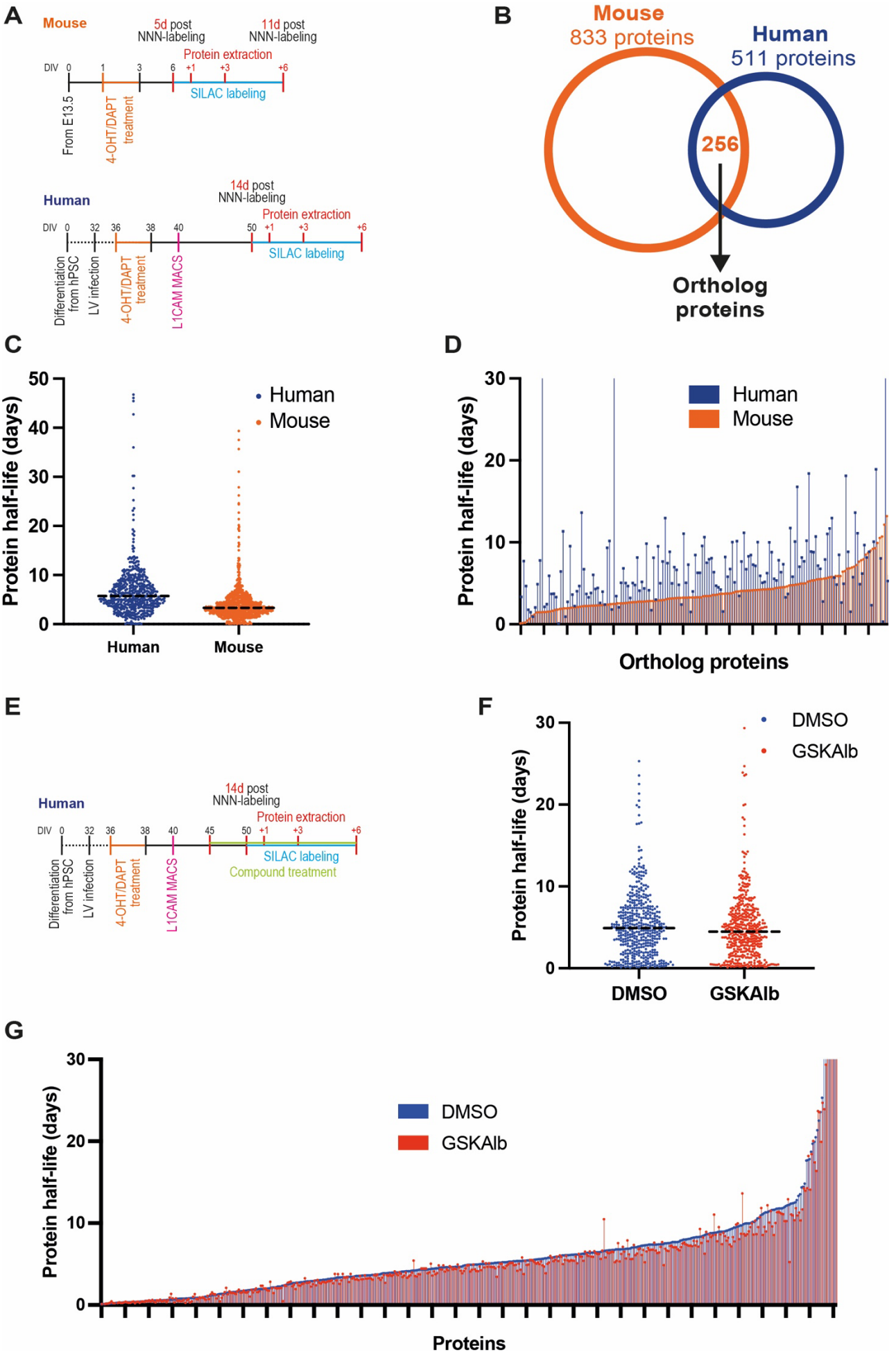

A
Mouse
5d post NNN-labeling
11d post NNN-labeling
Protein extraction
DIV 0 1 3 6 +1 +3 +6
SILAC labeling
From E13.5
4-OHT/DAPT treatment
Human
14d post NNN-labeling
Protein extraction
DIV 0 32 36 38 40 50 +1 +3 +6
SILAC labeling
Differentiation from hPSC
LV infection
4-OHT/DAPT treatment
L1CAM MACS
B
Mouse
833 proteins
Human
511 proteins
256
Ortholog proteins
C
Protein half-life (days)
Human
Mouse
Human
Mouse
D
Protein half-life (days)
Human
Mouse
Ortholog proteins
E
Human
14d post NNN-labeling
Protein extraction
DIV 0 32 36 38 40 45 50 +1 +3 +6
SILAC labeling
Compound treatment
Differentiation from hPSC
LV infection
4-OHT/DAPT treatment
L1CAM MACS
F
Protein half-life (days)
DMSO
GSKAlb
DMSO
GSKAlb
G
Protein half-life (days)
DMSO
GSKAlb
Proteins

Figure 16. Interspecies differences in protein turnover and impact of mitochondria enhancing treatment on protein turnover in human cortical neurons. (A) Experimental timelines of SILAC experiments to measure protein turnover in Mouse and Human maturing cortical neurons. (B) Schematic of the number of proteins identified in Mouse and Human cortical neurons. (C) Distribution of protein half-lives for all proteins identified in Mouse and in Human. Mouse: N=2 ; Human: N=2 . (D) Half-life of ortholog proteins between Mouse and Human ranked in ascending half-life order for Mouse. (E) (F) Distribution of protein half-lives for all proteins identified in Human DMSO and AlbuMAX/GSK treated conditions. DMSO: N=3; AlbuMAX/GSK: N=3. (G) Half-life of proteins in Human DMSO and AlbuMAX/GSK treated conditions ranked in ascending half-life order for DMSO condition. DMSO: N=3; AlbuMAX/GSK: N=3.

Discussion

Altogether our data indicate that the rate of mitochondrial activity can directly influence the developmental tempo of cortical neurons. They show that species-specific differences in mitochondrial activity and quantity are one of the mechanisms responsible for species-specific rates of cortical neuron maturation, and in particular the delayed neotenic maturation of human cortical neurons.

Importantly, while GSK/AlbuMAX treatment enhances mitochondrial activity, the oxygen consumption rate (OCR) in human treated neurons is still lower than in mouse neurons of similar age (Fig.6C-E, Fig.10B). In addition, treating the cells with higher doses of GSK did not lead to further significant increase in OCR nor further significant acceleration of cortical neuron maturation (Fig.13B,D,E), suggesting that a plateau was reached in terms of LDHA activity. This indicates that other mechanisms than increased LDHA activity, and probably also than increased utilization of fatty acids, contribute to increased mitochondrial activity in mouse neurons. Likewise, the treated neurons display accelerated induction of global maturation properties, including molecular markers, morphology, neuronal excitability and connectivity weeks ahead of time. However, it should be emphasized that they are still less mature than mouse counterparts at the same age, and less mature than xenotransplanted neurons several months post-transplantation for instance.

In addition, the fact that the maturation timeline of human cortical neurons is further delayed than in other organs and cell types(*105*, *106*, *127–129*), including other neuronal subtypes like motor neurons(*105*), also suggests that other mechanisms than differences in mitochondrial activity contribute to the species-specific differences in developmental timing of cortical neuron maturation. Such mechanisms could reside in divergences within the GRN of cortical neuron maturation, for example, by the expression of human-specific genes that may have acquired new functions. It could also include species-specific patterns of

expression of conserved genes through quantitative changes or timing differences in their transcription. Other mechanisms could also lie in divergences in processes that do not participate directly in the GRN but influence the way it proceeds over time. Such processes could include differences in RNA stability and in protein turnover, as well as differences in intermediary metabolism driving epigenetic remodeling of the chromatin landscape. Several of these mechanisms could operate separately or be interacting to some extent with mitochondrial function.

Indeed, as for downstream mechanisms, differences in mitochondrial metabolic rates could alter the species-specific turnover rate of RNAs and proteins(*102*, *130*). Our data suggest that enhancing mitochondrial function could increase protein turnover. However, the observed differences in protein half-lives after GSK/AlbuMAX treatment are small. This is not unexpected as mitochondrial OCR in human treated neurons remains lower than in mouse neurons of similar age. But it would be interesting to test if enhancing further mitochondrial function would result in a larger shift of protein half-lives and show a dose-response relationship between mitochondrial function and protein turnover. Our results suggest that mitochondrial enhancement increases protein turnover across the whole proteome, concerning short-lived as well as long-lived proteins. But whether it specifically impacts transcription factors belonging to cortical neuron maturation GRN needs to be tested.

Mitochondrial metabolic rate could interact with protein turnover at different levels. RNA and protein synthesis have been described as being among cell processes the most dependent upon ATP supply(*131*). More specifically, mitochondria have been shown to be fueling local protein synthesis in the post-synaptic dendritic compartment during plasticity(*99*). Protein degradation is also an ATP consuming process(*132*). In eukaryotic cells, the predominant protein degradation pathways are the ubiquitin proteasome system (UPS) and macroautophagy. Under basal condition, the UPS is thought to be the primary degradation

pathway for both the rapid degradation of misfolded and regulatory proteins and most of the slower breakdown of the bulk of cellular proteins(*133*, *134*). Macroautophagy is also involved in the constitutive turnover of long lived proteins(*133*, *135*). In addition, post-translational modifications of UPS components can modulate their activity both at the level of substrate ubiquitination rate and of proteasome catalytic activity itself(*136*, *137*). Macroautophagy has also been shown to be up-regulated in non-dividing quiescent cells(*133*). RNA and protein turnover rates were recently associated with differential developmental timing in other systems(*105*, *106*).

Besides ATP production, it has been shown that one major function of mitochondrial respiration in proliferating cells was to provide electron acceptors to support de novo aspartate biosynthesis, which itself is a key anabolic element for purine and pyrimidine as well as protein synthesis(*138*). Cortical neurons are non-proliferating cells but are requiring a high anabolism for their maturation. Species-specific differences in mitochondrial respiration could similarly be limiting aspartate synthesis and the related anabolic rate in cortical neurons and thereby regulate their tempo of maturation.

In other contexts, in particular in stem cell differentiation and oncogenesis, the metabolic state of the cell has been shown to have a major impact on the way signaling pathways are translated into the nucleo-cytosolic space(*139*, *140*). Variations in levels of glucose uptake, glycolytic flux, lactate production and TCA cycle flux result in different concentrations of glycolysis and TCA metabolites as well as physico-chemical parameters such as pH, redox balance represented by the NAD+/NADH ratio, and generation of reactive oxygen species (ROS). Several of these metabolites serve as substrates or regulators of post-translational protein modifications (PTM), such as protein methylation/demethylation, acetylation/deacetylation, o-glycosylation, as well as DNA methylation. pH and NAD+/NADH can also influence the rate of PTMs. In turn, PTMs can affect the gene expression program by changes in the epigenetic regulation of chromatin state, direct activation/repression of

gene transcription, and modulation of cell signaling outputs. Mitochondrial dynamics changes and metabolic shifts, including between aerobic glycolysis and oxidative phosphorylation, have been documented to take place with cell fate transitions in different cell types, including cardiomyocyte differentiation(*141*), T lymphocyte differentiation(*142*), follicle cell differentiation(*143*), naïve-to-primed interconversion of embryonic stem cells(*144*). Similarly metabolic reprogramming(*145*) and changes in mitochondrial dynamics and chromatin remodeling through Sirt1-dependent histone deacetylation have been involved in neurogenesis, by negatively regulating promotor self-renewal and promoting neural fate acquisition and differentiation(*111*, *146*, *147*). The precise role of these changes and whether they are permissive or instructive remains to be determined(*139*, *140*) but similar mechanisms could be involved at a different timescale during cortical neuron maturation.

Furthermore, recent data have pointed to epigenetic mechanisms as rate-limiting during neural differentiation(*148*) and maturation(*149*). Indeed, a recent study documented that a subset of chromatin regulators were progressively downregulated during cortical neuron maturation. Interestingly, loss-of-function of several of these genes in newborn neurons was associated with their precocious morphological and electrophysiological maturation. More surprisingly, transient inhibition of some of these chromatin regulators, including histone lysine methyltransferases and demethylases, at the stage of the neural progenitor cell (NPC), before cell division and the induction of neurogenesis, resulted also in precocious neuronal maturation, suggesting that there is an “epigenetic barrier” already defined at the NPC stage that prevents faster progression of the maturation transcriptional program(*149*). The dynamic of histone PTM was also shown to regulate transcriptional programs of cerebellar granule cell migration and maturation(*150*, *151*). This could be related to our findings as changes in mitochondrial metabolism could result in changes in substrate availability for PTMs and in the kinetics at which they take place.

As for upstream mechanisms, our transcriptomic analyses indicate that at least part of the temporal differences in mitochondria maturation likely originate from patterns of mitochondria gene regulatory mechanisms(see Iwata, Casimir et al, Science 2023, ref(*112*)), but the observed species differences in mitochondria function likely also involve post-translational mechanisms such as modifications of mitochondrial dynamics and assembly of the ETC(*113*, *152*, *153*).

Interestingly, our data identify at the cellular level in cortical neurons differences in species-specific metabolic properties that are in line with previous reports of years-long periods of aerobic glycolysis observed at the organ level in the developing human cortex(*24*, *25*, *154*). It suggests they could be one of the mechanisms underlying the human brain neoteny.

Our data point to a crucial role of mitochondria during cortical neuron maturation but whether mitochondria play a similar role in the maturation of other neuronal subtypes remains to be determined. In particular, isolation of intact and functional mitochondria from different cell types in the mouse cerebellum and their proteomic characterization have shown a diversity of mitochondria displaying cell-type specific profiles(*155*). Further studies are required to characterize when this molecular diversity of cell-type specific mitochondria unfolds during development and if it results in differential regulation of cell maturation.

Mitochondria and metabolism could contribute to heterochrony in other developmental contexts than neuron maturation. Indeed metabolic rates influence the final maturation of cardiac and pancreas cells(*86*–*88*). A recent report identifies the metabolic rate as a regulatory mechanism of the timing of the somitic segmentation clock, with species-specific differences in metabolic rates underlying different species-specific segmentation clock speeds(*127*). More specifically, it points to the redox balance as assessed by the NAD+/NADH balance as a key limiting factor of the developmental clock speed, potentially and partly through the regulation of the protein translation rate rather than the protein degradation rate(*127*). Interestingly, this represents a very different developmental context

in which the metabolic rate is linked to the developmental rate as the somite segmentation consists of dividing cells while cortical neurons are post-mitotic non-dividing cells where cellular growth refers to an increase in cell size, complexity and compartmentalization, as well as functional maturation, rather than to cell division and population growth. The more precise role of the NAD+/NADH balance remains to be investigated, especially in the context of cortical neuron maturation, which has so far been limited by the technical hurdle of obtaining precise measurements of the ratio in the different cellular subcompartments, in particular in the cytosolic, nuclear and mitochondrial subcompartments, making the interpretation of changes in the global NAD+/NADH ratio delicate. On the other hand, the different cellular context could also imply different downstream mechanisms and the role of the NAD+/NADH balance could be different in somite segmentation and in cortical neuron maturation.

Our data focused on developmental timing but mitochondria and metabolism could also have a broader impact, extending beyond the context of development, and regulating neuronal plasticity and aging, through changes in epigenetics and/or proteostasis(*67*, *156*). Basal metabolic rate is also correlated to lifespan(*68*). Aging is generally associated with mitochondrial dysfunction(*157*). In addition, mitochondria have also been shown to be involved in adult hippocampal neurogenesis and neuron maturation with perturbation of mitochondrial function likely underlying neurogenesis-defects in the aging hippocampus(*94*).

Accelerated human neuronal maturation *in vitro* might benefit PSC-based modelling of human neurological diseases, which remains greatly hindered by the slowness of human neuron development.

On the other hand, prolonged human neuronal development has been long proposed to have a key role in acquiring human-specific cognitive features(*158*). Tools to accelerate or decelerate cortical neuron maturation could allow experimental exploration of the consequences of neuronal neoteny on the development, function, and plasticity of brain

circuits. They could also have important implications for human stem cell therapies and in particular, stem cell derived neuron replacement therapies(*159*).

Defects of mitochondrial function underly mitochondrial diseases which are a very heterogeneous group of diseases causing a wide range of clinical presentations, likely to affect almost any organ and tissue(*160*, *161*).

Neurological symptoms in some mitochondrial diseases could be linked to defects of neuronal maturation. Conversely, it will be interesting to assess mitochondrial function in neuro-developmental diseases where mitochondria are not identified as the primary cause of the disease. For example, altered mitochondrial morphology and metabolism as well as altered protein synthesis and degradation rates have been linked to perturbation of dendritic spine maturation and plasticity in Fragile X syndrome(*100*, *162*).

Also, many mitochondrial diseases do not alter cortical neuron maturation and dissecting into details the nature and timing of mitochondrial function defects in these diseases and the mechanisms by which they spare cortical neuron maturation should bring new insights into their precise regulatory functions.

In our project, we applied chemical compound treatments and genetic strategies to fine tune mitochondrial function at the long term without significant toxicity. These approaches are encouraging for the development of future therapies in the field of mitochondrial diseases.

Finally, in terms of the limitations of the current study and future perspectives, we compared mitochondrial function during cortical maturation of only two species: mouse and human. It would be interesting to include more species with different maturation and basal metabolic rates. A recent study comparing presomitic mesoderm cells from six mammalian species failed to show correlations between mitochondrial activity and somitic clock developmental timing(*163*).

The acceleration of maturation after mitochondrial enhancement was assessed by morphological and electrophysiological criteria. It would be interesting to perform a single cell RNA analysis to see if the transcriptomics profile of treated neurons corresponds to more mature stages.

Our mitochondrial morphological analysis is restricted to mitochondria from the soma and proximal dendrites. It does not document the evolution of mitochondria in more distal dendrites nor in the axons. On the other hand, OCR measurement is based on cell suspensions. Therefore it should represents whole cell mitochondria. However, especially for mature stages with complex dendritic arborization, we cannot exclude that more distal dendrites as well as the axons were lost during cell preparation. The metabolomics and proteomics are based on whole cells in culture.

As neurons are compartmentalized cells, mitochondria from different compartments could behave differently. Interestingly, in mouse neurons treated with pyruvate carrier inhibitor and rotenone, the complexity of the dendritic arborization was reduced but the axons seemed less affected by the treatment (data not shown) even if this was not quantified. This analysis would be very interesting and could point to different functions of mitochondria in different cell compartments during maturation.

Our data compare the OCR per cell and therefore does not give insight on whether observed differences are due to differences in quantity of mitochondria per cell, or difference in mitochondrial efficiency itself, or both. Additional experiments could be performed by measuring the OCR after normalizing by mitochondrial protein content.

Our proteomics data suggests that mitochondrial enhancement could increase protein turnover. In return, it would be interesting to see if changing protein turnover would affect neuron maturation, as well as mitochondrial oxidative function.

Materials and Methods

Mice

All mouse experiments were performed with the approval of the KU Leuven Committee for animal welfare. Mice were housed under standard conditions (12h light:12h dark cycles) with food and water ad libitum. Embryos (aged E13.5 - E14.5) of the mouse strain ICR (CD1, Charles River Laboratory) or Swiss (Janvier Labs) were used for in utero experiments and primary cultures. The plug date was defined as embryonic day E0.5, and the day of birth was defined as P0. The data obtained from all embryos were pooled without discrimination of sexes for the analysis of in utero electroporation, given the difficulty to determine sex identity at embryonic stages. RAG2 knock-out mice were used for xenotransplantation experiments.

DNA Constructs

The DNA fragment of NeuroD1 promoter was amplified from pNeuroD-ires-GFP, a gift from Franck Polleux (Addgene plasmid #61403; http://n2t.net/addgene:61403 ; RRID:Addgene_61403) using the following primers pair: 5'-TTAATTAAGAGCTCGGAGG ACACTTGCTGGG-3'/5'-ACCGGTGAATTCCTCGTGTCCCGGTGGC-3'. The DNA fragment of CreERT2 was amplified from the Nestin-CreERT2 mouse genome using the following primers pair: 5'-GCTAGCATGTCCAATTTACTGACCGTAC-3'/5'-GGCGCGCCT CAAGCTGTGGCAGGGAAACCC-3'. These DNA fragments were transferred to a lentiviral backbone (a gift from Cecile Charrier) by restriction enzyme digestion and ligation to obtain pLenti-NeuroD1 promoter-CreERT2-WPRE.

The DNA fragment of T2A-tCD8 (truncated CD8a) was amplified from CD8a-EGFP, a gift from Lei Lu (Addgene plasmid # 86051 ; http://n2t.net/addgene:86051 ; RRID:Addgene_86051) using the following primers pair; 5'-

tTGTACAAGGGATCCGGAGAGGGGAGAGGATCACTGCTGACTTGCGGGGATGTGGA AGAGAACCCAGGGCCCATGGCCTTACCAGTGACC-3'/5'-aAGCGCTTCAGTGGT TGCAGTAAAGGGTGATAACCAGTGACAGGAGAAGG-3'. T2A-tCD8 fragment was transferred to the lentiviral backbone pLenti-CAG-DIO-EGFP-WPRE by restriction enzyme digestion and ligation to obtain pLenti-CAG-DIO-EGFP-T2A-tCD8-WPRE.

The DNA fragment of codon optimized tCD8 was amplified from pSLHDR02_EGFP_tCD8, a gift from Matthew Porteus (Addgene plasmid # 124061 ; http://n2t.net/addgene:124061 ; RRID:Addgene_124061) using the following primers pair: 5'-TATCGCCTTgctagccaccATGGCTCTGCCTGTGACAG-3'/5'-GCTTAATGggcgcgccTCA ATGGTTGCAATACAGTGTG-3'. tCD8 fragment was transferred to lentiviral backbone pLenti-CAG-DIO-EGFP-WPRE(*111*) by restriction enzyme digestion and ligation to obtain pLenti-CAG-DIO-EGFP-tCD8-WPRE.

The DNA fragment of tTA was amplified from pK029.CAG-loxP-stop-loxP-RFP-ires-tTA-WPRE, a gift from Takuji Iwasato (Addgene plasmid # 69138 ; http://n2t.net/addgene:69138 ; RRID:Addgene_69138) using the following primers pair: 5'-tGCTAGCATGTCTAGACTGGACAAGAGCAAAG-3'/5'-aGGCGCGCCTTACCCGGGGAGCATGTCAAGGTCAAAA-3'. The tTA fragment was transferred to the lentiviral backbone pLenti-hSynI-EmGFP-WPRE by restriction enzyme digestion and ligation to obtain pLenti-hSynI-tTA-WPRE.

The DNA fragment of EmGFP was amplified from pLenti-hSynI-EmGFP-WPRE using the following primers pair: 5'-GCTAGCgccaccATGGTGAGCAAGGGCGAGGAG-3'/5'-GGCGCGCCTTACTTGTACAGCTCGTCCATG-3'. EmGFP fragment was transferred to lentiviral backbone pLenti-TRE-LSL-mito-EmGFP-WPRE(*111*) by restriction enzyme digestion and ligation to obtain pLenti-TRE-EGFP-WPRE.

Lentiviral preparation

HEK293T cells were transfected with the packaging plasmids, psPAX2, a gift from Didier Trono (Addgene plasmid # 12260; http://n2t.net/addgene:12260; RRID:Addgene_12260) and pMD2.G, a gift from Didier Trono (Addgene plasmid # 12259; http://n2t.net/addgene:12259; RRID:Addgene_12259), and a plasmid of the gene of interest in the lentiviral backbone pLenti-NeuroD1 promoter-CreERT2-WPRE (this study), pLenti-CAG-DIO-EGFP-WPRE, pLenti-UbC promoter-rtTA-WPRE (a gift from Rudolf Jaenisch (Addgene plasmid # 20342 ; http://n2t.net/addgene:20342 ; RRID:Addgene_20342)), pLenti-TRE-LSL-mito-EmGFP-WPRE(*111*), pLenti-CAG-DIO-EGFP-T2A-tCD8-WPRE (this study), pLenti-CAG-DIO-tCD8-WPRE (this study), pLenti-human Synapsin I promoter (hSynI)-EmGFP-WPRE, pLenti-hSynI-tTA-WPRE (this study), pLenti-TRE-EGFP-WPRE (this study), pLenti-TRE-LDHB-IRES-EGFP-WPRE (this study)). Three days after transfection, the culture medium was collected and viral particles were enriched by filtering (Amicon Ultra-15 Centrifuge Filters, Merck, Cat#UFC910008). Titer check was performed on HEK293T cell culture for every batch of lentiviral preparation.

Cell culture media

hES medium (Wisconsin medium)

KnockOut-DMEM (Thermo Fisher Scientific, Cat#10829018) with KnockOut Serum Replacement (20%, Thermo Fisher Scientific, Cat#10828028), Non-Essential Amino Acids Solution (1x, Thermo Fisher Scientific, Cat#11140050), L-Glutamine (2mM, Thermo Fisher Scientific, Cat#25030081), 2-Mercaptoethanol (100μM, Merck, Cat#M3148) and Human FGF-basic (10ng/ml, PeproTech, Cat#AF-100-18B).

DDM/B27 medium

DMEM/F12 + GlutaMAX (Thermo Fisher Scientific, Cat#10565042) with N2-supplement (1x, Thermo Fisher Scientific, Cat#A1370701), B27 supplement minus Vitamin A (1x, Thermo Fisher Scientific, Cat#12587010), Bovine Albumin Fraction V (0.05%, Thermo Fisher Scientific, Cat#15260037), 2-Mercaptoethanol (100µM, Merck, Cat#M3148), Non-Essential Amino Acids Solution (1x, Thermo Fisher Scientific, Cat#11140050) and Sodium Pyruvate (1mM, Thermo Fisher Scientific, Cat#11360070).

Nb/B27 medium

Neurobasal (Thermo Fisher Scientific, Cat#21103049) with B27 supplement minus Vitamin A (1x, Thermo Fisher Scientific, Cat#12587010) and L-Glutamine (2mM, Thermo Fisher Scientific, Cat#25030081).

DDM/B27+Nb/B27 medium

A mixture of Mix DDM/B27 and Nb/B27 medium at 1:1 ratio.

Nb/B27x medium

Neurobasal (Thermo Fisher Scientific, Cat#21103049) with B27 supplement (1x, Thermo Fisher Scientific, Cat#17504044) and GlutaMAX supplement (1x, Thermo Fisher Scientific, Cat# 35050061).

Nb/B27 low glucose medium

Neurobasal-A (Thermo Fisher Scientific, Cat#10888022) with B27 supplement (1x, Thermo Fisher Scientific, Cat#17504044), Sodium Pyruvate (0.227mM, Thermo Fisher Scientific,

Cat#11360070), Glucose (2.5mM, Thermo Fisher Scientific, Cat#A2494001) and GlutaMAX supplement (1x, Thermo Fisher Scientific, Cat# 35050061).

NbA/B27 medium

Neurobasal-A (Thermo Fisher Scientific, Cat#10888022) with B27 supplement (1x, Thermo Fisher Scientific, Cat#17504044), Sodium Pyruvate (0.227mM, Thermo Fisher Scientific, Cat#11360070), Glucose (25mM, Thermo Fisher Scientific, Cat#A2494001) and GlutaMAX supplement (1x, Thermo Fisher Scientific, Cat# 35050061).

Human PSC culture and cortical cell differentiation

Human ESC (hESC) (H9; WiCell Cat # NIHhESC-10-0062; female donor) were grown on irradiated mouse embryonic fibroblasts in the ES cell medium until the start of cortical cell differentiation. Cortical cell differentiation was performed as described previously(*18*). Two days before starting neuronal cell differentiation (day -2), hESCs were dissociated with Accutase (Thermo Fisher Scientific, Cat#00-4555-56) and plate on Matrigel-coated (BD, Cat#354277) plates at low confluency (5,000 cells/cm^2) in hES medium with 10μM ROCK inhibitor (Merck, Cat#688000). On day 0 of the differentiation, the medium was changed to DDM/B27 medium with recombinant mouse Noggin (100ng/ml, R&D systems, Cat#1967-NG). The medium was changed every other day until day 6. From day 6, the medium was changed every day until day 16. At day 16, medium was changed to DDM/B27 medium and changed every day until day 25. At day 25, the differentiated cortical cells were dissociated using Accutase and cryopreserved in mFreSR (STEMCELL technologies, Cat#05855). D ifferentiated cortical cells were validated for neuronal and cortical markers by immunostaining using antibodies for TUBB3 (1:2,000; BioLegend, Cat#MMS-435P), TBR1 (1:1,000; Abcam, Cat#ab183032), CTIP2 (1:1,000; Abcam, Cat#ab18465), FOXG1

(1:1,000; Takara, Cat#M227), SOX2 (1:2,000; Santa Cruz, Cat#sc-17320), FOXP2 (1:500; Abcam, Cat#ab16046), SATB2 (1:2,000; Abcam, Cat#ab34735), and CUX1 (1:1,000; Santa Cruz, Cat#sc-13024).

Mouse PSC culture and cortical cell differentiation

Mouse ESC (mESC) (E14Tg2A; ATCC Cat # CRL) were cultured and differentiated as described previously(*166*) with some modifications. One day before starting differentiation (day -1), mESCs were dissociated with Accutase and plated on Gelatin or GFR-Matrigel (Corning, Cat#354230) coated 5 cm dish. On day 0 of the differentiation, the medium was changed to DDM/B27 medium with recombinant mouse Noggin (100 ng/ml). At day2, the medium was changed to DDM/B27+Noggin with Cyclopamine (1μM, Calbiochem, Cat#239803). The medium was changed every day until day 6. At day 6, medium was changed to DDM/B27 medium with Cyclopamine. At day 10, the medium was changed to DDM/B27 medium. At day 13, the differentiated cortical cells were dissociated using NeuroCult Enzymatic Dissociation Kit for Adult CNS Tissue (STEMCELL technologies, Cat#05715) following the manufacturer's instructions. Dissociated cells were plated on laminin and poly-D-lysin coated culture dish or coverslip. D ifferentiated cortical cells were validated for neuronal and cortical markers by immunostaining using antibodies for TUBB3 (1:2,000; BioLegend, Cat#MMS-435P), TBR1 (1:1,000; Abcam, Cat#ab183032), CTIP2 (1:1,000; Abcam, Cat#ab18465), FOXG1 (1:1,000; Takara, Cat#M227) and SATB2 (1:2,000; Abcam, Cat#ab34735).

Immunostaining

For immunocytochemistry, coverslips were fixed with 4% PFA in PBS 1h at 4°C. The coverslips were transferred into PBS, then blocked using PBS with 3% horse serum (Thermo

Fisher Scientific, Cat# 16050122) and 0.3% Triton X-100 (Sigma-Aldrich, Cat#T9284) during 1h, and incubated overnight at 4°C with the primary antibodies. After three washes with PBS/0.1% Triton X-100, the coverslips were incubated in PBS for 5 min at room temperature and incubated 2h at room temperature with the appropriate secondary antibodies with DAPI (Merck, Cat#D9542) or Hoechst (Thermo Fisher Scientific, Cat#3570). The coverslips were again washed three times with PBS for 5 min. The coverslips were mounted on a Superfrost slide (Thermo Fisher Scientific) using Glycergel mounting medium (Dako, Cat#C0563). The cells were immunostained using the following antibodies for Mitochondria (1:800; Abcam, Cat#ab92824), GFP (1:2,000; Abcam, Cat#ab13970), mCherry (1:1,000; Thermo Fisher Scientific, Cat#M11217), TUBB3 (1:2,000; BioLegend, Cat#MMS-435P), TUBB3 (1:2,000; BioLegend, Cat#PRB-435P), MAP2 (1:1,000; Merck, Cat#M1406), Sox2 (1:2,000; Santa Cruz, Cat#sc-17320), Active Caspase-3 (1:1,000; R&D systems, Cat#AF835), Synapsin-1 (1:200-1,000; Cell Signaling Technology, Cat#5297), Human Nuclei (1:1,000; Merck, Cat#MAB1281) and NPAS4 (1:1,600; Thermo Fisher Scientific, Cat#PA5-58713). Imaging was performed using either a Zeiss LSM880 confocal microscope or a Nikon Märzhäuser Slide Express 2 (Nikon) controlled by the Zen Black software (Zeiss) or NIS-Element (Nikon).

NNN-labeling

For NNN-labeling (Fig. 2), human cortical cells (frozen at day 25) were thawed and plated on Matrigel-coated plates using DDM/B27+Nb/B27 medium with Cre reporter lentivirus (LV-CAG-DIO-EGFP-WPRE) at 37˚C with 5% CO_2. Three days after thawing (day 28), the cells were dissociated using Accutase and plated on mouse astrocyte-coated coverslips at low confluency (50,000 cells/cm2). LV-NeuroD1 promoter-CreERT2-WPRE was infected at day 30. Two days after CreERT2 lentivirus infection (day 32), medium was changed to DDM/B27+Nb/B27 medium with 0.25μM 4-Hydroxytamoxifen (4-OHT) (Merck,

Cat#SML1666). The next day (day 33), medium was changed to fresh DDM/B27+Nb/B27 medium. The culture medium was changed twice a week.

At indicated time points (Fig. 2B), coverslips were fixed with 4% PFA and immunostained with anti-GFP and anti-MAP2 antibodies.

Mouse mitochondria labeling

For mouse NNN-labeled cell mitochondria labeling (Fig. 3A), timed pregnant CD1 mice were in utero electroporated (IUE) at E14.5 with the following construct: pLenti-NeuroD1 promoter-CreERT2-WPRE (500ng/µl), pCAG-LSL-tdTomato-WPRE (1µg/µl), pUbC promoter-M2rtTA (500ng/µl), a gift from Rudolf Jaenisch (Addgene plasmid # 20342 ; http://n2t.net/addgene:20342 ; RRID:Addgene_20342), and pTRE-LSL-Cox8-EmGFP-WPRE (500g/µl). IUE was performed as described previously(*111*). On the same day, electroporated embryos were used for primary mouse cortical cell culture as described in the previous section. 4-OHT (0.25µM) was added to the medium from day *in vitro* (DIV) 0 to DIV2. Half of the medium was changed every 2-3 days. Doxycycline hyclate (1µg/ml, Sigma-Aldrich, Cat#D9891) was added to the medium 24h before fixation. At indicated time points, cells were fixed in 4% PFA in PBS for 1h, at 4°C. The coverslips were washed in PBS, incubated in PBS with 0.3% Triton X-100 with DAPI for 30 min at room temperature, then washed in PBS and mounted on a Superfrost slide with Glycergel mounting medium.

PSC-derived Mouse mitochondria labeling

For PSC-derived mouse NNN-labeled cell mitochondria labeling, PSC-derived cortical cells were dissociated with NeuroCult Enzymatic Dissociation Kit at day 13 of the differentiation. Dissociated cells were plated on laminin and poly-D-lysin coated coverslip with the following lentivirus: LV-NeuroD1 promoter-CreERT2, LV-UbC promoter-rtTA-WPRE, LV-TRE-LSL-

mito-EmGFP-WPRE. At day 14, DAPT (10μM) and 4-OHT (0.25μM) were added to the Nb/B27 medium for 48h. Doxycycline hyclate was added to the medium 24h before fixation. At indicated time points, cells were fixed in 4% PFA in PBS for 1h, at 4°C. The coverslips were washed in PBS and further processed for immunostaining using anti-MAP2 and anti-Tbr1 antibodies, as described in previous section.

Human mitochondria labeling

For human NNN-labeled cell mitochondria labeling (Fig. 3B). Human cortical cells (frozen at day 25) were thawed and plated on Matrigel-coated plates using DDM/B27+Nb/B27 medium at 37˚C with 5% CO_2. At day 32, the cortical cells were dissociated with Accutase and plated on Matrigel coated 6-well plates at 260,000-300,000 cells/cm^2. One fourth of the cells were infected with the following lentiviral vectors: LV-NeuroD1 promoter-CreERT2-WPRE and LV-CAG-DIO-EGFP-WPRE. At day 34, 4-OHT (0.25μM) was added to the medium for 48h. At day 35, AraC (Cytosine β-D-arabinofuranoside hydrochloride, Sigma-Aldrich, Cat#C6645-25MG) was added to the medium for 24h. At day 37, the cells were dissociated using Accutase and plated on mouse-astrocyte coated coverslips at 100,000 cells/cm^2 with a ratio of non-infected to infected cells of 4:1. At indicated time points, the cells were fixed in 4% PFA in PBS for 1h at 4°C and further processed for immunostaining using anti-GFP and anti-Mitochondria antibodies, as described in previous section.

Mitochondrial morphology analysis

Morphologies were imaged on a Zeiss LSM880 confocal microscope, using the Airyscan function with a 63x (NA 1.4) oil immersion objectives with 1.8x digital zoom, at a horizontal resolution of 0.0732 μm/pixel and a vertical resolution of 0.18-0.21 μm/pixel. For each cell, a z-stack of 10-30 images was acquired centered on the cell of interest. For mitochondrial

length measurement, a maximal intensity projection image of the mitochondrial channel was performed. An image of the first cell was thresholded visually as to optimally individualize mitochondria fragments using raw mitochondrial membrane signal (Mouse: mito-EmGFP, Human: mitochondrial antibody). This image was later used as a “reference” image for visual thresholding of the other cell images. The freehand tool in Fiji was used to manually trace the maximum length of mitochondria fragment. The 3D projection tool or serial images were used to determine whether there is a connection between mitochondria fragments. Only mitochondria fragments which could be visually identified as single mitochondria were measured.

For mitochondrial volume, a z-stack of images of the mitochondrial channel of the first cell was thresholded visually as to optimally individualize mitochondrial fragments using raw mitochondrial membrane signal. This stack was later used as a “reference” for visual thresholding of the other cell stacks. To remove mitochondria belonging to neighboring cells around the cell of interest, a maximal intensity projection image of the channel corresponding to the cell cytoplasm was performed. Using the polygon selection tool in Fiji, a selection corresponding to the cell envelope was manually traced. This selection was applied across the stack of the mitochondrial channel and the function “clear outside” of Fiji was used to remove mitochondria outside of the selection. Then the stack of image was converted to 8-bit and binarized and the 3D ImageJ suite of Fiji was used for measuring the volume in 3D.

CLEM (correlative light and electron microscopy)

For mouse cells (Fig. 4A and 5), timed pregnant CD1 mice were in utero electroporated (IUE) at E14.5 with the following construct: pCAG-EGFP-WPRE (1µg/µl). At indicated time points (E16.5, P0, P7, P14 and P30), mice were perfused with 4% PFA (Electron Microscopy Services, Cat#15714) and 0.5% glutaraldehyde (GA, Electron Microscopy Services,

Cat#16220) in 0.1M phosphate buffer (PB) and the brains were collected. After post-fixation overnight at 4°C, 100µm vibratome sections were made. GFP positive neurons were marked by near-infrared branding (NIRB) as described previously(*167*, *168*). The bleaching function of the ZEN2010 software (Zeiss) was used to perform NIRB around the cell of interest on a LSM 780 inverted confocal microscope. Branding marks were introduced to the tissue with a Mai Tai DeepSee two-photon laser (Spectra-Physics) at 800 nm and 40% maximal power output. Z-stacks of the region of interest were acquired before and after NIRB. Sections were then post-fixed in 4% PFA with 2.5% GA and 0.2% picric acid (Electron Microscopy Services, Cat#19554) in 0.1M PB and kept in this solution at 4°C till further processing. Next, sections were rinsed and cropped to 1mm^2 pieces around the neuron of interest. Samples were stained with 1% osmium tetroxide and 1.5% potassium ferrocyanide (Merck, Cat#455989) in milliQ H_2O (MQ) for 1h, followed by 30 min of 0.2% tannic acid (Electron Microscopy Services, Cat#21700) in MQ, 0.5% osmium tetroxide (Electron Microscopy Services, Cat#19152) in MQ, 1% thiocarbohydrazide (Merck, Cat#88535) in MQ and 0.5% osmium tetroxide in MQ. Samples were then stained with 0.5% uranyl acetate (Electron Microscopy Services, Cat#22400) in 25% methanol at 4°C overnight. The next day the samples were stained en bloc with lead aspartate for 30 min at 60°C, followed by dehydration in increasing ethanol concentrations (30%, 50%, 70%, 90% and 2x 100%) at 4°C, 10 min each. After further dehydration with propylene oxide (2 times, 10 min), sections were infiltrated with epon/propylene oxide mixture and flat embedded in pure epon. Embedded pieces were mounted on aluminum pin stubs (Gatan) with conductive epoxy (Circuit Works). Approaching and imaging of the region of interest was done with a Zeiss Sigma Variable pressure SBF-SEM with 3View technology (Gatan). Neurons of interest could be located based on the branding marks and on the surrounding blood vessels. A stack of the neuron was imaged at 1.3 kV with 15nm pixel size and 100nm sections. Next, to have the 3D model, segmentation of individual mitochondria was performed manually

using Microscopy Image Browser (MIB) and reconstruction was done with Amira (thermo Fisher Scientific).

For some samples, when the middle of the neuron of interest was reached by SBF-SEM, 70 nm thick, serial ultrathin sections were cut manually using a Reichardt Ultracut E ultramicrotome. All sections were collected as ribbons of 4–5 sections on triple slot grids (Ted Pella). Images were taken on a JEOL JEM-1400 Transmission Electron Microscope operated at 80 kV at 15k magnification for high resolution images of the mitochondrial cristae.

Xenotransplantation

For the CLEM experiment, human neuron xenotransplantation in neonatal brain was performed as described previously with some modifications. Human cortical cells (frozen at day 25) were thawed and plated on Matrigel-coated plates using DDM/B27+Nb/B27 medium at 37˚C with 5% CO_2. At seven days after thawing (day 32), cells were dissociated using Accutase and plated on Matrigel-coated plate at high confluency (450,000-700,000 cells/cm^2) with LV-hSynI-EmGFP-WPRE. Eight days later (day 40), the medium was changed to DDM/B27+Nb/B27 medium with 10μM DAPT and cultured for three additional days. At day 43, the cells were treated with 5mM AraC for 24h. On the following day, the cortical cells were dissociated using NeuroCult Enzymatic Dissociation Kit following manufacturer's instructions and suspended in the injection solution containing 20mM EGTA (Merck, Cat#03777) and 0.1% Fast Green (Merck, Cat#210-M) in PBS at 100,000–200,000 cells/μl. Approximately 1-2μl of cell suspension was injected into the lateral ventricles of each hemisphere of neonatal (postnatal day 0 or 1) immunodeficient mice (*Rag2*$^{-/-}$) using glass capillaries pulled on a horizontal puller (Sutter P-97). At indicated time points (5 weeks, 6 months and 15 months post xenotransplantation, the mice were perfused with 4% PFA

and 0.5% GA in 0.1M PM and the brains were collected., the sections were used as described in the previous section.

Oxygraphy

Mouse cortical cells were obtained from primary culture mouse embryonic cortex at E13.5-E14.5 as described in the previous section and were plated on 6-well plates that had previously been coated with laminin- and poly-D-lysin overnight at 37°C and horse serum 1h at 37°C, or on coverslips, at $2x10^5$ cells/cm^2 using NbB27x medium with Penicillin-Streptomycin (50U/ml). Plated cells were incubated at 37℃ with 5% CO2. DAPT (10µM,) was added to the medium from DIV1 to DIV3. Human cortical cells (frozen at day 25) were thawed and plated on Matrigel-coated plates using DDM/B27+Nb/B27 medium at 37˚C with 5% CO_2. Seven days after thawing (day 32), the cells were dissociated using Accutase and plated on Matrigel-coated plate at high confluency (450,000-700,000 cells/cm2) with LV-NeuroD1 promoter-CreERT2-WPRE and LV-CAG-DIO-tCD8-WPRE. Four days later (day 36), the medium was changed to DDM/B27+Nb/B27 medium with 4-OHT (1µM) and DAPT (10µM). Two days after 4-OHT/DAPT induction (day 38), the medium was changed to fresh DDM/B27+Nb/B27 medium. At day 40, cortical cells were dissociated using NeuroCult Enzymatic Dissociation Kit following manufacturer's instructions. For CD8+ MACS, dissociated cells were incubated with magnetic beads conjugated anti-human CD8 in MACS buffer at 4˚C for 10 min. CD8 positive selection were carried out with LS columns according to the manufacturer's instructions. The sorted cells were plated on Poly-L-ornithine-(Merck, Cat#P3655), Laminin-(Merck, Cat#L2020) and horse serum-coated plates at 200,000 cells/cm^2 using DDM/B27+NbB27 medium. The DDM/B27+Nb/B27 medium was changed twice a week. For chemical compound treatment experiment (Fig. 10B, Fig. 12, Fig. 13), at day 45, the DDM/B27+Nb/B27 medium was changed to the following medium: (1: DMSO) Nb/B27 low glucose medium with DMSO (1:4,000); (2: GSK) Nb/B27 low glucose medium

with GSK-2837808A (5μM, MedChemExpress, Cat#HY-100681); (3: AlbuMAX+GSK) Nb/B27 low glucose medium with GSK-2837808A (5μM) and AlbuMAX (0.5%, Thermo Fisher Scientific, Cat#11020021). These media were changed every other day. At indicated time points, oxygraphy was performed as described(*116*). Cells were dissociated using NeuroCult Enzymatic Dissociation Kit. First, the cells were washed with Collection solution and incubated in Dissociation solution at 37˚C for 7 min. Next, the Inhibition solution was added to the plate and the cells transferred to a 10ml tube (SARSTEDT, Cat#62.9924.284). After adding PBS up to 10ml and centrifuging at 270xg for 3 min, the cell pellet was resuspended in 200μl of Miro5 buffer before counting. Depending on the species and cell birthdate, Miro5 buffer were added to adjust to 2,000,000-40,000,000 cells/ml. One hundred microliter of this cell suspension was injected per chamber of the oxygraphy O2K with subsequent injections of the following compounds to the final concentration of : catalase (Merck, Cat#C9322), 556U/ml; digitonin (Merck, Cat#300410); 10μg/ml; pyruvate (Merch P2256), 5mM; Malate (Merck, Cat#02288), 0.5mM; ADP (Calbiochem, Cat#117105), 1mM; Glutamate (Merck, Cat#G1251) 10mM; succinate (Merck, Cat#S2378), 10mM; CCCP (Merck, Cat#C2759) Δ1μM until maximum respiration reached; rotenone (Merck, Cat#R8875), 75nM; glycerophosphate (Merck, Cat#G7886), 10mM; antimycin A (Merck, Cat#A8674), 250nM; sodium ascorbate (Merck, Cat#A7631), 2mM; N,N,N′,N′-Tetramethyl-p-phenylenediamine dihydrochloride (TMPD) (Merck, Cat#T3134) 0.5mM; Cytochrome C (Merck, Cat#C7752), 10μM; sodium azide (Merck, Cat#S2002), 200mM. Oxygen saturation was maintained ≥ 40μM throughout the experiment, and between 170 and 200μM before the measurement of isolated complex IV (CIV) activity. The reported values of maximum OXPHOS (phosphorylating) and ETC (non-phosphorylating) were calculated as succinate minus antimycin A (non-mitochondrial respiration) and CCCP minus antimycin A respectively.

Metabolic labeling

Mouse cells were obtained from primary culture of timed pregnant mouse embryos at E13.5-E14.5 as described in the previous section and were plated on 6-well plates that had previously been coated with laminin- and poly-D-lysin overnight at 37°C and horse serum 1h at 37°C, or on coverslips, at 200,000 cells/cm^2 using NbB27x medium with Penicillin-Streptomycin (50U/ml). Plated cells were incubated at 37℃ with 5% CO_2. DAPT (10μM) was added to the medium from DIV1 to DIV3. 5-Fluoro-2′-deoxyuridine (5-FdU, 6.6μg/ml, Merck, F0503) and Uridine (16.5μg/ml, Merck, U3003) were added to the medium from DIV3 to DIV5. On DIV5, cells were dissociated using NeuroCult Enzymatic Dissociation Kit following manufacturer's instructions and plated on 6-well plates coated with laminin- and poly-D-lysin overnight at 37°C and horse serum 1h at 37°C, at 100,000 cells/cm^2 using NbB27x medium. Plated cells were incubated at 37℃ with 5% CO_2. After 2 days, on DIV7, 5-FdU (6.6μg/ml) and Uridine (16.5μg/ml) were added to the medium from DIV7 to DIV10. On DIV10, the medium was changed to NbA/B27 medium**.** One day before U-^{13}C D-glucose tracing experiment, the medium was changed for NbB27 low glucose medium. After one day, on DIV13, the medium was switched to Neurobasal-A with B27 supplement (1x), Sodium Pyruvate (0.227mM), GlutaMAX supplement (1x) and U-^{13}C D-glucose (2.5mM, Cambridge Isotope Laboratories Inc., Cat#CLM-1396).

Human cortical cells (frozen at day 25) were thawed and plated on Matrigel-coated plates using DDM/B27+Nb/B27 medium at 37˚C with 5% CO_2. Seven days after thawing (day 32), the cells were dissociated using Accutase and plated on Matrigel-coated plate at high confluency (450,000-700,000 cells/cm^2) with LV-NeuroD1 promoter-CreERT2-WPRE and LV-CAG-DIO-tCD8-WPRE. Four days later (day 36), the medium was changed to DDM/B27+Nb/B27 medium with 1μM 4-OHT and 10μM DAPT. Two days after 4-OHT/DAPT induction (day 38), the medium was changed to fresh DDM/B27+Nb/B27 medium. At day 40, cortical cells were dissociated using NeuroCult Enzymatic Dissociation Kit following

manufacturer's instructions. For CD8+ MACS, dissociated cells were incubated with magnetic beads conjugated anti-human CD8 in MACS buffer at 4˚C for 10 min. CD8 positive selection was carried out with LS columns according to the manufacturer's instructions. The sorted cells were plated on Poly-L-ornithine-, Laminin-(Merck, Cat#L2020) and horse serum-coated plates at 200,000 cells/cm^2 using DDM/B27+NbB27 medium. The culture medium was changed two times a week. One day before U-^{13}C D-glucose tracing experiment, the medium was changed for NbB27 low glucose medium. After one day, the medium was switched to Neurobasal-A with B27 supplement (1x), Sodium Pyruvate (0.227mM), GlutaMAX supplement (1x) and U-^{13}C D-glucose (2.5mM, Cambridge Isotope Laboratories Inc., Cat#CLM-1396).

After 30 hours of incubation with U-^{13}C D-glucose medium, for each well, 200 µl of medium were snap frozen in liquid nitrogen. Then the rest of the medium was removed and the cells were washed once with 1 ml of room temperature NaCl 0.9% solution. Then the plates were snap frozen in liquid nitrogen. Metabolite extraction, derivatization and analysis were previously described (61). Metabolites were extracted on dry ice/ice with 800 µL cold 62.5% methanol in water, containing norvaline and glutarate as internal standards. Cells were scraped and 500 µL ice cold chloroform and C17, heptadecanoic acid, as an internal standard, were added. The samples were vortexed at 4°C to extract metabolites, centrifuged for 10 min and the phases were separated. For measurements of polar metabolites, the methanol water phase was dried at 4°C by vacuum centrifugation.

For GC-MS, samples were derivatized. Methoxyamine in pyridine (20 mg/ml, Sigma) was added and samples were incubated at 37°C for 90 min, N-(tert-butyldimethylsilyl)-N-methyl-trifluoroacetamide (TBDMS) was added for 1h at 60°C. Separation occurred with an Agilent 7890A GC system coupled to an Agilent 5975C Inert MS system, the column used was a DB35MS column and helium was used as a carrier gas at a flow rate of 1 mL min^{-1}. A volume of 1 µL of sample was injected in splitless mode with an inlet temperature of 270°C. The GC

oven was kept at 100°C for 1 min, increased up to 105°C with a gradient of 2.5°C min^{-1}, then ramped to 240°C with a gradient of 3.5°C min^{-1}, and after that ramped up to 320°C with a gradient of 2.5°C min^{-1}, which was followed by 4 min at 320°C. Mass spectrometry was performed at 70 eV and a mass range of 100-650 atomic mass units was measured. Isotopologue distributions of the metabolites were quantified, normalized to protein and corrected for natural abundance with a MATLAB Script (MA, USA).

Sample preparation for the detection of metabolites by LC-MS occurred as previously stated for GC-MS measurements. A Dionex UltiMate 3000 LC System (Thermo Scientific) was coupled to a Q-Exactive Orbitrap mass spectrometer (Thermo Scientific). Samples were resuspended 50 µl of H_2O. Separation was achieved with a flow rate of 0.25 ml min^{-1}, by utilizing a C18 column (Acquity UPLC HSS T3 1.8 µm 2.1 × 100 mm) at 40°C and a gradient for 40 min (solvent A: 0 H_2O, 10 mM tributyl-amine, 15 mM acetic acid - solvent B:Methanol) (0 min: 0% B, 2 min: 0% B, 7 min:37% B, 14 min: 41% B, 26 min: 100% B, 30 min: 100% B, 31 min: 0% B; 40 min: 0% B). The MS operated in negative full scan mode (m/z range: 70–900) using a spray voltage of 4.9 kV, capillary temperature of 320°C, sheath gas at 50.0 and auxiliary gas at 10.0. Data was collected and analyzed using the Xcalibur software (Thermo Scientific).

Measurement of whole-cellular NAD/NADH

To measure whole cellular NAD/NADH levels, the NAD/NADH Glo-Assay kit from Promega was used and optimized for neuronal cells. In brief, cells were prepared as described in the metabolic labelling section. After snap-freezing in liquid nitrogen, the cells were lysed using a 1% DTAB in 0.2 M NaOH/PBS (50:50) solution. A tenth of the sample was taken separately and mixed with 25ul of 0.4N HCl to measure NAD+ and the same volume was taken aside to measure NADH without any addition. Both samples were incubated at 60°C for 15 minutes and then equilibrated to room temperature. Afterwards, 25 µl of 0.4N Tris base was

added to the NAD+ tube and 50 µl of 1:1 0.4N HCl/Tris was added to one of NADH to neutralize and equalize the pH. At last, 30ul of the NAD+ and NADH tubes were mixed with the luminescence mix from the kit and incubated for 1h at room temperature before measuring the luminescence with the Microplate Luminometer LB 96V from EG&G Berthold.

Proteomics for measurement of protein turnover

Mouse cells were obtained from primary culture of timed pregnant mouse embryos at E13.5-E14.5 as described in the previous section and were plated on 6-well plates that had previously been coated with laminin- and poly-D-lysin overnight at 37°C and horse serum 1h at 37°C, or on coverslips, at 200,000 cells/cm^2 using NbB27x medium with Penicillin-Streptomycin (50U/ml). Plated cells were incubated at 37℃ with 5% CO_2. DAPT (10µM) was added to the medium from DIV1 to DIV3. At DIV6, the medium was changed to Neurobasal without glucose, Lysin and Arginin (Customized, Thermofisher) with B27 supplement minus Vitamin A (1x, Thermo Fisher Scientific, Cat#12587010), GlutaMAX supplement (1x, Thermo Fisher Scientific, Cat# 35050061), Glucose (2.5mM, Thermo Fisher Scientific, Cat#A2494001), L-Lysine-13C6 hydrochloride (0.798mM, Sigma-Aldrich, cat#643459-250MG), L-Arginine-13C6 hydrochloride (0.398mM, Sigma-Aldrich, cat#643440-250MG). Half of the medium was changed every other day. At DIV6 prior to the start of the labelling, and at DIV7, 9 and 12, protein extraction was performed using a freshly made Urea lysis buffer containing 8M Urea (Sigma-Aldrich, Cat# U5378), 30mM Tris, 5mM dithiothreitol (Sigma-Aldrich, Cat# D0632) and 1x Protease inhibitor (Roche). Briefly, culture medium is removed, cells are washed once with ice-cold PBS, Urea lysis buffer is added to the cells. After 30 minutes incubation in Urea lysis buffer at room temperature, the lysate is centrifugated for 10 min at 14,000 xg. The supernatant is aliquoted and snap frozen. For tryptic digestion, DTT was added to the 20 µg protein-containing sample up to a final concentration of 20 mM, gently vortexed, and incubated for 15 min. Iodoacetamide was

added to the samples up to a final concentration of 50 mM and vortexed before it was incubated for 30 min in the dark. Samples were diluted 4 times with a stock solution of 150 mM ammonium bicarbonate in order to reduce urea concentration from 8 to 2 M. Trypsin was added in a ratio of 0.2 µg trypsin/20 µg extracted protein and incubated overnight at 37 °C. Samples were acidified with trifluoroacetic acid (0.1% final concentration) and de-salted using C18 solid phase extraction according to the manufacturer (Pierce™ C18 Spin Columns, Thermo Fisher Scientific, Gent, Belgium). Peptides were eluted with 40 µl 70% ACN, after which solvents were evaporated using a speed vac and dissolved in 5% ACN, 0.1% formic acid.

Human cortical cells (frozen at day 25) were thawed and plated on Matrigel-coated plates using DDM/B27+Nb/B27 medium at 37˚C with 5% CO_2. Seven days after thawing (day 32), the cells were dissociated using Accutase and plated on Matrigel-coated plate at high confluency (450,000-700,000 cells/cm2). Four days later (day 36), the medium was changed to DDM/B27+Nb/B27 medium with 10µM DAPT. Two days after 4-OHT/DAPT induction (day 38), the medium was changed to fresh DDM/B27+Nb/B27 medium. At day 40, cortical cells were dissociated using NeuroCult Enzymatic Dissociation Kit following manufacturer's instructions. For L1CAM+ MACS, dissociated cells were incubated with biotin conjugated anti-human CD171(L1CAM) (Miltenyi Biotec, Cat#130-124-046) in MACS buffer at 4˚C for 10 min. After washing using MACS buffer, human cells were incubated with anti-biotin microbeads (Miltenyi Biotec, Cat#130-090-485) in MACS buffer at 4˚C for 15 min. L1CAM positive selection were carried out with LS columns according to the manufacturer's instructions. The sorted cells were plated on Poly-L-ornithine-, Laminin- and horse serum-coated 6-well plate at 110,000 cells/cm^2. The sorted cells were maintained in Nb/B27 low glucose medium. At day53, the medium was changed to Neurobasal without glucose, Lysin and Arginin (Customized, Thermofisher) with B27 supplement minus Vitamin A (1x, Thermo Fisher Scientific, Cat#12587010), GlutaMAX supplement (1x, Thermo Fisher Scientific, Cat#

35050061), Glucose (2.5mM, Thermo Fisher Scientific, Cat#A2494001), L-Lysine-13C6 hydrochloride (0.798mM, Sigma-Aldrich, cat#643459-250MG), L-Arginine-13C6 hydrochloride (0.398mM, Sigma-Aldrich, cat#643440-250MG). Half of the medium was changed every other day. At day53 prior to the start of the labelling, and at day54, 56 and 59, protein extraction was performed same as above.

The digested samples (0.5 µg) were injected (5 µL) and separated on an Ultimate 3000 UPLC system (Dionex, Thermo Scientific) equipped with an Acclaim PepMap 100 pre-column (C18 3 µm–100 Å, Thermo Scientific) and a C18 PepMap RSLC (2 µm, 75 µm-50 cm, Thermo Scientific) using a linear gradient (300 nL/min) of 0–4% buffer B (80% ACN, 0.08% FA) in 3 min, 4–12% B in 17 min, 12–15% in 10 min, 15–18% in 45min, 18–20% in 40min, 20–30% in 65min , 30–35% in 30min, 35–65% in 10min, 65–95% in 5 min 95% for 40 min, 95–4% in 1 min, 4% for 39 min. The Orbitrap Elite Velos Pro ETD mass spectrometer (Thermo Scientific) was operated in positive ion mode with a nanospray voltage of 1.8 kV and a source temperature of 275 °C. Pierce LTQ Velos ESI positive ion calibration mix (88323, Thermo Scientific) was used as an external calibrant. The instrument was operated in data-dependent acquisition mode with a survey MS scan at a resolution of 60,000 for the mass range of m/z 375–1500 for precursor ions, followed by MS/MS scans of the top 20 most intense peaks with +2, +3, +4, and above charged ions above a minimum signal threshold count of 500 at Rapid resolution setting of ion trap using normalized collision energy (NCE) of 35 eV with an isolation window of 2.0 m/z, and dynamic exclusion of 10 s. All data were acquired with Xcalibur 3.0.63.3 software (Thermo Scientific). For peptide quantification, all raw file were loaded into the software Progenesis QI for proteomics®v4.2 (Nonlinear Dynamics, Waters). We applied MASCOT version 2.2.06 (Matrix Science) to identify the spectra and import the results back into Progenesis. The spectra were searched against the human uniprot proteome using the search parameters parent mass tolerance of 12 PPM, fragment tolerance of 0.5 Da. As variable modification we accepted oxidation M,

Deamidation NQ, 13C (R), 13C (K). As fixed modification carbamidomethyl C was set and up to two missed cleavages for trypsin were allowed. Quantitation was set at SILAC K+6 R+6. All spectra were only searched against the human data base and hence only identical peptides in both species were considered. All identifications and quantitative values for all features were exported from Progenesis as csv file. To calculate the ratio of labelled vs non-labelled protein, the corresponding m/z pairs were selected, their ratio labelled/ non labelled was calculated and the average ratio for all identified peptides was calculated for each individual sample.

Electrophysiological recordings

Human cortical cells (frozen at day 25) were thawed and plated on Matrigel-coated plates using DDM/B27+Nb/B27 medium at 37˚C with 5% CO_2. Seven days after thawing (day 32), the cells were dissociated using Accutase and plated on Matrigel-coated plate at high confluency (450,000-700,000 cells/cm2). Four days later (day 36), the medium was changed to DDM/B27+Nb/B27 medium with 10µM DAPT. Two days after 4-OHT/DAPT induction (day 38), the medium was changed to fresh DDM/B27+Nb/B27 medium. At day 40, cortical cells were dissociated using NeuroCult Enzymatic Dissociation Kit following manufacturer's instructions. For L1CAM+ MACS, dissociated cells were incubated with biotin conjugated anti-human L1CAM in MACS buffer at 4˚C for 10 min. After washing using MACS buffer, human cells were incubated with anti-biotin microbeads in MACS buffer at 4˚C for 15 min. L1CAM positive selection were carried out with LS columns according to the manufacturer's instructions. The sorted cells were plated on mouse astrocyte-coated coverslips at 110,000 cells/cm^2.

The patch pipette solution contained (in mM): 135 K-Gluconate, 4 KCl, 10 HEPES, 4 Mg-ATP, 0.3 Na2-GTP, 10 Na2-phospocreatine, 3 biocytin (pH 7.3). For the recordings, the glass coverslips were transferred into a recording chamber where they were continuously

perfused (2–3mL/min) with the extracellular solution at room temperature. The external medium used contained the following components (in mM): 140 NaCl, 2.4 KCl, 4 CaCl2, 4 MgCl2, 10 HEPES, 10 Glucose and 20 μM bicuculline methiodide (300 mOsm, pH 7.40). For recording sEPSCs and sodium currents, cells were whole-cell voltage clamped at −70 mV with a double EPC-10 amplifier (HEKA Elektronik, Lambrecht/Pfalz, Germany) under control of Patchmaster v2x32 software (HEKA Elektronik). Currents were low-pass filtered at 3 kHz and stored at 20 kHz. Cell intrinsic properties were measured in current clamp from the same cells. Patch pipettes were pulled from borosilicate glass using a multi-step puller (P-1000; Sutter Instruments; 3-5 MΩ). The series resistance was compensated to ~70%. Only cells with series resistances below 12 MΩ were included for analysis. Fitmaster (HEKA Electroniks) was used for offline analysis of cell intrinsic parameters. sEPSCs were detected using Mini Analysis program (Synaptosoft).

Detection of KCl-induced NPAS4 expression

For NPAS4 expression level comparison at different time points (Fig. 10C), the human cortical cells (frozen at day 25) were thawed and plated on Matrigel-coated plates using DDM/B27+Nb/B27 medium at 37˚C with 5% CO_2. At seven days after thawing (day 32), cells were dissociated using Accutase and plated on Matrigel-coated plate at high confluency (450,000-700,000 cells/cm2) with LV-NeuroD1 promoter-CreERT2-WPRE and LV-CAG-DIO-tCD8-WPRE. At four days later (day 36), medium was changed to DDM/B27+Nb/B27 medium with 1μM 4-OHT and 10μM DAPT. Two days after 4-OHT/DAPT induction (day 38), medium was changed to fresh DDM/B27+Nb/B27 medium. At day 40, cortical cells were dissociated using NeuroCult Enzymatic Dissociation Kit following manufacturer's instructions. For CD8+ MACS, dissociated cells were incubated with magnetic beads conjugated anti-human CD8 in MACS buffer at 4˚C for 10 min. CD8 positive selection were carried out with LS columns according to the manufacturer's instructions. The sorted cells

were plated on mouse astrocyte-coated coverslips or Poly-L-ornithine-, Laminin- and horse serum-coated coverslips at 110,000 cells/cm^2. The DDM/B27+Nb/B27 medium was changed twice a week. At indicated time points, 50mM KCl depolarization solution was prepared by adding 0.41 volume of pre-mixture solution (170mM KCl, 1mM $MgCl_2$, 2mM $CaCl_2$, 10mM HEPES (pH7.2)) to DDM/B27+Nb/B27 medium with FPL64176 (5μM, Tocris, Cat#1403) and D-AP5 (5μM, Tocris, Cat#0106) to prevent excitotoxicity. The DDM/B27+Nb/B27 medium was removed and replaced by pre-warmed 50mM KCl depolarization solution. After 1h incubation at 37˚C with 5% CO_2, the depolarization solution was completely removed and replaced by fresh DDM/B27+Nb/B27 medium. 2h after removing depolarization solution, coverslips were fixed with 4% PFA and immunostained with anti-NPAS4 and anti-MAP2 antibodies.

Impact of metabolic modulators on KCl-induced NPAS4 expression

Human cortical cells (frozen at day 25) were thawed and plated on Matrigel-coated plates using DDM/B27+Nb/B27 medium at 37˚C with 5% CO_2. Seven days after thawing (day 32), the cells were dissociated using Accutase and plated on Matrigel-coated plate at high confluency (450,000-700,000 cells/cm2) with LV-NeuroD1 promoter-CreERT2-WPRE and LV-CAG-DIO-tCD8-WPRE. Four days later (day 36), the medium was changed to DDM/B27+Nb/B27 medium with 1μM 4-OHT and 10μM DAPT. Two days after 4-OHT/DAPT induction (day 38), the medium was changed to fresh DDM/B27+Nb/B27 medium. At day 40, cortical cells were dissociated using NeuroCult Enzymatic Dissociation Kit following manufacturer's instructions. For CD8+ MACS, dissociated cells were incubated with magnetic beads conjugated anti-human CD8 in MACS buffer at 4˚C for 10 min. CD8 positive selection were carried out with LS columns according to the manufacturer's instructions. The sorted cells were plated on mouse astrocyte-coated coverslips at 110,000 cells/cm^2 (Fig.10D) and on Poly-L-ornithine-, Laminin- and horse serum-coated coverslips at 110,000

cells/cm^2. At day 45, DDM/B27+Nb/B27 medium was changed to following: (1: DMSO) Nb/B27 low glucose medium with DMSO (1:2,000, Merck, Cat#D2650); (2: PS10) Nb/B27 low glucose medium with PS10 (5μM, MedChemExpress, Cat#HY-121744); (3: GSK) Nb/B27 low glucose medium with GSK-2837808A (5μM, MedChemExpress, Cat#HY-100681); (4: AlbuMAX+DMSO) Nb/B27 low glucose medium with DMSO (1:2,000) and AlbuMAX (0.5%, Thermo Fisher Scientific, Cat#11020021); (5: AlbuMAX+PS10) Nb/B27 low glucose medium with PS10 (5μM) and AlbuMAX (0.5%); (6: AlbuMAX+GSK) Nb/B27 low glucose medium with GSK-2837808A (5μM) and AlbuMAX (0.5%). These media were changed every other day until day 59. At day 59, these media were completely changed to fresh Nb/B27 medium. Twenty-four hours later, Nb/B27 medium was removed and pre-warmed 50mM KCl depolarization solution (a mixture of Nb/B27 medium and pre-mixture solution) was added to the cells. After 1h incubation at 37˚C with 5% CO_2, the depolarization solution was completely removed and fresh Nb/B27 medium was added to the cells. 2h after removing the depolarization solution, coverslips were fixed with 4% PFA and immunostained with anti-NPAS4 and anti-human nuclei antibodies. For image acquisition, a Märzhäuser Slide Express 2 attached to a Nikon NiE inverted microscope was used in combination with a 10x Plan Apo lambda objective lens (NA 0.45). The setup was controlled by NIS-Element (5.21.03 build 1489, Nikon Instruments Europe B.V.). For illumination a Spectra III lightsource was used. DAPI was excited at 365nm, human nuclei were excited at 488nm, and NPAS4 was excited at 561nm. Signals were collected with a pentacube emission filter (420-460 / 510-531 / 590-624). The entire coverslip was imaged (without border) using a tilescan, z-stack (3 planes, 15μm step size). For post processing/image analysis, a NIS-Elements 5.30.01 (Nikon) was used. Five regions of interest (ROI, 1320x1320 μm) were selected form one coverslip for analysis. The human nuclei signal was used to determine the area in which to measure the signal intensity of NPAS4. For quantification of NPAS4+ cells, NPAS4 staining-derived “background signal” was acquired from the NPAS4/human

nuclei-immunostained cells that did not receive the KCl treatment. This background signal was used as a threshold to distinguish NPAS4 positive vs. negative cells. The ratios of NPAS4+ human nuclei of each ROI were calculated by applying this threshold.

Neuronal morphology analysis of NNN-labeled cell

For morphology analysis of chemical compound treated human neurons (Fig. 5A,B), human cortical cells (frozen at day 25) were thawed and plated on Matrigel-coated plates using DDM/B27+Nb/B27 medium at 37˚C with 5% CO_2. Seven days after thawing (day 32), the cells were dissociated using Accutase and plated on Matrigel-coated plate at high confluency (450,000-700,000 cells/cm2) with LV-NeuroD1 promoter-CreERT2-WPRE and LV-CAG-DIO-tCD8-WPRE or LV-CAG-DIO-EGFP-T2A-tCD8-WPRE. Four days later (day 36), the medium was changed to DDM/B27+Nb/B27 medium with 1μM 4-OHT and 10μM DAPT. Two days after 4-OHT/DAPT induction (day 38), the medium was changed to fresh DDM/B27+Nb/B27 medium. At day 40, the cortical cells were dissociated using NeuroCult Enzymatic Dissociation Kit following manufacturer's instructions. For CD8+ MACS, dissociated cells were incubated with magnetic beads conjugated anti-human CD8 in MACS buffer at 4˚C for 10 min. CD8 positive selection was carried out with LS columns according to the manufacturer's instructions. The sorted cells were plated on mouse astrocyte-coated coverslips at 110,000 cells/cm^2 with a ratio of DIO-tCD8-infected to DIO-EGFP-T2A-tCD8-infected cells of 10:1. At day 45, DDM/B27+Nb/B27 medium was changed to the following: (1: DMSO) Nb/B27 low glucose medium with DMSO (1:4,000); (2: GSK) Nb/B27 low glucose medium with GSK-2837808A (5μM); (3: AlbuMAX+GSK) Nb/B27 low glucose medium with GSK-2837808A (5μM) and AlbuMAX (0.5%). These media were changed every other day. At day 60, the coverslips were fixed with 4% PFA and immunostained with anti-NPAS4, anti-FoxG1 and anti-MAP2 antibodies.

For morphology analysis of chemical compound treated mouse neurons (Fig. 5C-F, Fig. S19), mouse cells were obtained from primary culture of timed pregnant mouse embryos at E13.5 as described before and were plated on coverslips in 12-well plates that had previously been coated with laminin- and poly-D-lysin overnight at 37°C and horse serum 1h at 37°C, at 200,000 cells/cm^2 using NbB27x medium with Penicillin-Streptomycin (50U/ml) and with LV-NeuroD1 promoter-CreERT2 and LV-CAG-DIO-GFP-WPRE. The day after (DIV1), the medium was changed Nb/B27x medium with 1μM 4-OHT and 10μM DAPT. Two days after 4-OHT/DAPT induction (DIV3), the medium was changed as follow: for cells treated with AlbuMAX+GSK, the medium was changed to (1:DMSO) Nb/B27 low glucose medium with DMSO (1:4,000), (2: AlbuMAX+GSK) Nb/B27 low glucose medium with GSK-2837808A (5μM) and AlbuMAX (0.5%); for cells treated with Rotenone, the medium was changed to (1:DMSO) Nb/B27x medium with DMSO (1/5,000,000), (2: Rotenone) Nb/B27x medium with 21 nM Rotenone (Sigma-Aldrich, Cat#R8875); for the cells treated with mitochondrial pyruvate carrier blocker UK-5099, the medium was changed to (1:DMSO) Nb/B27x medium with DMSO (1/40,000), (2:UK-5099) Nb/B27x medium with 2,5 μM UK-5099 (Sigma-Aldrich, Cat# PZ0169). These media were changed every other day. At DIV8 and DIV14, the coverslips were fixed with 4% PFA and immunostained with anti-GFP and anti-Synapsin1 antibodies.

Morphologies were imaged on a Zeiss LSM880 confocal microscope, using 25x objective, and a vertical resolution of 0.9-1.2μm/pixel. For each cell, a z-stack of 10-20 images was acquired centered on the cell of interest. A maximal intensity projection image was performed on NNN-labeled FoxG1+ neuron. For dendritic morphology analysis, GFP images were traced analyzed by using Sholl analysis with the “Simple Neurite Tracer” plugin on Fiji. The cell body area was quantified based on GFP signal of the maximal intensity projection image by Fiji.

Statistical analysis

All statistical analyses were performed using GraphPad Prism 9 (GraphPad Software) or SigmaPlot 12.5 (Systat Software Inc). A Kolmogorov-Smirnov test or Shapiro-Wilk normality test was used to test the normality. Parametric data were analyzed by t-test, one-way or two-way ANOVA followed by Dunnett's, or Tukey's post hoc analysis for comparisons of multiple samples. Non-parametric data were analyzed by the Mann-Whitney test followed by Dunn's post hoc analysis for comparisons of multiple samples. P values < 0.05 were considered statistically significant. Data are presented as mean ± SEM or median.

Abstract

Neuronal development in the human cerebral cortex is considerably prolonged compared to that of other mammals. It results in extended critical periods of learning and plasticity that have been proposed to play a role in the acquisition of human-specific cognitive features. In mammals, the rate of embryonic development is correlated to the resting metabolic rate as assessed by oxygen consumption. Within the cell, mitochondria are the site of oxidative phosphorylation. Mitochondria have also been linked to neuronal development and plasticity, in particular to the morphology of dendrites, spines and synapses. We explored whether mitochondria influence the species-specific timing of cortical neuron maturation. During cortical neuron maturation, we documented a progressive increase of mitochondrial size, quantity and activity. By comparing human and mouse cortical neuronal maturation at high temporal and cell resolution, we found a slower mitochondria development in human cortical neurons compared with that in the mouse, together with lower mitochondria metabolic activity, particularly that of oxidative phosphorylation. Stimulation of mitochondria metabolism in human neurons resulted in accelerated development *in vitro* and *in vivo*, leading to maturation of cells weeks ahead of time, whereas its inhibition in mouse neurons led to decreased rates of maturation. Mitochondria are thus important regulators of the pace of neuronal development underlying human-specific brain neoteny.

Uittreksel

De neuronale ontwikkeling, met name de rijping van corticale neuronen in het menselijk brein, duurt aanzienlijk langer dan bij andere zoogdieren. Over het algemeen verloopt de embryonale ontwikkeling sneller bij kleinere dieren dan bij grotere, waarbij kleinere dieren een hoger basaal metabolisme en mitochondriale activiteit vertonen. In zowel menselijke als muizen corticale neuronen leidt een toename van mitochondriale activiteit tot versnelde

rijping, terwijl een afname van deze activiteit resulteert in vertraagde rijping. Mitochondriale activiteit vormt dus een intrinsiek celmechanisme dat het tempo van neuronale ontwikkeling en de onderliggende mensspecifieke neotenie reguleert.

References

1. E. Bufill, J. Agustí, R. Blesa, Human neoteny revisited: The case of synaptic plasticity. *American Journal of Human Biology* **23**, 729–739 (2011).
2. S. J. Gould, Roots: Ontogeny and phylogeny – revisited and reunited. *BioEssays* **14**, 275–279 (1992).
3. Finlay et Darlington - 1995 - Linked regularities in the development and evoluti.pdf.
4. S. Herculano-Houzel, The human brain in numbers: a linearly scaled-up primate brain. *Front. Hum. Neurosci.* **3** (2009).
5. A. M. M. Sousa, K. A. Meyer, G. Santpere, F. O. Gulden, N. Sestan, Evolution of the Human Nervous System Function, Structure, and Development. *Cell* **170**, 226–247 (2017).
6. S. Herculano-Houzel, B. Mota, R. Lent, Cellular scaling rules for rodent brains. *Proc. Natl. Acad. Sci. U.S.A.* **103**, 12138–12143 (2006).
7. S. Herculano-Houzel, C. E. Collins, P. Wong, J. H. Kaas, Cellular scaling rules for primate brains. *Proceedings of the National Academy of Sciences* **104**, 3562–3567 (2007).
8. M. P. van den Heuvel, E. T. Bullmore, O. Sporns, Comparative Connectomics. *Trends in Cognitive Sciences* **20**, 345–361 (2016).
9. D. C. Van Essen, C. J. Donahue, T. S. Coalson, H. Kennedy, T. Hayashi, M. F. Glasser, Cerebral cortical folding, parcellation, and connectivity in humans, nonhuman primates, and mice. *Proceedings of the National Academy of Sciences* **116**, 26173–26180 (2019).
10. J. K. Rilling, Human and nonhuman primate brains: Are they allometrically scaled versions of the same design? *Evolutionary Anthropology: Issues, News, and Reviews* **15**, 65–77 (2006).
11. S. Bianchi, C. D. Stimpson, A. L. Bauernfeind, S. J. Schapiro, W. B. Baze, M. J. McArthur, E. Bronson, W. D. Hopkins, K. Semendeferi, B. Jacobs, P. R. Hof, C. C. Sherwood, Dendritic Morphology of Pyramidal Neurons in the Chimpanzee Neocortex: Regional Specializations and Comparison to Humans. *Cereb Cortex* **23**, 2429–2436 (2013).
12. G. N. Elston, R. Benavides-Piccione, J. DeFelipe, The pyramidal cell in cognition: a comparative study in human and monkey. *J. Neurosci.* **21**, RC163 (2001).
13. G. Elston, R. Benavides-Piccione, A. Elston, P. Manger, J. Defelipe, Pyramidal Cells in Prefrontal Cortex of Primates: Marked Differences in Neuronal Structure Among Species. *Frontiers in Neuroanatomy* **5** (2011).
14. G. N. Elston, I. Fujita, Pyramidal cell development: postnatal spinogenesis, dendritic growth, axon growth, and electrophysiology. *Front. Neuroanat.* **8** (2014).
15. B. Libé-Philippot, P. Vanderhaeghen, Cellular and Molecular Mechanisms Linking Human Cortical Development and Evolution. *Annu Rev Genet* **55**, 555–581 (2021).
16. H. B. Uylings, J. van Pelt, J. G. Parnavelas, A. Ruiz-Marcos, Geometrical and topological characteristics in the dendritic development of cortical pyramidal and non-pyramidal neurons. *Prog Brain Res* **102**, 109–123 (1994).
17. P. Rakic, J. P. Bourgeois, M. F. Eckenhoff, N. Zecevic, P. S. Goldman-Rakic, Concurrent overproduction of synapses in diverse regions of the primate cerebral cortex. *Science* **232**, 232–235 (1986).
18. I. Espuny-Camacho, K. A. Michelsen, D. Gall, D. Linaro, A. Hasche, J. Bonnefont, C. Bali, D. Orduz, A. Bilheu, A. Herpoel, N. Lambert, N. Gaspard, S. Péron, S. N. Schiffmann, M. Giugliano, A. Gaillard, P. Vanderhaeghen, Pyramidal Neurons Derived from Human Pluripotent Stem Cells Integrate Efficiently into Mouse Brain Circuits In Vivo. *Neuron* **77**, 440–456 (2013).

19. Z. Petanjek, M. Judaš, G. Šimić, M. R. Rašin, H. B. M. Uylings, P. Rakic, I. Kostović, Extraordinary neoteny of synaptic spines in the human prefrontal cortex. *PNAS* **108**, 13281–13286 (2011).
20. J. Grutzendler, N. Kasthuri, W.-B. Gan, Long-term dendritic spine stability in the adult cortex. *Nature* **420**, 812–816 (2002).
21. Z. Petanjek, M. Judas, I. Kostović, H. B. M. Uylings, Lifespan alterations of basal dendritic trees of pyramidal neurons in the human prefrontal cortex: a layer-specific pattern. *Cereb Cortex* **18**, 915–929 (2008).
22. L. Mrzljak, H. B. Uylings, C. G. Van Eden, M. Judás, Neuronal development in human prefrontal cortex in prenatal and postnatal stages. *Prog Brain Res* **85**, 185–222 (1990).
23. P. R. Huttenlocher, A. S. Dabholkar, Regional differences in synaptogenesis in human cerebral cortex. *J. Comp. Neurol.* **387**, 167–178 (1997).
24. H. T. Chugani, M. E. Phelps, J. C. Mazziotta, Positron emission tomography study of human brain functional development. *Annals of Neurology* **22**, 487–497 (1987).
25. H. T. Chugani, Review : Metabolic Imaging: A Window on Brain Development and Plasticity. *Neuroscientist* **5**, 29–40 (1999).
26. C. Kennedy, G. D. Grave, J. W. Juhle, L. Sokoloff, Changes in blood flow in the component structures of the dog brain during postnatal maturation. *J Neurochem* **19**, 2423–2433 (1972).
27. D. B. Tyler, A. van Harreveld, The respiration of the developing brain. *American Journal of Physiology-Legacy Content* **136**, 600–603 (1942).
28. N. M. Porter, O. Thibault, V. Thibault, K.-C. Chen, P. W. Landfield, Calcium Channel Density and Hippocampal Cell Death with Age in Long-Term Culture. *J Neurosci* **17**, 5629–5639 (1997).
29. C. Lesuisse, L. J. Martin, Long-term culture of mouse cortical neurons as a model for neuronal development, aging, and death. *Journal of Neurobiology* **51**, 9–23 (2002).
30. M. Eiraku, K. Watanabe, M. Matsuo-Takasaki, M. Kawada, S. Yonemura, M. Matsumura, T. Wataya, A. Nishiyama, K. Muguruma, Y. Sasai, Self-organized formation of polarized cortical tissues from ESCs and its active manipulation by extrinsic signals. *Cell Stem Cell* **3**, 519–532 (2008).
31. T. Otani, M. C. Marchetto, F. H. Gage, B. D. Simons, F. J. Livesey, 2D and 3D Stem Cell Models of Primate Cortical Development Identify Species-Specific Differences in Progenitor Behavior Contributing to Brain Size. *Cell Stem Cell* **18**, 467–480 (2016).
32. X. Tang, L. Zhou, A. M. Wagner, M. C. N. Marchetto, A. R. Muotri, F. H. Gage, G. Chen, Astroglial cells regulate the developmental timeline of human neurons differentiated from induced pluripotent stem cells. *Stem Cell Res* **11**, 743–757 (2013).
33. O. Blondel, C. Collin, W. J. McCarran, S. Zhu, R. Zamostiano, I. Gozes, D. E. Brenneman, R. D. McKay, A glia-derived signal regulating neuronal differentiation. *J. Neurosci.* **20**, 8012–8020 (2000).
34. D. Prè, M. W. Nestor, A. A. Sproul, S. Jacob, P. Koppensteiner, V. Chinchalongporn, M. Zimmer, A. Yamamoto, S. A. Noggle, O. Arancio, A Time Course Analysis of the Electrophysiological Properties of Neurons Differentiated from Human Induced Pluripotent Stem Cells (iPSCs). *PLoS One* **9** (2014).
35. F. W. Pfrieger, B. A. Barres, Synaptic efficacy enhanced by glial cells in vitro. *Science* **277**, 1684–1687 (1997).
36. E. M. Ullian, S. K. Sapperstein, K. S. Christopherson, B. A. Barres, Control of synapse number by glia. *Science* **291**, 657–661 (2001).
37. K. S. Christopherson, E. M. Ullian, C. C. A. Stokes, C. E. Mullowney, J. W. Hell, A. Agah, J. Lawler, D. F. Mosher, P. Bornstein, B. A. Barres, Thrombospondins are astrocyte-secreted proteins that promote CNS synaptogenesis. *Cell* **120**, 421–433 (2005).
38. D. Linaro, B. Vermaercke, R. Iwata, A. Ramaswamy, B. Libé-Philippot, L. Boubakar,

B. A. Davis, K. Wierda, K. Davie, S. Poovathingal, P.-A. Penttila, A. Bilheu, L. De Bruyne, D. Gall, K.-K. Conzelmann, V. Bonin, P. Vanderhaeghen, Xenotransplanted Human Cortical Neurons Reveal Species-Specific Development and Functional Integration into Mouse Visual Circuits. *Neuron* **104**, 972-986.e6 (2019).
39. M. C. Marchetto, B. Hrvoj-Mihic, B. E. Kerman, D. X. Yu, K. C. Vadodaria, S. B. Linker, I. Narvaiza, R. Santos, A. M. Denli, A. P. Mendes, R. Oefner, J. Cook, L. McHenry, J. M. Grasmick, K. Heard, C. Fredlender, L. Randolph-Moore, R. Kshirsagar, R. Xenitopoulos, G. Chou, N. Hah, A. R. Muotri, K. Padmanabhan, K. Semendeferi, F. H. Gage, Species-specific maturation profiles of human, chimpanzee and bonobo neural cells. *eLife* **8**, e37527 (2019).
40. M. Schörnig, X. Ju, L. Fast, S. Ebert, A. Weigert, S. Kanton, T. Schaffer, N. Nadif Kasri, B. Treutlein, B. M. Peter, W. Hevers, E. Taverna, Comparison of induced neurons reveals slower structural and functional maturation in humans than in apes. *eLife* **10**, e59323 (2021).
41. Y. Zhang, C. Pak, Y. Han, H. Ahlenius, Z. Zhang, S. Chanda, S. Marro, C. Patzke, C. Acuna, J. Covy, W. Xu, N. Yang, T. Danko, L. Chen, M. Wernig, T. C. Südhof, Rapid single-step induction of functional neurons from human pluripotent stem cells. *Neuron* **78**, 785–798 (2013).
42. E. H. Davidson, D. H. Erwin, Gene regulatory networks and the evolution of animal body plans. *Science* **311**, 796–800 (2006).
43. M. Levine, E. H. Davidson, Gene regulatory networks for development. *Proc Natl Acad Sci U S A* **102**, 4936–4942 (2005).
44. J. A. Bailey, Z. Gu, R. A. Clark, K. Reinert, R. V. Samonte, S. Schwartz, M. D. Adams, E. W. Myers, P. W. Li, E. E. Eichler, Recent segmental duplications in the human genome. *Science* **297**, 1003–1007 (2002).
45. P. H. Sudmant, J. O. Kitzman, F. Antonacci, C. Alkan, M. Malig, A. Tsalenko, N. Sampas, L. Bruhn, J. Shendure, 1000 Genomes Project, E. E. Eichler, Diversity of human copy number variation and multicopy genes. *Science* **330**, 641–646 (2010).
46. I. K. Suzuki, D. Gacquer, R. Van Heurck, D. Kumar, M. Wojno, A. Bilheu, A. Herpoel, N. Lambert, J. Cheron, F. Polleux, V. Detours, P. Vanderhaeghen, Human-Specific NOTCH2NL Genes Expand Cortical Neurogenesis through Delta/Notch Regulation. *Cell* **173**, 1370-1384.e16 (2018).
47. C. Charrier, K. Joshi, J. Coutinho-Budd, J.-E. Kim, N. Lambert, J. de Marchena, W.-L. Jin, P. Vanderhaeghen, A. Ghosh, T. Sassa, F. Polleux, Inhibition of SRGAP2 Function by Its Human-Specific Paralogs Induces Neoteny during Spine Maturation. *Cell* **149**, 923–935 (2012).
48. M. Fossati, R. Pizzarelli, E. R. Schmidt, J. V. Kupferman, D. Stroebel, F. Polleux, C. Charrier, SRGAP2 and Its Human-Specific Paralog Co-Regulate the Development of Excitatory and Inhibitory Synapses. *Neuron* **91**, 356–369 (2016).
49. B. Libé-Philippot, R. Iwata, A. J. Recupero, K. Wierda, M. Ditkowska, V. Gaspariunaite, B. Vermaercke, E. Peze-Heidsieck, D. Remans, C. Charrier, F. Polleux, P. Vanderhaeghen, Human synaptic neoteny requires species-specific balancing of SRGAP2-SYNGAP1 cross-inhibition. bioRxiv [Preprint] (2023). https://doi.org/10.1101/2023.03.01.530630.
50. I. T. Fiddes, G. A. Lodewijk, M. Mooring, C. M. Bosworth, A. D. Ewing, G. L. Mantalas, A. M. Novak, A. van den Bout, A. Bishara, J. L. Rosenkrantz, R. Lorig-Roach, A. R. Field, M. Haeussler, L. Russo, A. Bhaduri, T. J. Nowakowski, A. A. Pollen, M. L. Dougherty, X. Nuttle, M.-C. Addor, S. Zwolinski, S. Katzman, A. Kriegstein, E. E. Eichler, S. R. Salama, F. M. J. Jacobs, D. Haussler, Human-Specific NOTCH2NL Genes Affect Notch Signaling and Cortical Neurogenesis. *Cell* **173**, 1356-1369.e22 (2018).
51. W. Enard, S. Gehre, K. Hammerschmidt, S. M. Hölter, T. Blass, M. Somel, M. K. Brückner, C. Schreiweis, C. Winter, R. Sohr, L. Becker, V. Wiebe, B. Nickel, T. Giger, U.

Müller, M. Groszer, T. Adler, A. Aguilar, I. Bolle, J. Calzada-Wack, C. Dalke, N. Ehrhardt, J. Favor, H. Fuchs, V. Gailus-Durner, W. Hans, G. Hölzlwimmer, A. Javaheri, S. Kalaydjiev, M. Kallnik, E. Kling, S. Kunder, I. Moßbrugger, B. Naton, I. Racz, B. Rathkolb, J. Rozman, A. Schrewe, D. H. Busch, J. Graw, B. Ivandic, M. Klingenspor, T. Klopstock, M. Ollert, L. Quintanilla-Martinez, H. Schulz, E. Wolf, W. Wurst, A. Zimmer, S. E. Fisher, R. Morgenstern, T. Arendt, M. Hrabé de Angelis, J. Fischer, J. Schwarz, S. Pääbo, A Humanized Version of Foxp2 Affects Cortico-Basal Ganglia Circuits in Mice. *Cell* **137**, 961–971 (2009).
52. W. Enard, M. Przeworski, S. E. Fisher, C. S. L. Lai, V. Wiebe, T. Kitano, A. P. Monaco, S. Pääbo, Molecular evolution of FOXP2, a gene involved in speech and language. *Nature* **418**, 869–872 (2002).
53. G. Konopka, J. M. Bomar, K. Winden, G. Coppola, Z. O. Jonsson, F. Gao, S. Peng, T. M. Preuss, J. A. Wohlschlegel, D. H. Geschwind, Human-specific transcriptional regulation of CNS development genes by FOXP2. *Nature* **462**, 213–217 (2009).
54. K. S. Pollard, S. R. Salama, N. Lambert, M.-A. Lambot, S. Coppens, J. S. Pedersen, S. Katzman, B. King, C. Onodera, A. Siepel, A. D. Kern, C. Dehay, H. Igel, M. Ares, P. Vanderhaeghen, D. Haussler, An RNA gene expressed during cortical development evolved rapidly in humans. *Nature* **443**, 167–172 (2006).
55. C. Y. McLean, P. L. Reno, A. A. Pollen, A. I. Bassan, T. D. Capellini, C. Guenther, V. B. Indjeian, X. Lim, D. B. Menke, B. T. Schaar, A. M. Wenger, G. Bejerano, D. M. Kingsley, Human-specific loss of regulatory DNA and the evolution of human-specific traits. *Nature* **471**, 216–219 (2011).
56. S. Prabhakar, A. Visel, J. A. Akiyama, M. Shoukry, K. D. Lewis, A. Holt, I. Plajzer-Frick, H. Morrison, D. R. Fitzpatrick, V. Afzal, L. A. Pennacchio, E. M. Rubin, J. P. Noonan, Human-specific gain of function in a developmental enhancer. *Science* **321**, 1346–1350 (2008).
57. J. A. Calarco, Y. Xing, M. Cáceres, J. P. Calarco, X. Xiao, Q. Pan, C. Lee, T. M. Preuss, B. J. Blencowe, Global analysis of alternative splicing differences between humans and chimpanzees. *Genes Dev* **21**, 2963–2975 (2007).
58. A. A. Pollen, A. Bhaduri, M. G. Andrews, T. J. Nowakowski, O. S. Meyerson, M. A. Mostajo-Radji, E. Di Lullo, B. Alvarado, M. Bedolli, M. L. Dougherty, I. T. Fiddes, Z. N. Kronenberg, J. Shuga, A. A. Leyrat, J. A. West, M. Bershteyn, C. B. Lowe, B. J. Pavlovic, S. R. Salama, D. Haussler, E. E. Eichler, A. R. Kriegstein, Establishing Cerebral Organoids as Models of Human-Specific Brain Evolution. *Cell* **176**, 743-756.e17 (2019).
59. Z. He, D. Han, O. Efimova, P. Guijarro, Q. Yu, A. Oleksiak, S. Jiang, K. Anokhin, B. Velichkovsky, S. Grünewald, P. Khaitovich, Comprehensive transcriptome analysis of neocortical layers in humans, chimpanzees and macaques. *Nat Neurosci* **20**, 886–895 (2017).
60. S. Kanton, M. J. Boyle, Z. He, M. Santel, A. Weigert, F. Sanchís-Calleja, P. Guijarro, L. Sidow, J. S. Fleck, D. Han, Z. Qian, M. Heide, W. B. Huttner, P. Khaitovich, S. Pääbo, B. Treutlein, J. G. Camp, Organoid single-cell genomic atlas uncovers human-specific features of brain development. *Nature* **574**, 418–422 (2019).
61. A. Amiri, G. Coppola, S. Scuderi, F. Wu, T. Roychowdhury, F. Liu, S. Pochareddy, Y. Shin, A. Safi, L. Song, Y. Zhu, A. M. M. Sousa, PsychENCODE Consortium, M. Gerstein, G. E. Crawford, N. Sestan, A. Abyzov, F. M. Vaccarino, Transcriptome and epigenome landscape of human cortical development modeled in organoids. *Science* **362**, eaat6720 (2018).
62. Y. Zhu, A. M. M. Sousa, T. Gao, M. Skarica, M. Li, G. Santpere, P. Esteller-Cucala, D. Juan, L. Ferrández-Peral, F. O. Gulden, M. Yang, D. J. Miller, T. Marques-Bonet, Y. Imamura Kawasawa, H. Zhao, N. Sestan, Spatiotemporal transcriptomic divergence across human and macaque brain development. *Science* **362**, eaat8077 (2018).
63. X. Liu, M. Somel, L. Tang, Z. Yan, X. Jiang, S. Guo, Y. Yuan, L. He, A. Oleksiak, Y.

Zhang, N. Li, Y. Hu, W. Chen, Z. Qiu, S. Pääbo, P. Khaitovich, Extension of cortical synaptic development distinguishes humans from chimpanzees and macaques. *Genome Res.* **22**, 611–622 (2012).
64. G. Konopka, T. Friedrich, J. Davis-Turak, K. Winden, M. C. Oldham, F. Gao, L. Chen, G.-Z. Wang, R. Luo, T. M. Preuss, D. H. Geschwind, Human-specific transcriptional networks in the brain. *Neuron* **75**, 601–617 (2012).
65. M. Somel, H. Franz, Z. Yan, A. Lorenc, S. Guo, T. Giger, J. Kelso, B. Nickel, M. Dannemann, S. Bahn, M. J. Webster, C. S. Weickert, M. Lachmann, S. Pääbo, P. Khaitovich, Transcriptional neoteny in the human brain. *PNAS* **106**, 5743–5748 (2009).
66. R. E. Ricklefs, Embryo development and ageing in birds and mammals. *Proc Biol Sci* **273**, 2077–2082 (2006).
67. A. A. Fushan, A. A. Turanov, S.-G. Lee, E. B. Kim, A. V. Lobanov, S. H. Yim, R. Buffenstein, S.-R. Lee, K.-T. Chang, H. Rhee, J.-S. Kim, K.-S. Yang, V. N. Gladyshev, Gene expression defines natural changes in mammalian lifespan. *Aging Cell* **14**, 352–365 (2015).
68. J. R. Speakman, Body size, energy metabolism and lifespan. *J. Exp. Biol.* **208**, 1717–1730 (2005).
69. A. A. Heusner, Body size and energy metabolism. *Annu. Rev. Nutr.* **5**, 267–293 (1985).
70. G. B. West, J. H. Brown, B. J. Enquist, A General Model for the Origin of Allometric Scaling Laws in Biology. *Science* **276**, 122–126 (1997).
71. G. B. West, J. H. Brown, B. J. Enquist, A general model for ontogenetic growth. *Nature* **413**, 628–631 (2001).
72. D. S. Glazier, Is metabolic rate a universal “pacemaker” for biological processes? *Biol Rev Camb Philos Soc* **90**, 377–407 (2015).
73. P. Couture, A. J. Hulbert, Relationship between body mass, tissue metabolic rate, and sodium pump activity in mammalian liver and kidney. *Am J Physiol* **268**, R641-650 (1995).
74. R. Porter, M. Brand, Cellular oxygen consumption depends on body mass. *The American journal of physiology* **269**, R226-8 (1995).
75. R. K. Porter, Allometry of mammalian cellular oxygen consumption. *CMLS, Cell. Mol. Life Sci.* **58**, 815–822 (2001).
76. M. F. Brown, T. P. Gratton, J. A. Stuart, Metabolic rate does not scale with body mass in cultured mammalian cells. *Am J Physiol Regul Integr Comp Physiol* **292**, R2115-2121 (2007).
77. R. K. Porter, A. J. Hulbert, M. D. Brand, Allometry of mitochondrial proton leak: influence of membrane surface area and fatty acid composition. *Am J Physiol* **271**, R1550-1560 (1996).
78. D. C. Chan, Mitochondria: Dynamic Organelles in Disease, Aging, and Development. *Cell* **125**, 1241–1252 (2006).
79. L. Guarente, Mitochondria—A Nexus for Aging, Calorie Restriction, and Sirtuins? *Cell* **132**, 171–176 (2008).
80. T. Wai, T. Langer, Mitochondrial Dynamics and Metabolic Regulation. *Trends in Endocrinology & Metabolism* **27**, 105–117 (2016).
81. D. D. Newmeyer, S. Ferguson-Miller, Mitochondria: releasing power for life and unleashing the machineries of death. *Cell* **112**, 481–490 (2003).
82. R. E. Smith, Quantitative Relations Between Liver Mitochondria Metabolism and Total Body Weight in Mammals. *Annals of the New York Academy of Sciences* **62**, 405–421 (1956).
83. D. L. Drabkin, THE DISTRIBUTION OF THE CHROMOPROTEINS, HEMOGLOBIN, MYOGLOBIN, AND CYTOCHROME c, IN THE TISSUES OF DIFFERENT SPECIES, AND THE RELATIONSHIP OF THE TOTAL CONTENT OF EACH

CHROMOPROTEIN TO BODY MASS. *Journal of Biological Chemistry* **182**, 317–333 (1950).
84. G. De Franciscis, M. F. Futrell, H. O. Kunkel, J. F. Spalding, Cytochrome oxidase activity and body weight in rats and in three species of large animals. *Am J Physiol* **186**, 203–206 (1956).
85. O. Mathieu, R. Krauer, H. Hoppeler, P. Gehr, S. L. Lindstedt, R. M. Alexander, C. R. Taylor, E. R. Weibel, Design of the mammalian respiratory system. VII. Scaling mitochondrial volume in skeletal muscle to body mass. *Respir Physiol* **44**, 113–128 (1981).
86. D. Hu, A. Linders, A. Yamak, C. Correia, J. D. Kijlstra, A. Garakani, L. Xiao, D. J. Milan, P. van der Meer, M. Serra, P. M. Alves, I. J. Domian, Metabolic Maturation of Human Pluripotent Stem Cell-Derived Cardiomyocytes by Inhibition of HIF1α and LDHA. *Circ Res* **123**, 1066–1079 (2018).
87. X. Yang, M. L. Rodriguez, A. Leonard, L. Sun, K. A. Fischer, Y. Wang, J. Ritterhoff, L. Zhao, S. C. Kolwicz, L. Pabon, H. Reinecke, N. J. Sniadecki, R. Tian, H. Ruohola-Baker, H. Xu, C. E. Murry, Fatty Acids Enhance the Maturation of Cardiomyocytes Derived from Human Pluripotent Stem Cells. *Stem Cell Reports* **13**, 657–668 (2019).
88. E. Yoshihara, Z. Wei, C. S. Lin, S. Fang, M. Ahmadian, Y. Kida, T. Tseng, Y. Dai, R. T. Yu, C. Liddle, A. R. Atkins, M. Downes, R. M. Evans, ERRγ is required for the metabolic maturation of therapeutically functional glucose-responsive β cells. *Cell Metab* **23**, 622–634 (2016).
89. C. Correia, A. Koshkin, P. Duarte, D. Hu, A. Teixeira, I. Domian, M. Serra, P. M. Alves, Distinct carbon sources affect structural and functional maturation of cardiomyocytes derived from human pluripotent stem cells. *Sci Rep* **7**, 8590 (2017).
90. M. T. Ryan, N. J. Hoogenraad, Mitochondrial-nuclear communications. *Annu Rev Biochem* **76**, 701–722 (2007).
91. Z. Wu, P. Puigserver, U. Andersson, C. Zhang, G. Adelmant, V. Mootha, A. Troy, S. Cinti, B. Lowell, R. C. Scarpulla, B. M. Spiegelman, Mechanisms controlling mitochondrial biogenesis and respiration through the thermogenic coactivator PGC-1. *Cell* **98**, 115–124 (1999).
92. H. Liang, W. F. Ward, PGC-1alpha: a key regulator of energy metabolism. *Adv Physiol Educ* **30**, 145–151 (2006).
93. A. Cheng, R. Wan, J.-L. Yang, N. Kamimura, T. G. Son, X. Ouyang, Y. Luo, E. Okun, M. P. Mattson, Involvement of PGC-1α in the formation and maintenance of neuronal dendritic spines. *Nature Communications* **3**, 1250 (2012).
94. R. Beckervordersandforth, B. Ebert, I. Schäffner, J. Moss, C. Fiebig, J. Shin, D. L. Moore, L. Ghosh, M. F. Trinchero, C. Stockburger, K. Friedland, K. Steib, J. von Wittgenstein, S. Keiner, C. Redecker, S. M. Hölter, W. Xiang, W. Wurst, R. Jagasia, A. F. Schinder, G.-L. Ming, N. Toni, S. Jessberger, H. Song, D. C. Lie, Role of Mitochondrial Metabolism in the Control of Early Lineage Progression and Aging Phenotypes in Adult Hippocampal Neurogenesis. *Neuron* **93**, 560-573.e6 (2017).
95. A. S. Dickey, S. Strack, PKA/AKAP1 and PP2A/Bβ2 Regulate Neuronal Morphogenesis via Drp1 Phosphorylation and Mitochondrial Bioenergetics. *J. Neurosci.* **31**, 15716–15726 (2011).
96. A. M. Bertholet, A. M. E. Millet, O. Guillermin, M. Daloyau, N. Davezac, M.-C. Miquel, P. Belenguer, OPA1 loss of function affects in vitro neuronal maturation. *Brain* **136**, 1518–1533 (2013).
97. T. Kimura, F. Murakami, Evidence That Dendritic Mitochondria Negatively Regulate Dendritic Branching in Pyramidal Neurons in the Neocortex. *J. Neurosci.* **34**, 6938–6951 (2014).
98. Z. Li, K.-I. Okamoto, Y. Hayashi, M. Sheng, The Importance of Dendritic Mitochondria in the Morphogenesis and Plasticity of Spines and Synapses. *Cell* **119**, 873–887 (2004).

99. V. Rangaraju, M. Lauterbach, E. M. Schuman, Spatially Stable Mitochondrial Compartments Fuel Local Translation during Plasticity. *Cell* **176**, 73-84.e15 (2019).
100. P. Licznerski, H.-A. Park, H. Rolyan, R. Chen, N. Mnatsakanyan, P. Miranda, M. Graham, J. Wu, N. Cruz-Reyes, N. Mehta, S. Sohail, J. Salcedo, E. Song, C. Effman, S. Effman, L. Brandao, G. N. Xu, A. Braker, V. K. Gribkoff, R. J. Levy, E. A. Jonas, ATP Synthase c-Subunit Leak Causes Aberrant Cellular Metabolism in Fragile X Syndrome. *Cell*, doi: 10.1016/j.cell.2020.07.008 (2020).
101. K. Swovick, K. A. Welle, J. R. Hryhorenko, A. Seluanov, V. Gorbunova, S. Ghaemmaghami, Cross-species Comparison of Proteome Turnover Kinetics. *Mol. Cell Proteomics* **17**, 580–591 (2018).
102. K. Swovick, D. Firsanov, K. A. Welle, J. R. Hryhorenko, J. P. Wise, C. George, T. L. Sformo, A. Seluanov, V. Gorbunova, S. Ghaemmaghami, Interspecies Differences in Proteome Turnover Kinetics Are Correlated With Life Spans and Energetic Demands. *Mol Cell Proteomics* **20**, 100041 (2021).
103. J. C. Price, S. Guan, A. Burlingame, S. B. Prusiner, S. Ghaemmaghami, Analysis of proteome dynamics in the mouse brain. *Proceedings of the National Academy of Sciences* **107**, 14508–14513 (2010).
104. C. Catela, P. Kratsios, Transcriptional mechanisms of motor neuron development in vertebrates and invertebrates. *Dev Biol* **475**, 193–204 (2021).
105. T. Rayon, D. Stamataki, R. Perez-Carrasco, L. Garcia-Perez, C. Barrington, M. Melchionda, K. Exelby, J. Lazaro, V. L. J. Tybulewicz, E. M. C. Fisher, J. Briscoe, Species-specific pace of development is associated with differences in protein stability. *Science* **369** (2020).
106. M. Matsuda, H. Hayashi, J. Garcia-Ojalvo, K. Yoshioka-Kobayashi, R. Kageyama, Y. Yamanaka, M. Ikeya, J. Toguchida, C. Alev, M. Ebisuya, Species-specific segmentation clock periods are due to differential biochemical reaction speeds. *Science* **369**, 1450–1455 (2020).
107. N. P. Hoyle, D. Ish-Horowicz, Transcript processing and export kinetics are rate-limiting steps in expressing vertebrate segmentation clock genes. *Proceedings of the National Academy of Sciences* **110**, E4316–E4324 (2013).
108. A. Kriegstein, A. Alvarez-Buylla, The glial nature of embryonic and adult neural stem cells. *Annu Rev Neurosci* **32**, 149–184 (2009).
109. J. H. Lui, D. V. Hansen, A. R. Kriegstein, Development and Evolution of the Human Neocortex. *Cell* **146**, 18–36 (2011).
110. L. Borghese, D. Dolezalova, T. Opitz, S. Haupt, A. Leinhaas, B. Steinfarz, P. Koch, F. Edenhofer, A. Hampl, O. Brüstle, Inhibition of notch signaling in human embryonic stem cell-derived neural stem cells delays G1/S phase transition and accelerates neuronal differentiation in vitro and in vivo. *Stem Cells* **28**, 955–964 (2010).
111. R. Iwata, P. Casimir, P. Vanderhaeghen, Mitochondrial dynamics in postmitotic cells regulate neurogenesis. *Science* **369**, 858–862 (2020).
112. R. Iwata, P. Casimir, E. Erkol, L. Boubakar, M. Planque, I. M. Gallego López, M. Ditkowska, V. Gaspariunaite, S. Beckers, D. Remans, K. Vints, A. Vandekeere, S. Poovathingal, M. Bird, N. Corthout, P. Vermeersch, S. Carpentier, K. Davie, M. Mazzone, N. V. Gounko, S. Aerts, B. Ghesquière, S.-M. Fendt, P. Vanderhaeghen, Mitochondria metabolism sets the species-specific tempo of neuronal development. *Science* **0**, eabn4705 (2023).
113. S. Cogliati, C. Frezza, M. E. Soriano, T. Varanita, R. Quintana-Cabrera, M. Corrado, S. Cipolat, V. Costa, A. Casarin, L. C. Gomes, E. Perales-Clemente, L. Salviati, P. Fernandez-Silva, J. A. Enriquez, L. Scorrano, Mitochondrial Cristae Shape Determines Respiratory Chain Supercomplexes Assembly and Respiratory Efficiency. *Cell* **155**, 160–171 (2013).
114. S. Cogliati, J. A. Enriquez, L. Scorrano, Mitochondrial Cristae: Where Beauty Meets

Functionality. *Trends in Biochemical Sciences* **41**, 261–273 (2016).
115. N. Baker, J. Patel, M. Khacho, Linking mitochondrial dynamics, cristae remodeling and supercomplex formation: How mitochondrial structure can regulate bioenergetics. *Mitochondrion* **49**, 259–268 (2019).
116. M. J. Bird, I. Adant, P. Windmolders, I. Vander Elst, C. Felgueira, R. Altassan, S. C. Gruenert, B. Ghesquière, P. Witters, D. Cassiman, P. Vermeersch, Oxygraphy Versus Enzymology for the Biochemical Diagnosis of Primary Mitochondrial Disease. *Metabolites* **9** (2019).
117. J. M. Buescher, M. R. Antoniewicz, L. G. Boros, S. C. Burgess, H. Brunengraber, C. B. Clish, R. J. DeBerardinis, O. Feron, C. Frezza, B. Ghesquiere, E. Gottlieb, K. Hiller, R. G. Jones, J. J. Kamphorst, R. G. Kibbey, A. C. Kimmelman, J. W. Locasale, S. Y. Lunt, O. D. Maddocks, C. Malloy, C. M. Metallo, E. J. Meuillet, J. Munger, K. Nöh, J. D. Rabinowitz, M. Ralser, U. Sauer, G. Stephanopoulos, J. St-Pierre, D. A. Tennant, C. Wittmann, M. G. Vander Heiden, A. Vazquez, K. Vousden, J. D. Young, N. Zamboni, S.-M. Fendt, A roadmap for interpreting 13 C metabolite labeling patterns from cells. *Current Opinion in Biotechnology* **34**, 189–201 (2015).
118. A. Bhaduri, M. G. Andrews, W. Mancia Leon, D. Jung, D. Shin, D. Allen, D. Jung, G. Schmunk, M. Haeussler, J. Salma, A. A. Pollen, T. J. Nowakowski, A. R. Kriegstein, Cell stress in cortical organoids impairs molecular subtype specification. *Nature*, doi: 10.1038/s41586-020-1962-0 (2020).
119. D. J. Di Bella, E. Habibi, R. R. Stickels, G. Scalia, J. Brown, P. Yadollahpour, S. M. Yang, C. Abbate, T. Biancalani, E. Z. Macosko, F. Chen, A. Regev, P. Arlotta, Molecular logic of cellular diversification in the mouse cerebral cortex. *Nature* **595**, 554–559 (2021).
120. C. J. Valvona, H. L. Fillmore, P. B. Nunn, G. J. Pilkington, The Regulation and Function of Lactate Dehydrogenase A: Therapeutic Potential in Brain Tumor. *Brain Pathology* **26**, 3–17 (2016).
121. J. Billiard, J. B. Dennison, J. Briand, R. S. Annan, D. Chai, M. Colón, C. S. Dodson, S. A. Gilbert, J. Greshock, J. Jing, H. Lu, J. E. McSurdy-Freed, L. A. Orband-Miller, G. B. Mills, C. J. Quinn, J. L. Schneck, G. F. Scott, A. N. Shaw, G. M. Waitt, R. F. Wooster, K. J. Duffy, Quinoline 3-sulfonamides inhibit lactate dehydrogenase A and reverse aerobic glycolysis in cancer cells. *Cancer & Metabolism* **1**, 1–17 (2013).
122. V. R. Fantin, J. St-Pierre, P. Leder, Attenuation of LDH-A expression uncovers a link between glycolysis, mitochondrial physiology, and tumor maintenance. *Cancer Cell* **9**, 425–434 (2006).
123. Y. Lin, B. L. Bloodgood, J. L. Hauser, A. D. Lapan, A. C. Koon, T.-K. Kim, L. S. Hu, A. N. Malik, M. E. Greenberg, Activity-dependent regulation of inhibitory synapse development by Npas4. *Nature* **455**, 1198–1204 (2008).
124. D. H. Ebert, M. E. Greenberg, Activity-dependent neuronal signalling and autism spectrum disorder. *Nature* **493**, 327–337 (2013).
125. S.-C. Tso, X. Qi, W.-J. Gui, C.-Y. Wu, J. L. Chuang, I. Wernstedt-Asterholm, L. K. Morlock, K. R. Owens, P. E. Scherer, N. S. Williams, U. K. Tambar, R. M. Wynn, D. T. Chuang, Structure-guided development of specific pyruvate dehydrogenase kinase inhibitors targeting the ATP-binding pocket. *J Biol Chem* **289**, 4432–4443 (2014).
126. S.-E. Ong, M. Mann, A practical recipe for stable isotope labeling by amino acids in cell culture (SILAC). *Nat Protoc* **1**, 2650–2660 (2006).
127. M. Diaz-Cuadros, T. P. Miettinen, O. S. Skinner, D. Sheedy, C. M. Díaz-García, S. Gapon, A. Hubaud, G. Yellen, S. R. Manalis, W. M. Oldham, O. Pourquié, Metabolic regulation of species-specific developmental rates. *Nature* **613**, 550–557 (2023).
128. F. Antonica, D. F. Kasprzyk, R. Opitz, M. Iacovino, X.-H. Liao, A. M. Dumitrescu, S. Refetoff, K. Peremans, M. Manto, M. Kyba, S. Costagliola, Generation of functional thyroid from embryonic stem cells. *Nature* **491**, 66–71 (2012).
129. M. Romitti, A. Tourneur, B. de Faria da Fonseca, G. Doumont, P. Gillotay, X.-H.

Liao, S. E. Eski, G. Van Simaeys, L. Chomette, H. Lasolle, O. Monestier, D. F. Kasprzyk, V. Detours, S. P. Singh, S. Goldman, S. Refetoff, S. Costagliola, Transplantable human thyroid organoids generated from embryonic stem cells to rescue hypothyroidism. *Nat Commun* **13**, 7057 (2022).
130. J. Labbadia, R. I. Morimoto, The biology of proteostasis in aging and disease. *Annu Rev Biochem* **84**, 435–464 (2015).
131. F. Buttgereit, M. D. Brand, A hierarchy of ATP-consuming processes in mammalian cells. *Biochem J* **312 (Pt 1)**, 163–167 (1995).
132. J. J. S. VerPlank, A. L. Goldberg, Regulating protein breakdown through proteasome phosphorylation. *Biochem J* **474**, 3355–3371 (2017).
133. T. Zhang, C. Wolfe, A. Pierle, K. A. Welle, J. R. Hryhorenko, S. Ghaemmaghami, Proteome-wide modulation of degradation dynamics in response to growth arrest. *Proc Natl Acad Sci USA* **114**, E10329–E10338 (2017).
134. G. A. Collins, A. L. Goldberg, The Logic of the 26S Proteasome. *Cell* **169**, 792–806 (2017).
135. D. J. Klionsky, S. D. Emr, Autophagy as a regulated pathway of cellular degradation. *Science* **290**, 1717–1721 (2000).
136. J. J. S. VerPlank, S. Lokireddy, J. Zhao, A. L. Goldberg, 26S Proteasomes are rapidly activated by diverse hormones and physiological states that raise cAMP and cause Rpn6 phosphorylation. *Proceedings of the National Academy of Sciences* **116**, 4228–4237 (2019).
137. D. Kornitzer, A. Ciechanover, Modes of regulation of ubiquitin-mediated protein degradation. *Journal of Cellular Physiology* **182**, 1–11 (2000).
138. L. B. Sullivan, D. Y. Gui, A. M. Hosios, L. N. Bush, E. Freinkman, M. G. Vander Heiden, Supporting Aspartate Biosynthesis Is an Essential Function of Respiration in Proliferating Cells. *Cell* **162**, 552–563 (2015).
139. O. A. Tarazona, O. Pourquié, Exploring the Influence of Cell Metabolism on Cell Fate through Protein Post-translational Modifications. *Dev Cell* **54**, 282–292 (2020).
140. W. G. Kaelin, S. L. McKnight, Influence of metabolism on epigenetics and disease. *Cell* **153**, 56–69 (2013).
141. A. Kasahara, S. Cipolat, Y. Chen, G. W. Dorn, L. Scorrano, Mitochondrial fusion directs cardiomyocyte differentiation via calcineurin and Notch signaling. *Science* **342**, 734–737 (2013).
142. M. D. Buck, D. O'Sullivan, R. I. Klein Geltink, J. D. Curtis, C.-H. Chang, D. E. Sanin, J. Qiu, O. Kretz, D. Braas, G. J. W. van der Windt, Q. Chen, S. C.-C. Huang, C. M. O'Neill, B. T. Edelson, E. J. Pearce, H. Sesaki, T. B. Huber, A. S. Rambold, E. L. Pearce, Mitochondrial Dynamics Controls T Cell Fate through Metabolic Programming. *Cell* **166**, 63–76 (2016).
143. K. Mitra, R. Rikhy, M. Lilly, J. Lippincott-Schwartz, DRP1-dependent mitochondrial fission initiates follicle cell differentiation during Drosophila oogenesis. *J. Cell Biol.* **197**, 487–497 (2012).
144. A. Bahat, A. Goldman, Y. Zaltsman, D. H. Khan, C. Halperin, E. Amzallag, V. Krupalnik, M. Mullokandov, A. Silberman, A. Erez, A. D. Schimmer, J. H. Hanna, A. Gross, MTCH2-mediated mitochondrial fusion drives exit from naïve pluripotency in embryonic stem cells. *Nature Communications* **9**, 5132 (2018).
145. X. Zheng, L. Boyer, M. Jin, J. Mertens, Y. Kim, L. Ma, L. Ma, M. Hamm, F. H. Gage, T. Hunter, Metabolic reprogramming during neuronal differentiation from aerobic glycolysis to neuronal oxidative phosphorylation, *eLife* (2016). https://doi.org/10.7554/eLife.13374.
146. J. Bonnefont, L. Tiberi, J. van den Ameele, D. Potier, Z. B. Gaber, X. Lin, A. Bilheu, A. Herpoel, F. D. V. Bravo, F. Guillemot, S. Aerts, P. Vanderhaeghen, Cortical Neurogenesis Requires Bcl6-Mediated Transcriptional Repression of Multiple Self-Renewal-Promoting Extrinsic Pathways. *Neuron* **0** (2019).

147. M. Khacho, A. Clark, D. S. Svoboda, J. Azzi, J. G. MacLaurin, C. Meghaizel, H. Sesaki, D. C. Lagace, M. Germain, M.-E. Harper, D. S. Park, R. S. Slack, Mitochondrial Dynamics Impacts Stem Cell Identity and Fate Decisions by Regulating a Nuclear Transcriptional Program. *Cell Stem Cell* **19**, 232–247 (2016).
148. Q. Wu, Y. Shichino, T. Abe, T. Suetsugu, A. Omori, H. Kiyonari, S. Iwasaki, F. Matsuzaki, Selective translation of epigenetic modifiers affects the temporal pattern and differentiation of neural stem cells. *Nat Commun* **13**, 470 (2022).
149. G. Ciceri, H. Cho, M. Kshirsagar, A. Baggiolini, K. A. Aromolaran, R. M. Walsh, P. A. Goldstein, R. P. Koche, C. S. Leslie, L. Studer, An epigenetic barrier sets the timing of human neuronal maturation. bioRxiv [Preprint] (2022). https://doi.org/10.1101/2022.06.02.490114.
150. V. Ramesh, F. Liu, M. S. Minto, U. Chan, A. E. West, Bidirectional regulation of postmitotic H3K27me3 distributions underlie cerebellar granule neuron maturation dynamics. *Elife* **12**, e86273 (2023).
151. K. Mätlik, E.-E. Govek, M. R. Paul, C. D. Allis, M. E. Hatten, Histone bivalency regulates the timing of cerebellar granule cell development. *Genes Dev.*, doi: 10.1101/gad.350594.123 (2023).
152. S. Cogliati, J. L. Cabrera-Alarcón, J. A. Enriquez, Regulation and functional role of the electron transport chain supercomplexes. *Biochem Soc Trans* **49**, 2655–2668 (2021).
153. M. Giacomello, A. Pyakurel, C. Glytsou, L. Scorrano, The cell biology of mitochondrial membrane dynamics. *Nat Rev Mol Cell Biol* **21**, 204–224 (2020).
154. M. S. Goyal, M. Hawrylycz, J. A. Miller, A. Z. Snyder, M. E. Raichle, Aerobic Glycolysis in the Human Brain Is Associated with Development and Neotenous Gene Expression. *Cell Metabolism* **19**, 49–57 (2014).
155. C. Fecher, L. Trovò, S. A. Müller, N. Snaidero, J. Wettmarshausen, S. Heink, O. Ortiz, I. Wagner, R. Kühn, J. Hartmann, R. M. Karl, A. Konnerth, T. Korn, W. Wurst, D. Merkler, S. F. Lichtenthaler, F. Perocchi, T. Misgeld, Cell-type-specific profiling of brain mitochondria reveals functional and molecular diversity. *Nat. Neurosci.* **22**, 1731–1742 (2019).
156. A. Brunet, M. A. Goodell, T. A. Rando, Ageing and rejuvenation of tissue stem cells and their niches. *Nat Rev Mol Cell Biol* **24**, 45–62 (2023).
157. C. López-Otín, M. A. Blasco, L. Partridge, M. Serrano, G. Kroemer, The Hallmarks of Aging. *Cell* **153**, 1194–1217 (2013).
158. C. C. Sherwood, F. Subiaul, T. W. Zawidzki, A natural history of the human mind: tracing evolutionary changes in brain and cognition. *Journal of Anatomy* **212**, 426–454 (2008).
159. O. Lindvall, Z. Kokaia, Prospects of stem cell therapy for replacing dopamine neurons in Parkinson's disease. *Trends in Pharmacological Sciences* **30**, 260–267 (2009).
160. A. H. Schapira, Mitochondrial disease. *The Lancet* **368**, 70–82 (2006).
161. G. S. Gorman, P. F. Chinnery, S. DiMauro, M. Hirano, Y. Koga, R. McFarland, A. Suomalainen, D. R. Thorburn, M. Zeviani, D. M. Turnbull, Mitochondrial diseases. *Nat Rev Dis Primers* **2**, 16080 (2016).
162. S. R. Louros, S. S. Seo, B. Maio, C. Martinez-Gonzalez, M. A. Gonzalez-Lozano, M. Muscas, N. C. Verity, J. C. Wills, K. W. Li, M. F. Nolan, E. K. Osterweil, Excessive proteostasis contributes to pathology in fragile X syndrome. *Neuron* **111**, 508-525.e7 (2023).
163. J. Lázaro, M. Costanzo, M. Sanaki-Matsumiya, C. Girardot, M. Hayashi, K. Hayashi, S. Diecke, T. B. Hildebrandt, G. Lazzari, J. Wu, S. Petkov, R. Behr, V. Trivedi, M. Matsuda, M. Ebisuya, A stem cell zoo uncovers intracellular scaling of developmental tempo across mammals. *Cell Stem Cell* **30**, 938-949.e7 (2023).
164. I. Espuny-Camacho, K. A. Michelsen, D. Gall, D. Linaro, A. Hasche, J. Bonnefont, C. Bali, D. Orduz, A. Bilheu, A. Herpoel, N. Lambert, N. Gaspard, S. Péron, S. N.

Schiffmann, M. Giugliano, A. Gaillard, P. Vanderhaeghen, Pyramidal Neurons Derived from Human Pluripotent Stem Cells Integrate Efficiently into Mouse Brain Circuits In Vivo. *Neuron* **77**, 440–456 (2013).
165. D. Linaro, B. Vermaercke, R. Iwata, A. Ramaswamy, B. Libé-Philippot, L. Boubakar, B. A. Davis, K. Wierda, K. Davie, S. Poovathingal, P. A. Penttila, A. Bilheu, L. De Bruyne, D. Gall, K. K. Conzelmann, V. Bonin, P. Vanderhaeghen, Xenotransplanted Human Cortical Neurons Reveal Species-Specific Development and Functional Integration into Mouse Visual Circuits. *Neuron* **104**, 972-986.e6 (2019).
166. N. Gaspard, T. Bouschet, R. Hourez, J. Dimidschstein, G. Naeije, J. van den Ameele, I. Espuny-Camacho, A. Herpoel, L. Passante, S. N. Schiffmann, A. Gaillard, P. Vanderhaeghen, An intrinsic mechanism of corticogenesis from embryonic stem cells. *Nature* **455**, 351–357 (2008).
167. D. Bishop, I. Nikić, M. Brinkoetter, S. Knecht, S. Potz, M. Kerschensteiner, T. Misgeld, Near-infrared branding efficiently correlates light and electron microscopy. *Nat Methods* **8**, 568–570 (2011).
168. K. Vints, P. Baatsen, N. V. Gounko, An accelerated procedure for approaching and imaging of optically branded region of interest in tissue. *Methods Cell Biol* **162**, 205–221 (2021).
.

Acknowledgements

I would like to thank my very dear and beloved wife Chiara, as well as my parents and my sister, and more broadly my family and family-in-law for their love, continuous support, help and suggestions. In particular, I would like to thank my grand-parents, as well as my grand-aunt, who are unfortunately not among us anymore, but who have been instrumental in my education and in communicating their infinite curiosity and their passion for arts and scientific endeavors.

I would like to thank also all my numerous friends for their support, their friendship and their availability all along my PhD.

Importantly, I would like to thank my main (KU Leuven) promotor, Pr Pierre Vanderhaeghen, for having welcomed me in his lab, for his close and demanding supervision, for his availability, for having given me the opportunity to work on a very interesting project, in an environment where research in fundamental neurosciences is undertaken at the highest level and showed how such an environment should be organized.

I would also like to thank in particular my ULB promotor, Pr David Gall for his supervision and advice, his availability and support.

Very specifically, I would like to thank a lot my co-supervisor, Dr Ryohei Iwata, for teaching me, day to day, all the technical aspects of the many experiments that we performed, showing me his level of excellence in experimental design and execution, his availability and kindness, for his help and smooth collaboration for the many experiments we performed together as we shared the co-first authorship of our paper, for our numerous discussions on more conceptual aspects of the project and of scientific research in general, for his friendship.

I would like to thank Emir Erkol, Leïla Boubakar, Mélanie Planque, Isabel M Gallego López, Martyna Ditkowska, Vaiva Gaspariunaite, Sofie Beckers, Daan Remans, Katlijn Vints, Anke Vandekeere, Suresh Poovathingal, Matthew Bird, Ine Vlaeminck, Eline Creemers, Keimpe

Wierda, Nikky Corthout, Kristofer Davie, Pr Bart Ghesquière, Pr Stein Aerts, Pr Sebastien Carpentier, Pr Sarah-Maria Fendt, Pr Natalia Gounko, Pr Massimiliano Mazzone for their help, their advice and their crucially important contributions to the project.

I would also like to thank all the lab members of the Vanderhaeghen lab for their help, their support and fruitful discussions.

I would like to thank all the administrative and technical staffs from the Center for Brain and Disease, in particular Raymond Spaans, Isabel Boux, Tineke Pellens, Bieke Tembuyser, for their availability, their kindness and the support they provided.

I would like to warmly thank Dr Bernard Dachy, the coordinator of my clinical training in Neurology, in which my PhD was inserted, for his availability, his benevolence, his efforts to coordinate at best all the aspects of my training scheme, and the excellence of the clinical training his has been and is still providing.

Personal Contribution

Conceptualization and Methodology, Pierre Casimir, Ryohei Iwata, Pierre Vanderhaeghen; Investigation, Pierre Casimir, Ryohei Iwata, Emir Erkol, Leïla Boubakar, Massimiliano Mazzone, Matthew Bird, Isabel Gallego López, Martyna Ditkowska, Suresh Poovathingal, Bart Ghesquière, Vaiva Gaspariunaite, Sofie Beckers, Anke Vandekeere, Daan Remans, Natalia Gounko, Sebastien Carpentier, Sarah-Maria Fendt, Pierre Vanderhaeghen.; Formal Analysis, Pierre Casimir, Ryohei Iwata, Emir Erkol, Nikky Corthout, Suresh Poovathingal, Kristofer Davie, Sebastien Carpentier, Sarah-Maria Fendt, Pierre Vanderhaeghen; Writing, Pierre Casimir, Ryohei Iwata, Pierre Vanderhaeghen; Funding acquisition, Pierre Vanderhaeghen; Resources, Stein Aerts, Pierre Vanderhaeghenn; Supervision, Pierre Vanderhaeghen.

Conflict of Interest

Pierre Vanderhaeghen, Ryohei Iwata and Pierre Casimir are inventors on a PCT application related to this work. All authors declare no other competing interests.

Curriculum Vitae

Last Name : Casimir **First Name :** Pierre

Date and place of birth: April 16, 1990; Uccle (Brussels, Belgium)

Civil Status : married

Citizenship: Belgian

Private Address : Avenue Louise, 114 , box25, 1000 Brussels, Belgium

Phone : + 32 494 58 42 59

Languages: French, English, Dutch, Italian

Education

1. High school: Athénée Royal de Watermael-Boitsfort, La brise, (Brussels, Belgium)
Section latin-mathematics-sciences
First of promotion 2007 (highest honours)
Prize of the highest percentage in last year
Prize of Mathematics
Prize of French
Prize of Geography
Prize of English
Prize of short French Essay (Terre d'Europe) of Kiwanis International
Prize of Olympiad of Latin (JUVENALIA) 2002, 2006, 2007
Prize of Olympiad of Biology (2007)

2. Other:
Certificate of Music Theory (Academy of Music of Watermael-Boitsfort), with highest honours
Certificate of Piano (Academy of Music of Watermael-Boistfort), with highest honours

3. University studies

a. Successful entrance examination in Polytechnics (Free University of Brussels, Université Libre de Bruxelles)
b. Medical school (Free University of Brussels, Université Libre de Bruxelles, ULB, Brussels, Belgium)

Bachelor in Medicine with high honours (2008-2011)

First of promotion Bach 1 in Medicine with highest honours, Fleurisse Mercier Prize

Master in Medicine with high honours (2011-2015)

- Summer internship in the St. Giles Laboratory of Human Genetics of Infectious Diseases, under the supervision of Pr. JL CASANOVA, The Rockefeller University, New York, USA (2013)
- One month clinical internship in the gynaecology department of the Tokyo Women's Medical University (TWMU) Hospital, Tokyo, Japan, 2014 in the context of an inter-university agreement between ULB an TWMU.

- Master's thesis in St. Giles Laboratory of Human Genetics of Infectious Diseases, under the supervision of Pr. JL CASANOVA, The Rockefeller University, New York, USA (2015)

Master of specialisation in Neurology (2015/2023)
- Assistant in Neurology at CHU Brugmann ULB (2015-2017)
- Assistant in Neurology at Hôpital Universitaire ERASME ULB (2017-2018)
- Assistant in Neurology at CHU Brugmann ULB (2022-2023)

c. Joint PhD in Biomedical Sciences (KULeuven)/Medical Sciences (ULB) (2018-present)

Participation in congresses

2019

- 5th European Stroke Organisation Conference, Milano 22-24 May 2019
  E-poster viewing: « Early venous filling and reperfusion hemorrhage after mechanical thrombectomy »

2022

- EMBO Workshop, Timing mechanisms linking development and evolution, EMBL Barcelona, Spain, 29 June-1 July, 2022, Poster: « The role of mitochondria and metabolism in the control of the rate of cortical neuron maturation »

Positions

PhD Fellowship F.W.O. (IRIBHM - ULB/VIB-KULeuven/ P. Vanderhaeghen)(10/2018-9/2022)

Publications in international peer-reviewed journals

1. **Rubén Martínez-Barricarte, Orli Megged, Polina Stepensky, Pierre Casimir, Marcela Moncada-Velez, Diana Averbuch, Marc Victor Assous, Omar Abuzaitoun, Xiao-Fei Kong, Vincent Pedergnana, Caroline Deswarte, Mélanie Migaud, Stefan Rose-John, Yuval Itan, Bertrand Boisson, Aziz Belkadi, Francesca Conti, Laurent Abel, Guillaume Vogt, Stephanie Boisson-Dupuis, Jean-Laurent Casanova, Jacinta Bustamante,** 2014, Mycobacterium simiae infection in two unrelated patients with different forms of inherited IFNgR2 deficiency - J Clin Immunol DOI 10.1007/s10875-014-0085-5
2. **Iwata, R., Casimir, P. & Vanderhaeghen, P**. Mitochondrial dynamics in postmitotic cells regulate neurogenesis. *Science* 369**,** 858–862 (2020).
3. **Elands, Sophie, Pierre Casimir, Thomas Bonnet, Benjamin Mine, Boris Lubicz, Martin Sjøgård, Noémie Ligot, et Gilles Naeije.** « Early Venous Filling Following Thrombectomy: Association With Hemorrhagic Transformation and Functional Outcome ». *Frontiers in Neurology* 12 (2021): 649079. https://doi.org/10.3389/fneur.2021.649079.
4. **R. Iwata*, P. Casimir*, E. Erkol, L. Boubakar, M. Planque, I. M. Gallego López, M. Ditkowska, V. Gaspariunaite, S. Beckers, D. Remans, K. Vints, A. Vandekeere, S. Poovathingal, M. Bird, N. Corthout, P. Vermeersch, S. Carpentier, K. Davie, M. Mazzone, N. V. Gounko, S. Aerts, B. Ghesquière, S.-M. Fendt, P. Vanderhaeghen**, « Mitochondria metabolism sets the species-specific tempo of neuronal development. » *Science*. 0, eabn4705 (2023). https://doi.org/10.1126/science.abn4705 *Equal Contribution